SILICON NANOWIRES FOR ENERGY GENERATION AND STORAGE

Memoria presentada por:

Sergio Pinilla Yanguas

Para optar al grado de

Doctor en Ciencias Físicas

por la Universidad Autónoma de Madrid con Mención Internacional

Directora:

Carmen Morant Zacarés

Facultad de Ciencias

Departamento de Física Aplicada

Junio 2017

Agradecimientos

Al presentar una tesis doctoral pareciera que se tratara del resultado de un trabajo estrictamente individual, sin embargo, no es así. Aunque el esfuerzo para el doctorando puede, en ocasiones, resultar abrumador, es también cierto que ese trabajo se ha ido nutriendo de conocimientos y experiencias transmitidas, tanto de manera formal como informal, por buen número de colegas y amigos. Por ello, considero que es de justicia señalar a aquellas personas que, de una u otra forma, han contribuido a este trabajo a lo largo de cinco años.

Entre ellas, en primer lugar, se encuentran mis dos directores de tesis, Eduardo Elizalde y Carmen Morant. Desde que comencé el doctorado no he parado de escuchar historias de tensas relaciones entre directores y doctorandos que transforman la tesis en poco menos que una tortura. Pues bien, mi experiencia ha sido la contraria. Desde que comenzara esta andanza, ellos han mostrado siempre una gran confianza en mi trabajo, dándome mucha libertad, aunque siempre pendientes de mi trabajo, aportando a él su experimentada visión y conocimiento. Creo haber crecido mucho como investigador con vosotros y espero y deseo que en el futuro esta relación se mantenga tanto dentro como fuera del laboratorio.

Probably, one of the most important experiences in my PhD, has been my stay in the Trinity College of Dublin. I would like to specially thank Valeria and John all the effort they put on me. All the teachings they gave me were invaluable and had enormously contributed to my development as researcher. I cannot leave aside any of my other partners in the TCD, Sonia, Shane, Joao and specially Park and Andrés. They all treated me like one of them from the first day, and now I am glad to call them friends.

No puedo olvidarme de agradecer a los compañeros y amigos del CIEMAT, Nieves, Rocío y Jose Lorenzo. Si leéis este trabajo, sin duda veréis vuestras aportaciones aquí y allá, ya que, tanto los debates que hemos mantenido como los resultados de muestras y medidas que me habéis facilitado, constituyen una parte importante de esta tesis.

También, he tenido la gran fortuna de colaborar con muchos de mis compañeros del departamento de Física Aplicada. Siempre que he recurrido a alguno de ellos en busca de ayuda, me he encontrado con su mejor disposición. Entre ellos, no puedo dejar de mencionar a Rafa, sin el cual no se podría haber realizado las medidas de técnicas IBA y mucho menos desgranar de una forma tan precisa los resultados; a Jose Luis Pau por su inestimable colaboración en las medidas de las propiedades eléctricas de los nanohilos, y a Alejandro Braña que tantas medidas y discusiones provechosas me ha proporcionado. También, agradezco a Manolo por su ayuda con los "4-puntas" y "spreading resistance"; a Vicente y a Miguel que me han dejado siempre usar sus laboratorios como si fuesen míos y a Paco, esa ayuda constante desde el otro lado del océano. Estas líneas se podrían extender aún más, pues pocos compañeros hay en el departamento que no me hayan ayudado en algún momento bien con un consejo o idea. A todo ellos mi más sincera gratitud.

Me gustaría proseguir los agradecimientos sin salir del departamento, centrándome esta vez en el equipo de técnicos, Felix, Jose, Luis, Edu y en especial mi compañero de buceo Tomás. Todos ellos han supuesto una importante ayuda en algo que no brilla lo suficiente cuando se redacta una tesis, pero que cualquiera que haya trabajado en experimentación sabe la importancia que tiene, y es el hacer frente a los problemas experimentales que surgen en el del día a día. También en este caso debo resaltar la paciencia y la amabilidad que siempre habéis mostrado conmigo.

También debo agradecer a los técnicos del SIdI su ayuda. Su profesionalidad y ánimo de colaboración han sido, sin duda, un apoyo inestimable. Especialmente debo mencionar a Isi, Espe y Quique, en cuyos laboratorios he pasado casi tanto tiempo como en los propios.

Hay muchos otros a los que aún no he mencionado y con quienes he aprendido y compartido muchos momentos del largo proceso de elaboración de la tesis; son otros doctorandos y amigos como mis compañeras de laboratorio Arancha y Teresa, y el "equipo" de las comidas, Chloe, Paola, Dario, Edu y Dani.

Por último, no puedo olvidar a quienes conmigo, sin duda, más han sufrido los rigores que conlleva el doctorado, mi familia. Tanto a mis padres como a mi pareja, Alicia, les dedico esta tesis, de la que, aunque no entiendan ni una palabra, han sido artífices en gran medida. La gente que me conoce sabe que si algo me caracteriza es mi actitud tranquila. A lo largo de estos cinco años de recorrido ha habido muchos altibajos y, detrás de mí aparente tranquilidad, en todo momento habéis estado vosotros. Vuestra comprensión, apoyo y ánimo, han sido siempre el pilar sobre el que he podido afrontar cualquier contratiempo. Por eso, y por mucho más, gracias.

Esta tesis reúne mis primeros trabajos de investigación en el ámbito de la Física Aplicada, tarea a la que, pese a la difícil tesitura por la que pasa la investigación en España, pretendo dedicar mi futura vida profesional. Espero y deseo que en próximos proyectos muchos de quienes he citado puedan acompañarme para seguir aprendiendo con su ayuda.

Summary

In the past few decades, an increasing interest has been growing towards the nanostructured materials. Their enhanced properties have opened a whole new investigation field with applications in almost every area of knowledge. Specifically, silicon nanomaterials have attracted much attention owing to its abundance, relatively low price and large variety of applications. Among the Si nanostructured materials, one-dimensional silicon nanowires (SiNWs) are of particular interest. There are several SiNWs synthesis processes (bottom-up and top-down approaches), however, most of these synthesis methods either suffer from scalability issues or compromise the quality of SiNWs. Therefore, new methods to develop high-quality SiNWs in a scalable manner is of great importance and highly necessary. In this research, a new synthesis procedure based on the metal assisted chemical etching approach (MACE) has been used. This method provides the quality and scalability necessary for industrial level applications.

The present work, has been focused on the synthesis of SiNWs and the study of their performances in solar cells and LIBs. Our studies on solar cells aimed at improving the light absorption and reducing the surface recombination. These goals were successfully obtained using patterned SiNWs, along with other nanomaterials, such as carbon nanotubes.

The implementation of SiNWs in the LIBs has been carried out in three innovative electrode architectures. The introduced innovations ranged from the exploitation of synergies between nanomaterials, to the direct growth of large amounts of amorphous SiNWs on the current collector. Each of these architectures has been systematically studied by galvanostatic cycling, achieving a good description of the electrodes performance. Finally, another family of materials called MXenes has been studied. These 2D materials show promising properties which paired with SiNWs could lead to a very interesting hybrid material for LIBs.

Resumen

En las últimas décadas, el interés hacia los materiales nanoestructurados ha crecido de manera incesante. La gran diversidad de propiedades que presentan tiene aplicaciones en casi todas las áreas del conocimiento. Específicamente, los nanomateriales de silicio han atraído mucha atención debido a la gran abundancia, precio relativamente bajo y gran variedad de aplicaciones del silicio. Entre los materiales nanoestructurados de Si, los nanohilos de silicio (SiNWs) son de particular interés. Entre los numerosos procesos de síntesis de SiNWs, en esta tesis nos hemos centrado en un método relativamente nuevo, llamado "metal assisted chemical etching" (MACE). Este método proporciona una alta calidad SiNWs y una fácil escalabilidad, lo que podría permitir el desarrollo de aplicaciones a nivel industrial.

En el presente estudio, se investigó la aplicación de estos SiNWs en dos campos relacionados con la energía: las células solares y las baterías de ion de litio (LIBs). En el ámbito de las células solares, la investigación se centró en la mejora de la absorción de la luz y la recombinación superficial del material. Para alcanzar este fin, se desarrollaron soluciones novedosas como el crecimiento de SiNWs con patrón o el uso de nanotubos de carbono como recubrimiento conductor.

La implementación de los SiNWs en LIBs se realizó en forma de tres innovadoras arquitecturas de electrodos. Estas innovaciones comprendían desde la explotación de sinergias entre nanomateriales hasta el crecimiento directo de SiNWs amorfos en el ánodo. Cada una de estas arquitecturas fue estudiada mediante ciclado galvanostático, obteniendo una buena descripción del comportamiento del material y un rendimiento electroquímico extraordinario. Por último, se estudió otra familia de materiales llamados MXenes. Estos materiales 2D muestran propiedades prometedoras que junto con los SiNWs podrían conducir a un material híbrido muy interesante para LIBs.

Index

Chapter 1:

Introduction

1.1 Silicon

In the last decades, Silicon (Si) has been the most widely used semiconductor in high technology applications. It is the basic building block of the actual electronics[1,2], solar cells[3] and many others industry applications[4]. Among the advantages of the Si, it can be highlighted its extreme abundancy, being the second major constituent of the earth crush. In addition, it is very stable and non-toxic. The long experience of the industry with Si is also a remarkable advantage, and have led to a very polished fabrication and purification processes. This set of properties, makes the industry much more receptive to use Si in innovative applications. Additionally, it can be remarked that it is the most well-known semiconductor. It shows extremely good properties such as good carrier mobility or an appropriate band gap for terrestrial light spectrum, making it suitable for many applications[1].

Since the development of the low-dimension structures, a great interest has grown towards the research of the Si in the nanoscale. The superior performance of these materials compared to bulk Si in many applications[5], have resulted in the development of numerous Si nanomaterials. Among them, it can be found: silicon nanoparticles[6,7], nanospheres[8], nanotubes[9], nanowires[10], nanocones[11] and many others. In this work, a deep study on the one-dimensional silicon nanowires (SiNWs) will be done.

1.2 Silicon Nanowires (SiNWs)

1.2.1 Synthesis methods

SiNWs have very different properties depending on their structure and morphology, and in most of the cases, these characteristics are directly determined by the synthesis method.

The synthesis methods are usually divided in two major approaches: bottom-up and top down. In all the bottom-up methods, the SiNWs grow from the successive assembly of Si atoms, forming structures which lengths are between few nanometers and several microns[12]. On the contrary, the top-down methods are based on the shaping of pre-existing Si substrates, achieving structures in the nanoscale dimensions. The most representative methods of each approach are the Vapor-Liquid-Solid (VLS) method through chemical vapor deposition (CVD), and the metal assisted chemical etching (MACE), respectively.

There are a number of differences between these methods. The first one is that the VLS is usually achieved by high temperature and needs gaseous precursors, implying the use of specific equipment. Moreover, the high temperatures required, could not be feasible for all applications. On the other hand, the MACE is achieved by a wet chemical reaction which does not needs any specific equipment or temperature requirement.

Another difference which can be noticed, is that the MACE presents a much more flexibility in the type of structures produced. The diameters of the MACE structures can be controllably ranged between 5 nm and 1 μm, while the VLS shows a much more restricted range[13]. Moreover, the MACE has proven to produce structures with higher surface-to-volume ratios that the VLS[14]. Opposite to the aforementioned MACE advantages, the VLS produces SiNWs with smoother and defectless surfaces[13].

To conclude, it can be highlighted very important similarities: both techniques produce SiNWs with high core purity and controlled doping, being really interesting for a number of nanodevices[10].

1.2.2 Metal Assisted Chemical Etching (MACE)

In the present work we will delve into the MACE method for obtaining SiNWs. This quite novel method has been gaining importance in the last decade, being right now one of the most used for the SiNWs production.

The MACE can be outlined as a localized etching of silicon in the presence of a catalyst, which can be any noble metal such as Au, Ag, Pt or Pd. When a Si surface is partially covered by any of this metals, and then subjected to a specific solution, the Si beneath the catalyst is removed leaving the metal-free surface untouched. This continuous process makes the metal sink into the Si substrate, carving pits on it. If the metal density in the surface is high enough, these pits gets interconnected forming SiNWs.

The catalyst plays a fundamental role in the MACE, and its deposition has a deep influence in the features obtained at the end of the process. There are numerous of valid deposition techniques for the catalysts, such as thermal evaporation[15], sputtering[16], electroless deposition[17] and many others. Due to the nature of the process, the shape in which the catalyst is deposited determines the features produced by the etching. This fact is very important because allows a very precise control of the nanostructures features by patterning the catalyst deposition. For the patterning, the physical deposition techniques (i.e. sputtering or thermal evaporation) are the appropriate methods. On the other side, plating methods such as electroless deposition generates more random shapes, being more suitable when a precise shape of the SiNWs is not extremely important. Moreover, plating techniques are very fast, easy to perform and have no sample size limitation, what makes them the most

common approach for the SiNWs growth. From the plating methods, this work focuses on the electroless deposition.

The metal deposition in the electroless method is based on a typical galvanic process[18]. The metal ions in the solution (containing noble metal salts) are reduced in the surface of the Si by injecting holes in its valence band. In the presence of water, this hole injection leads to the oxidation of the Si which is removed by the HF contained in the electroless solution, producing a mild etching on the Si.

Once the ions are reduced, they form metal aggregates. The new ions which interact with the Si, tend to get incorporated to these aggregates rather than to the naked Si surface. This behavior produces a continuous growth of the aggregates which end up forming nanoparticles. At the end of the procedure, the surface is covered by metal nanoparticles. This process is schematically represented in **scheme 1.1**.

After catalyst deposition, by any described method, the Si substrate with the catalyst is immersed into the etchant of the MACE, initiating SiNWs growth. The etching solution is usually a HF/H_2O_2 mixture. Similarly, as the etching due to the electroless solution, the removal of the Si is caused by the hole injection into the Si in the presence of HF. However, in this case, the source of holes is not the metal ions, but the H_2O_2. This reactant gets reduced in the noble metal surface injecting the holes into the Si through the catalyst nanoparticle[19]. The electron availability and better energy position respectively the Si valence band, makes more favorable the hole injection through the metal than the H_2O_2 directly on the Si[13,20]. The aforementioned is the responsible for the localized etching of the metal-covered Si, making the non-covered Si surface almost inert to the reaction. The whole process is displayed in **scheme 1.1**.

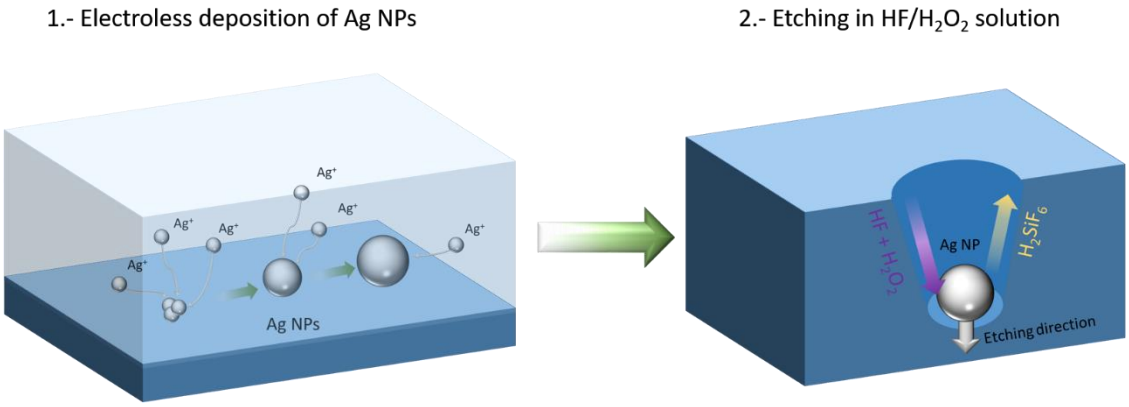

Scheme 1.1 Diagram of the electroless deposition of Ag NPs and the subsequent etching of the Si in a HF+H_2O_2 solution.

1.2.3 Applications

SiNWs belong to the one-dimensional materials due to their lateral size. For this reason, they show particular properties compared with their bulk counterparts, such as much higher surface-volume ratio[21] and quantum confinement effects[22]. These unique properties have attracted a lot of attention in many fields. Specifically, the MACE SiNWs have been used in field effect transistors[23], chemical sensors[24] and field emiters[25]. However, the higher impact of this material has been in the light harvesting and energy storage areas. The high light absorption of the SiNWs arrays and the inherited properties from the starting Si, have made them outstanding candidates both for photovoltaic and photoelectrochemical solar cells[26]. In the energy storage field, SiNWs have attracted much interest in lithium ion batteries (LIBs) and capacitors[10] because of their high surface-volume ratio. In this work, special attention is paid to the photovoltaic solar cells and LIBs.

1.2.4 Introduction photovoltaic to solar cells (PV)

Actually, Si is the most popular material for photovoltaic (PV) solar cells, holding approximately the 90% of the PV market. Its unchallenged position in this market, comes from the extremely good features that this material presents. Some of them have been already

commented, such as its abundancy, non-toxicity or compatibility with modern electronics. Additionally, it presents a band-gap almost perfect for the absorption of the terrestrial solar spectrum and, when purified, shows very long diffusion lengths.

In conventional Si solar cells, the planar p-n junctions require large amounts of Si to fully absorb the incident light. Moreover, due to the large thicknesses required, the purity of the material needs to be very high to avoid volumetric recombination. These requirements translate into high fabrication costs. In order to address the price issues, the research in this field have been directed in three differentiated paths[26]: the efficiency increase by new PV designs, the cost reduction of the Si production and the development of PV structures with low amount of material and lower purity requirements. The SiNWs can be used in the last approach. Their extremely high absorption could reduce the amount of material used[27], and the new p-n junction configurations they offer[21], could reduce the need of high diffusion lengths.

1.2.5 Introduction to lithium ion batteries (LIBs)

In the last decades, rechargeable lithium-ion batteries (LIBs) have been subjected to a growing demand due to the increasing popularity of portable electronic devices. The superior volumetric and gravimetric energy density of LIBs have stablished them as the prime portable energy source. Moreover, in the last few years, their application into the electric vehicles have made them a crucial device for the development of the renewable energies. This fast growth of the energy storage necessities, have encouraged the development of new materials for improved capacities and longer lifetimes.

The working principle of LIBs is based on the intercalation and de-intercalation of the lithium ions in the positive and negative electrodes. As more ions the material can host, larger is the material capacity. The commercial anodes of the LIBs, are made of graphite, which can only accommodate one Li ion for every six C atoms. This intercalation ratio leads to a

very low theoretical capacity of 370 mAh/g. In order to improve the anode capacity, great efforts have been devoted searching for high-capacity electrode materials. Among the most promising anodes materials it can be found the Si. It shows the higher theoretical capacity known to the date, being 4200 mAh/g. However, this massive lithiation capacity comes accompanied by a huge volume increase of almost the 400%. These volumes changes are an insurmountable obstacle for common Si structures, which rapidly breaks down. However, the nanostructured Si could help to overcome this limitation. Their high surface-volume ratio improves the accommodation of the Li ions without the fragmentation. Moreover, the nanostructuration can also allow high charge/discharge rates due to the high surface available. To the mentioned advantages, common of all Si nanomaterials, the SiNWs also supply improved conduction paths, due to their higher lengths. This conduction paths suppress the influence of the low conduction in-between nanomaterials which could improve the overall performance of the device. All the above discussed features makes the SiNWs a promising anode material for the LIBs.

1.3 MXenes

In the past decade, two-dimensional (2D) materials, have attracted much interest and they have been focus of intensive research. Since the discovery of the graphene[28] and its extraordinary electronical properties, a large amount of 2D materials have been discovered. Among these materials it can be found hexagonal boron nitride (h-BN),[29] transition metal dichalcogenides (TMDs),[30] oxides (TMOs)[31–33] and layered double-hydroxides (LDHs)[34]. The atomic scale of their thicknesses provide an extraordinarily large specific surface areas, which allows an excellent performance in applications such as energy storage[35–45], gas sensing[46] or nanoelectronics[47].

In the past few years, a new family of transition metal carbides and carbonitrides called "MXene" has been added to the 2D materials group. These materials are obtained by wet hydrofluoric chemical treatment from the $M_{n+1}AX_n$ phases. The name of the MAX phase comes from their composition. M denotes an early transition metal such as Ti, V, Nb, Mo, etc., A indicates an A-group element such as Al, Si and Ga, etc., the X is carbon and/or nitrogen and n=1, 2, 3. [48–51] The hydrofluoric treatment of these materials removes the A elements and leaves a multilayered MX material, which is the so called MXenes. Due to their wet etching synthesis method, MXenes are usually terminated by –O, –OH and/or –F with the general formula $M_{n+1}X_nT_x$, where T represents surface termination[51,52]. After the etching, the layers of the material are still bonded by weak van der Waals and/or hydrogen bonding[51]. These bonds can be broken through delamination to obtain monolayered colloidal solutions. To date, multilayered $Ti_3C_2T_x$, Ti_2CT_x, Ti_3CNT_x, Nb_2CT_x, V_2CT_x, Mo_2CT_x, $Mo_2TiC_2T_x$ and many other MXenes, as well as their corresponding colloidal solutions, have been reported.[53–58]

1.4 Thesis objectives

The objectives of this work are the growth of SiNWs by MACE for their application into photovoltaic solar cells and lithium ion batteries. The structure of the thesis is designed in six results chapters, number three to five are focused in the PV solar cells, while six to eight to the LIBs. The general objectives of the work are:

1. Providing a good **description of the SiNWs synthesis methods**, kinetics and characteristics of the resulting material. Along the thesis, different MACE procedures were employed to approach specific objectives. Prior to its use, the resulting SiNWs in each case were well characterized, and also the growth procedure was optimized.

This objective is addressed in the third, fifth and seventh chapter, for different MACE procedures in each one.

2. Investigating **the limiting factors** which could suppress the application **of the SiNWs into the PV solar cells** and look for solutions to these problems. Specifically, the focus of the research is on the surface recombination of the SiNWs. In chapter four and five, two alternative methods are provided to tense the reduction of this limiting effect.
3. Developing **novel synthesis procedures and electrodes architectures** to allow the use of **SiNWs into the LIBs**. The standard MACE is not directly applicable to the LIBs. Therefore, in chapter six to eight, different modifications of the MACE procedure are explored in order to make SiNWs which could be used in the LIBs. Moreover, along this three chapters, some novel electrodes architectures are developed answering to certain material necessities.
4. Formation and characterization of **electrodes composed by SiNWs** for LIBs. A comprehensive study of the electrochemical performance is done in each chapter, and every innovation introduced to the material is experimentally evaluated. The analysis of the electrochemical data is addressed in each case and a well description of the behaviour of the material is provided.

Chapter 2:

Techniques and equipment

In this chapter, some of the most used experimental setups and characterization techniques along the work are briefly introduce. It is out of the work's scope to give a detailed insight of all the characterization and synthesis techniques used. Consequently, only those experimental equipments that are not commercial are described in order to detail their features. In the characterization techniques section, special attention is paid to the electrochemical techniques, re-visiting some basic concepts for the interpretation of the results.

2.1 Synthesis techniques

2.1.1 Chemical vapour deposition (CVD)

This synthesis technique is based on the material deposition from vapour phase reactants. The reaction between these agents is usually driven by high temperatures and takes place in a purified atmosphere (obtained through low pressure or inert gas purge). This technique can produce a large amount of reactions, being quite versatile[59].

The experimental system consists on a tubular furnace with a quartz tube (125 cm long 35 cm wide) where the samples are introduced, **scheme 2.1**. The gas inlet is software controlled. Additionally, our specific equipment has four possible channels and allow gas mixtures of four different gasses. Along the work, only three gasses were used: argon (Ar), nitrogen (N_2)

and hydrogen (H_2). The maximum fluxes of those gasses were of 1000 sccm, 1000 sccm and 300 sccm, respectively. The working temperatures of the furnace are between ambient temperature (T.A.) and 1200ºC. The increasing and decreasing temperature ramps as well as the plateau temperature and duration is also software controlled.

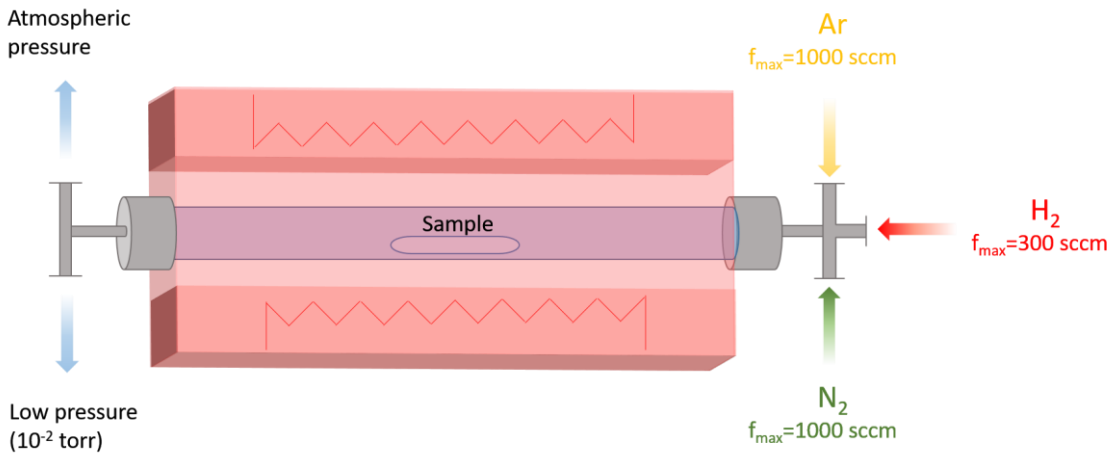

Scheme 2.1 Diagram of the CVD system experimentally used.

This equipment was used for the carbon nanotubes (CNTs) synthesis, described in the fourth chapter, and in all the thermal treatments along the work. For the CNT synthesis, ethanol (ETOH) was used as carbon source. The insertion of this agent into the reaction chamber was done by bubbling N_2 through a heated ETOH solution, **scheme 2.2**. The output N_2 drags ETOH, which reacts into the chamber forming the CNTs.

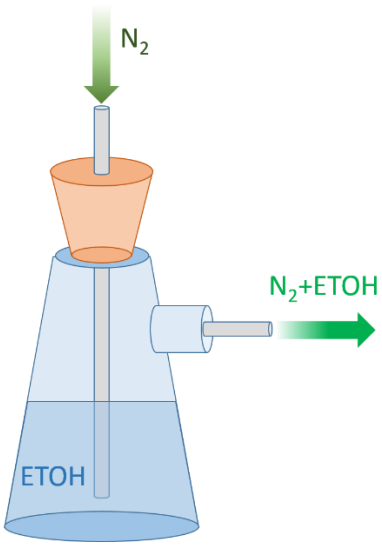

Scheme 2.2 Diagram of the ETOH addition to the N2 flux.

The CNTs synthesis was performed at atmospheric pressure, but some of the thermal treatments were done at low pressure. This low pressure was achieved by the addition of a pump at the gas output, **scheme 2.1**.

2.1.2 Radio frequency magnetron sputtering (RF-MS)

Radio frequency magnetron sputtering (RF-MS) belongs to the physical vapor deposition techniques (PVD). It is a sputtering technique which uses AC discharges (in the radio frequency range) in the electrode to generate plasma. The ions in the plasma collide with the target containing the source material. This material, is pulled out from its starting position and arrive at the sample holder. Unlike the DC sputtering techniques, the RF discharges allow the deposition of dielectric source materials due to their impedance drop with the increasing frecuency[60].

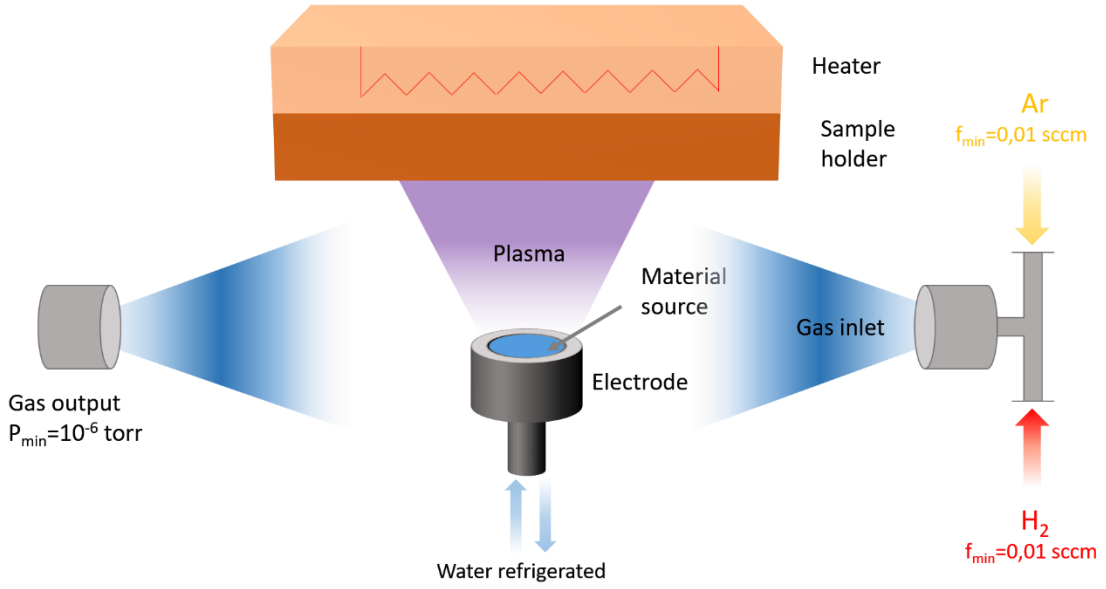

Scheme 2.3 Diagram of the RF-MS chamber.

The RF-MS was used in this work for the deposition of aluminum (Al), described in fifth chapter, and hydrogenated amorphous silicon (a-Si:H), seventh chapter. The used equipment counts with a round shaped electrode of 2 inches diameter with a fixed operating frequency of 13,56 MHz. The sample holder is equipped with a heater and a thermocouple which are placed 10,5 cm away from the electrode. The gas inlet is regulated by two flowmeters which allow to perform gas mixtures of Ar and H_2. The pumping system permits a minimum

pressure of 10^{-6} torr, which it has to be reached before any deposition process takes place. When this high vacuum conditions are obtained, the system is set to a working pressure of $8 \cdot 10^{-3}$ torr, then, the plasma can be turned on. Usually, in order to achieve this pressure, a flux of 3 sccm of the corresponding plasma gas is used. For Al deposition only Ar is used, while for a-Si:H a mixture of Ar and H_2 is needed.

2.2 Characterization techniques

2.2.1 Electrochemical characterization

The electrochemical characterization was performed with a 12-channel Arbin Instruments BT2143 workstation at room temperature (25 °C). As further discussed in chapter 6, the cells configurations were half-cells where the working electrode was faced to a pure lithium electrode, which act as both counter and reference electrode. The technique used for the electrochemical characterization was galvanostatic cycling. This technique is based on the application of a constant current between the working and counter electrodes while measuring their voltage difference. The capacity (mAh) of the working electrode material is extracted by multiplying the current and the cycle length. This capacity normalized by the mass of the material is the specific capacity[61] (mAh/g). The specific capacity can change between cycles due to the degradation of the electrode material or irreversible lithiation processes. For this reason, the specific capacity of a LIB is usually given as a function of the cycle number, **figure 2.1A**.

Another common way to display the galvanostatic cycling results is in the form of charge-discharge voltage profiles (VP). In these graphs, the voltage of the electrode (versus the lithium counter electrode, vs Li/Li^+) is plotted as a function of the accumulated specific capacity[61] for a single cycle, **figure 2.1B**. This allows the obtainment of the voltages at which the electrode is storing lithium, being dependent on the lithiation processes of the material.

Additionally, the galvanostatic cycling results can be derived to obtain the differential capacity (dQ/dV, denoted as DC) curves, **figure 2.1C**. The aforementioned curves show peaks where lithiation/delithiation reactions take place. The voltage of these peaks permits to identify the compounds formed in each stage of the operation of the cell. The DC curves and the VP are very closely related. Indeed, the peaks shown in DC appears in the VP as changes in slope.

The peaks in the DC curves can have two kind of shapes depending on the nature of the reaction. Due to the fact that the silicon lithiation is regarded as a solid-solution reaction, the behavior of the voltage will be determined by the Gibbs phase rule[62]. This rule stablishes that, if the system has one degree of freedom (in a constant temperature and pressure system), it is the electric potential and it varies with the lithium concentration. However, if the system has zero degrees of freedom, the electrode voltage is independent of the lithium concentration. The degrees of freedom[62] can be obtained through **equation 2.1**, where f are the degrees of freedom, C the number of components and P the number of phases.

$$f = C - P \qquad \textbf{Equation 2.1}$$

In the silicon lithiation there always are two components (Si and Li); therefore, f is determined by the number of phases P. If the initial Si is amorphous, as well as the resulting Si-Li compound, there is only one phase and the voltage change with the Li incorporation. On the other hand, if the Si is crystalline and the Si-Li compound is amorphous, there are two phases and the voltage do not change along the Li incorporation. This effect translates into the DC curves as a broad peak and a delta type peak, for one phase and two phase transitions respectively, **figure 2.1C**. Similarly, in the VPs this effect is shown as a flat plateau for two-phase transitions and as a sloping curve for one-phase transitions, **figure 2.1B**.

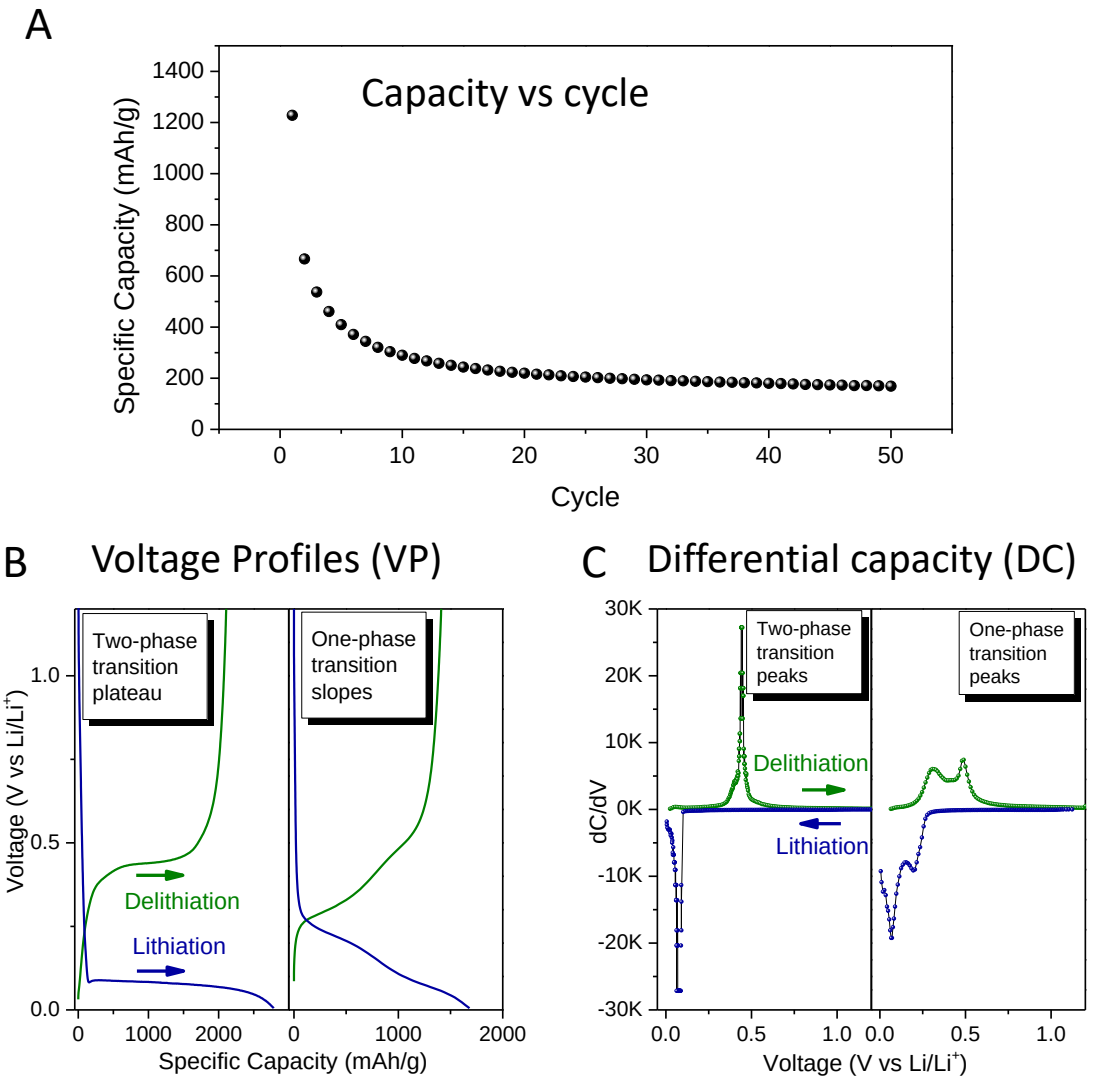

Figure 2.1 A) Specific capacity vs cycle. Two and one phase transitions reactions voltage profiles, B), and differential capacity curves, C).

The other characterization techniques used along the manuscript are either, described in the specific application/section or are so widely known that a detailed description is not necessary.

Chapter 3:

Silicon nanowire arrays as anti-reflective layer

3.1 Introduction

The aim of this chapter is to provide a good description of the Metal-Assisted Chemical Etching (MACE) method and its application for obtaining anti-reflective layers. The MACE method is used all along the presented work, so a detailed understanding of the process and its parameters is the first objective of the thesis. In this chapter a morphological characterization of the SiNWs is provided, delving into their crystallinity, growth direction and the etching parameters that affect them. Also, a chemical characterization of the surface and the core of the nanowires is included in this study. Consecutively, the kinetics of the reactions are studied, obtaining the etching rates for different conditions and the general parameters of the process. At the end of the chapter the optical properties of the SiNW-covered surfaces are analysed and their viability as anti-reflective layer is evaluated.

3.2 Experimental

The SiNWs were synthesized through a Metal-Assisted Chemical Etching (MACE) on p-type (1-10 Ωcm, Boron doped, 300 μm) {100} monocrystalline silicon wafers and on (1-10 Ωcm, Boron doped, 200 μm) multicrystalline silicon wafers. The standard two step MACE procedure was applied[13,63] with a previous cleaning process of the substrates. The cleaning

was started with a consecutively sonication for 10 minutes in acetone, isopropyl alcohol and deionized water. After this cleaning, a mixture of H_2SO_4 (94-97%) and H_2O_2 (35%) was prepared in volume ratio 3:1. The wafers were immersed into this acid mixture, usually called Piranha solution, for 30 minutes. Then, the silicon dioxide formed in the surface was removed by a HF (5%) bath for 5 minutes. After the cleaning procedure described, the MACE was performed.

The MACE used is composed by two consecutive baths, the first one consists on the electroless deposition of silver nanoparticles[13,17], which acts as catalyst, and the second one on the localized oxidation of the silicon where the catalyst was placed. The first bath was a 0,01M $AgNO_3$ (99,5%) and 4,8M HF (38-40%) solution while the second one was a HF and H_2O_2 solution in a molar ratio ($\varepsilon = [HF]/[H_2O_2]$) of ε=24. This molar ratio was chosen from the bibliography to obtain straight and non-porous SiNWs[63]. The samples were immersed in the first bath between 30 seconds to 3 minutes and into the second bath between 3 minutes to 20 minutes depending on the desired length for the nanowires. The temperatures of the solutions were kept constant during the growth.

After the last MACE bath, the samples were immersed into HNO_3 (65%) for 30 minutes in order to remove the silver nanoparticles (AgNPs) in between the nanowires. Finally, the samples were rinsed in deionized water and dried with a nitrogen gun.

3.3 Results and discussion

3.3.1 Morphological and structural characterization of the SiNWs

As commented in the experimental section of the chapter, two different substrates have been used: {100}* monocrystalline polished silicon wafers and textured multicrystalline silicon wafers. The main difference between these substrates is that while the monocrystalline (c-Si) just show one crystal orientation, the multicrystalline (mc-Si) shows many of them all around the surface. Crystal orientation is very important for the MACE process and has a decisive effect on the growth direction of the nanowires[64]. This is because for removing a silicon atom from the surface, the back bonds that keeps him attached to the bulk have to be broken. A silicon atom in the {100} surface has 2 back bonds, while in the other priority surfaces like {110} and {111} there are 3 back bonds[65]. This makes that the <100> direction is the easiest to etch and so the preferential direction in which the silver particles will dig forming the SiNWs. Hence, if the surface has {100} orientation, SiNWs will grow vertical (**Figure 3.1A**), otherwise they will grow slanted. In the case of mc-Si substrates, this can be observed in the grain boundaries (**Figure 3.1B**), where each crystal orientation leads to a different inclination.

* Please note that the distinction between {lmn}, [lmn] and <lmn> is on purpose, using them to surfaces, directions and family of directions respectively.

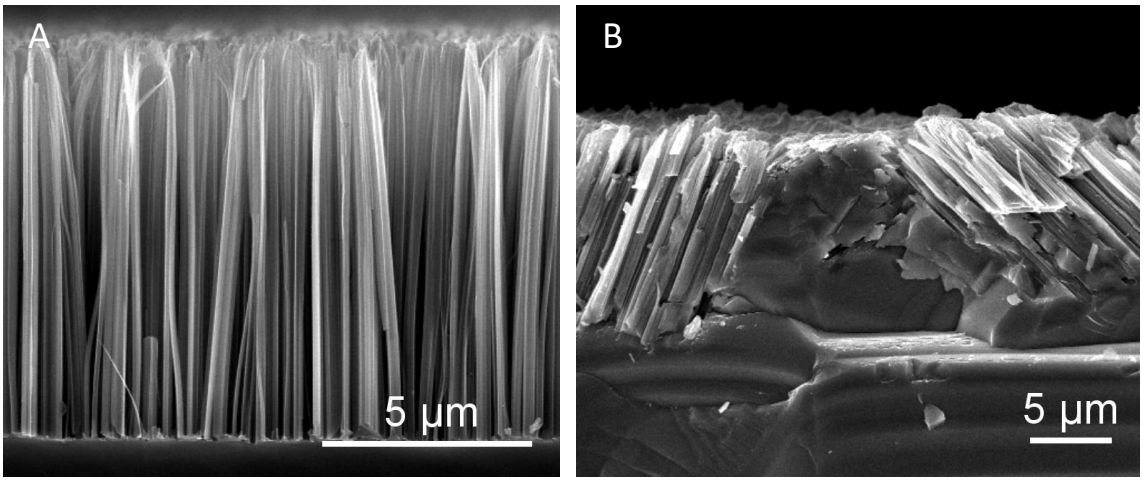

Figure 3.1 FESEM images of SiNWs grown on, A), c-Si {100} wafers and B), mc-Si wafers.

The SiNWs grown on c-Si and mc-Si were also studied by HRTEM in order to confirm the dependence of the inclination with the crystallographic orientation. The sample preparation for the TEM measurements was performed as follows; first, the sample was scratched with a scalpel immersed in an ethanol solution. Then, the solution with the sample inside was sonicated for 15 minutes. After that, some drops of the solution were deposited on a copper microscopic grid.

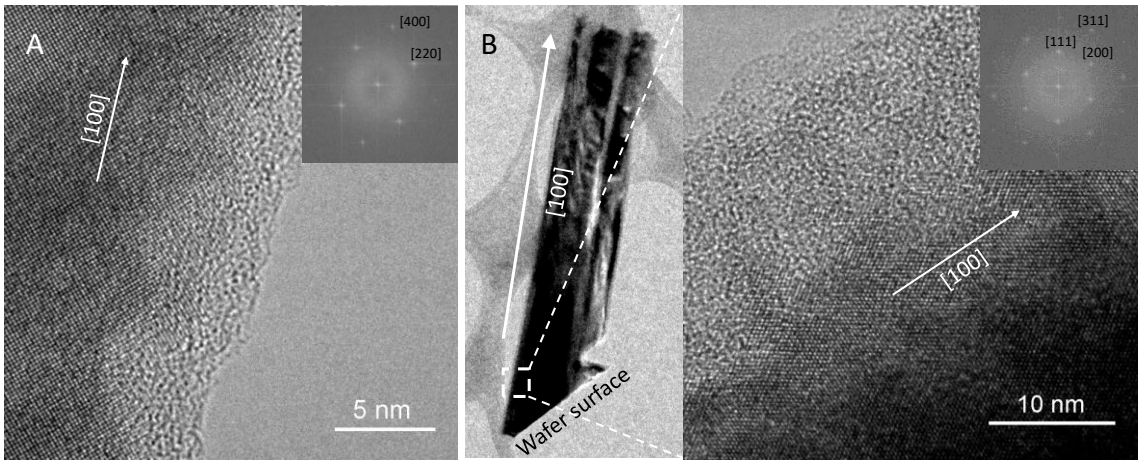

Figure 3.2 TEM images of SiNWs grown on, A), c-Si {100} wafers and on, B), mc-Si. Inset, the corresponding selected area diffraction pattern (SADP).

The TEM images of the SiNWs grown on c-Si, **figure 3.2A**, reveals a highly crystalline core with an axial axis with a plane separation of 0,27 nm, which corresponds to the [200] direction. Moreover, the inset selected area diffraction pattern (SADP) indicates the presence of the [400] direction in the axial axis. Therefore, the growth direction is the <100> family, in agreement with the FESEM observations.

In the case of the SiNWs growth on the mc-Si, nanowires with different inclinations were observed. **Figure 3.2B** shows a bundle of three slanted nanowires and part of the substrate. In the enlargement of the mentioned figure, it can be found an axial axis plane separation of 0,54 nm, which corresponds to the [100] direction. Moreover, this result is coincident with the inset SADP. The results clearly show that, even not being the crystalline direction of the surface, the [100] direction is the preferential growth direction of the MACE process.

It is worthy to mention that it has been reported the growth in other crystalline directions when the temperature of the attack is very high[63], or when using a thick and continuous catalyst layer[66]. However, both options have some disadvantages. When the temperature is increased over 50ºC, the reactivity of the attack grows. This effect allows the catalyst particles to remove faster the silicon beneath them and, therefore, suppresses the preferential growth in the [100] direction. However, the increased reactivity of the attack activates a secondary etch which affects the walls of the nanowires, obtaining porous nanowires, **figure 3.3B**.

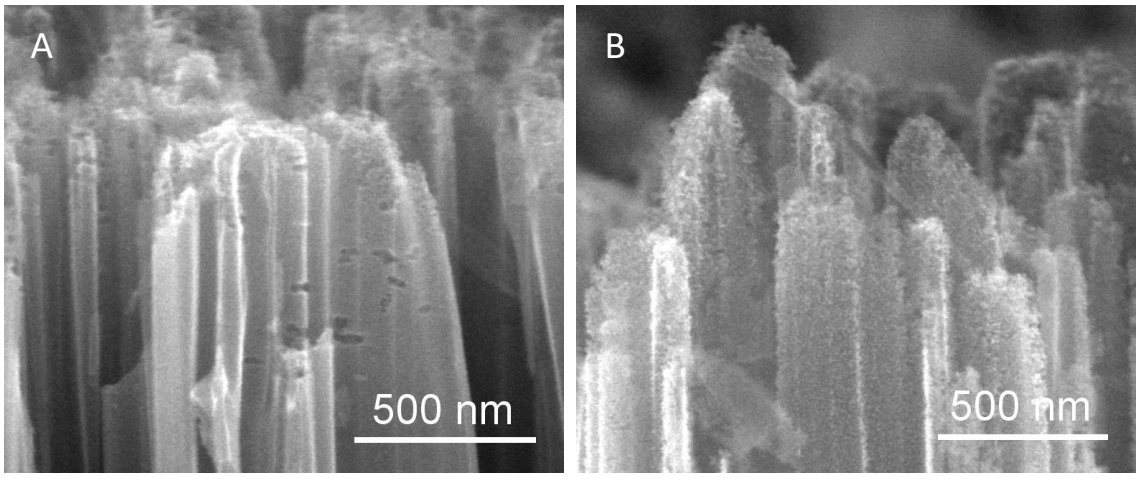

Figure 3.3 FESEM images of A), tips of SiNWs grown at 25 ºC and B), tips of SiNWs grown at 50ºC.

On the other hand, it is possible to suppress the etching in the preferential direction when the catalyst forms a continuous layer. This is due to the reduction of degrees of freedom of the catalyst, forcing the layer to move perpendicular to the surface rather than slanted[66]. However, the electroless deposition method does not allow the formation of a continuous layer, and instead, by increasing the deposition time, only bigger catalyst nanoparticles are achieved. This effect can be clearly observed in **figure 3.4**. When short deposition times (15 s) are applied, **figure 3.4A**, small AgNPs cover the surface. Their size distribution, **figure 3.4D**, is centered in 200 nm and is quite narrow despite of their irregular shapes. If the deposition is prolonged in time (45 s), **figure 3.4B**, the particles grow considerably achieving an average size of 500 nm but with a wider size distribution, **figure 3.4E**. When very long deposition times (2 minutes) take place, **figure 3.4C**, the mean size of the particles grow up to 700 nm keeping a wide size distribution, **figure 3.4F**. After this long deposition times, the Ag NPs also grow upwards forming 3D dendritic structures above the surface of the silicon. The commented behavior can be seen in **figure 3.4C**, where an incipient growth upwards is observed.

It is necessary to point out that the shapes or sizes of the Ag NPs deposited by electroless deposition are not exactly transferred to the silicon (and the nanowires). When the Si substrate, with the Ag NPs, is immersed into the second bath of the MACE process, the Ag NPs suffers a dissolution in the presence of HF/H_2O_2[13]. This dissolution leads to a notable size reduction and a shape transformation to spherical shaped NPs[67] which sculpt the nanowires. The mentioned effect is even more noticeable in the 3D structures formed above the Si, after the immersion in the second bath, this structures get dissolved and just the Ag NPs in contact with Si can be found.

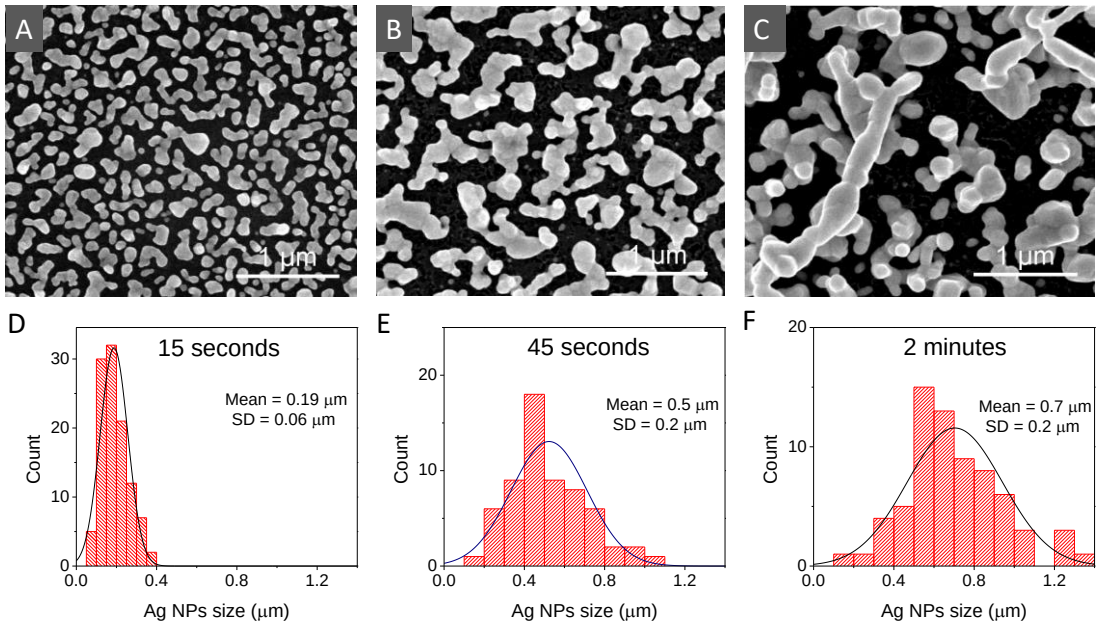

Figure 3.4 FESEM images of AgNPs deposited after 15 s (A), 45 s (B) and 120 s (C) by electroless deposition method. Corresponding size distribution histograms (D-F).

In the view of the above exposed, it can also be concluded that the electroless deposition method is not valid for the creation of a continuous catalyst layer, being necessary to move to physical deposition methods involving patterns, which makes the process much more complicated.

3.3.2 Chemical characterization of the SiNWs

As it was exposed in the introduction, a quite remarkable attribute of the MACE method is the low modification of the properties from the starting material. This result has been previously shown in TEM images of **figure 3.2**, where the nanowires keep the same crystallinity as the substrate. However, in **figure 3.2A-B** it can also be seen an amorphous layer wrapping the SiNWs of a thickness around 5 nm. The composition of this amorphous layer is relevant, because this type of chemical etch can indeed produce an oxide layer or the amorphization[68] of the surface of the nanowires. To investigate the chemical nature of the layer, the as-produced samples were analyzed by XPS and TEM-EDX. XPS results in **figure 3.5A**, referenced using the carbon peak, show an important contribution at 103.6 eV, what can be identified as Si-O bond. This clearly indicates the presence of silicon oxide on the surface. Also, in this XPS analysis it can be identified the Si-Si bond at 99.4 eV and the so called "Organic Si" at 102.4 eV. This "Organic Si" corresponds to the Si-H_x, Si-O-C and Si-OH bonds[69], attributed to surface terminations of the silicon due to the chemical etching and the interaction with atmosphere.

In agreement with XPS results, the TEM-EDX analysis of the core and external amorphous layer, **figure 3.5B**, points out a large amount of oxygen in the wrapping layer, while almost none in the core. Despite EDX results are mostly qualitative, the silicon oxide presence obtained from the XPS can be associated to the amorphous layer observed by TEM-EDX.

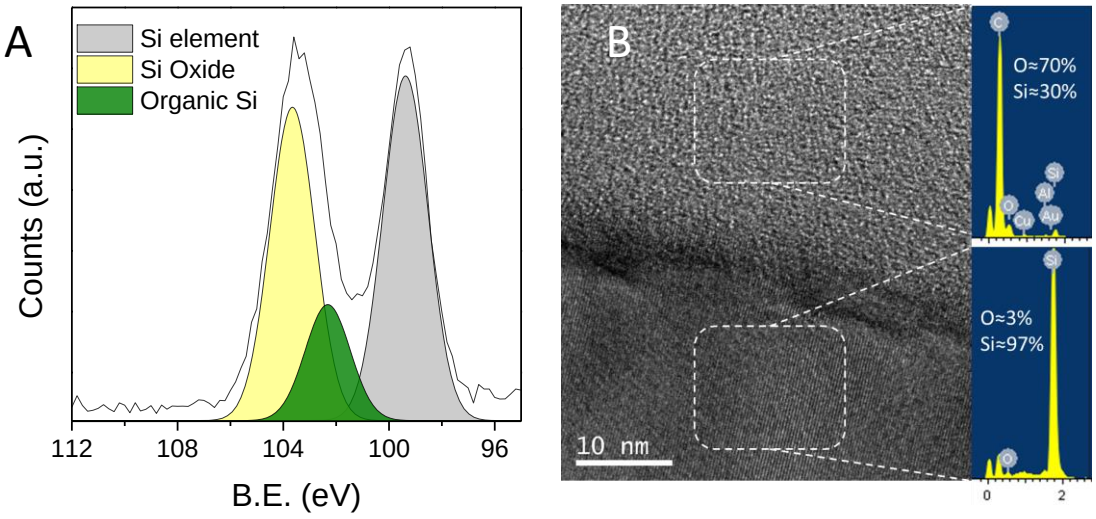

Figure 3.5 A) Si2p XPS spectra of as-synthetized SiNWs. B) TEM image of core (bottom) and amorphous layer (top) of a nanowire, and inset, EDX analysis of marked areas.

3.3.3 MACE reaction kinetics

Another great advantage of the MACE method is that the length of the SiNWs can be easily controlled by the etching time. Temperature also plays an important role on the MACE process, highly affecting the etching rate. Therefore, it is necessary to study the influence of the temperature in the kinetics of the reaction in order to further control the growth of the SiNWs. This study has been performed, **figure 3.6A**, selecting three temperatures: 50ºC, 30ºC and 8ºC, and measuring the length of the nanowires from FESEM cross-section images of the samples. As expected, the analysis shows that when the temperature of the reactants is increased, the etching rate also increases, obtaining values of 23 nm/s, 10 nm/s and 3.3 nm/s for the mentioned temperatures respectively. From this rates of grow, an Arrhenius plot can be obtained[70], **figure 3.6B**.

$$\ln(k) = \ln(A) - \frac{E_a}{R}\left(\frac{1}{T}\right) \qquad \textbf{Equation 3.1}$$

The slope of the graph, according to Arrhenius equation, **Equation 3.1**, where k is the rate constant (rate of grow in our case), A the pre-exponential factor, R the gas constant and T the temperature, is related with the activation energy (E_a) of our process. This activation energy was found to be 0.359 eV, in a very good agreement to other similar systems in the bibliography[70].

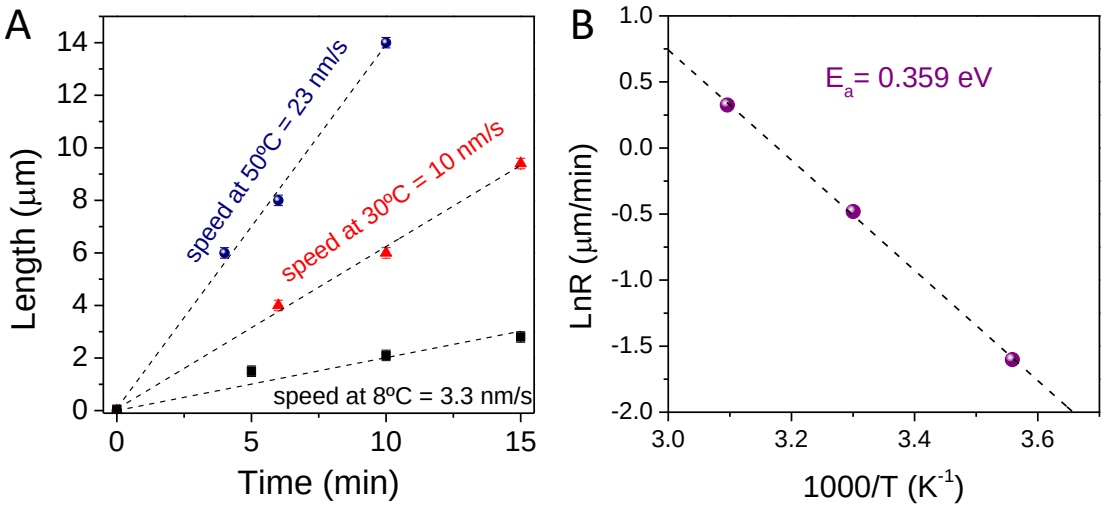

Figure 3.6 A) Graph of the lengths of the nanowires vs etching time, for different temperatures. B) Arrhenius plot of the obtained rates of grow shown in A).

3.3.4 Anti-reflective properties of the SiNWs-covered surface

After a thorough morphological, structural and chemical characterization of the SiNWs and the subsequent extensive description of the etching process and its parameters, the SiNWs were tested as antireflective coating.

For that purpose, 10 µm long SiNWs were grown on (100) c-Si wafers and its hemispherical reflectance was obtained. For comparison, the starting wafer and a commercial solar cell (REC), were also measured in the same conditions, **figure 3.7** top. It is worthy to say that the commercial solar cell was provided with an antireflective etching treatment and an

antireflective SiN_x layer. Moreover, the measurement of this commercial cell was performed avoiding the contact fingers which could increase their reflectivity. As can be seen in **figure 3.7** top, the reflectance is dramatically reduced when the SiNWs were grown on top of the silicon wafer, obtaining an average reflectance in the 250-1000 nm wavelength range, lower than 1%. This value is significantly lower than the commercial solar cell tested, which has an average of 5% in the mentioned range, without taking in to account the peak centered in 370 nm. In fact, the reported value is even lower than those shown in the literature[71–73].

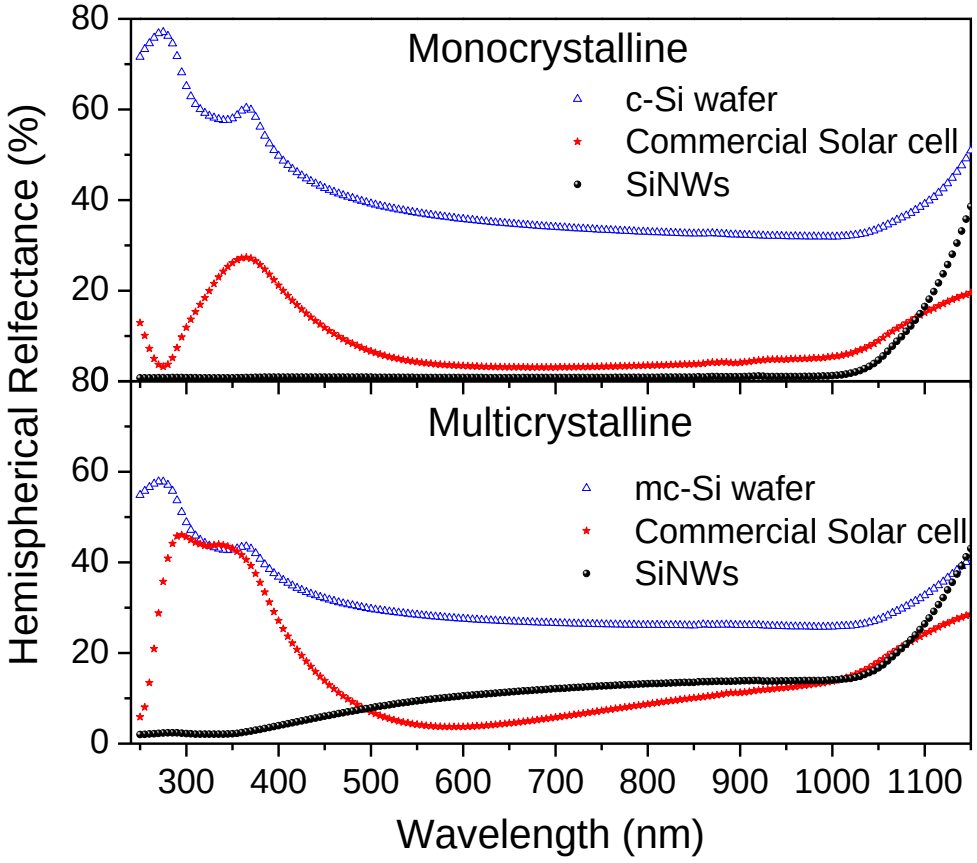

Figure 3.7 Hemispherical reflectance measurements on monocrystalline samples (top) and on multicrystalline samples (bottom).

A similar analysis was performed on the SiNWs grown on the mc-Si, **figure 3.7** bottom. The length of the SiNWs were 10 μm and, doing as before, the starting substrate and a

commercial multicrystalline solar cell were measured to make a comparative study. In this case, the starting substrate was not polished, so the reflectance reduction when the SiNWs are grown is not as sharp as in the c-Si case. Even so, the reduction it is still remarkable. On the other hand, when the SiNWs are compared with the commercial cell (GINTECH), the last one shows a better performance for wavelengths higher than 500 nm, while the SiNWs have better response below this wavelength. Still, the average reflectance in the 250-1000 nm range was lower for the SiNWs.

The higher reflectance of the SiNWs in mc-Si compared with the SiNWs on c-Si, is related with the presence of different crystalline orientations in the mc-Si. When there is a crystalline orientations different to the {100}, the SiNWs grow slanted. The slanted SiNWs have a bigger amount of surface facing the incoming light and, therefore, show a higher reflectance.

The results shown in **figure 3.7** proof the usefulness of the MACE method for obtaining highly absorbing surfaces. These SiNWs covered surfaces can match, or even surpass, other more complex anti-reflective solutions which usually involves numerous steps and layers.

3.4 Conclusions

As conclusions of the chapter the following results can be highlighted:

The MACE used for SiNWs growth has a preferential etch direction in [100] regardless of the crystalline orientation of the surface. The mentioned fact implies that when the MACE is applied over a surface with a crystalline orientation {100}, straight SiNWs are obtained. However, if it is applied in a surface different from the {100}, the SiNWs grow slanted.

It was also obtained by XPS and EDX-TEM analysis, that the SiNWs synthetized have a crystalline core surrounded by a thin silicon oxide wrapping layer.

Furthermore, a detailed study on the kinetics of the MACE has been accomplished. The etching rates corresponding to different temperatures, as well as an activation energy of 0.359 eV for the etching reaction, were obtained.

To conclude, the SiNWs have been tested as antireflective layer, obtaining an average value lower than 1% for nanowires grown in c-Si and lower than 10% for the ones grown on mc-Si. These values are extremely low and they are even better than the ones of actual commercial cells.

Chapter 4:

CNTs as conductive and transparent layers

4.1 Introduction

In the previous chapter, the SiNW-covered surfaces have proven to be a very good anti-reflective layer, being even better than some commercial options. However, for their application in solar cells is not only necessary to have a good absorption, but also the quality of the surface plays a very important role. When a photocarrier is generated in a solar cell, in order to contribute to the current generation, it has to be gathered before it recombines. The surface impurities, or even the dangling bonds of the surface, can act as traps where the photocarrier can get caught and recombined before being collected. This effect is called surface recombination and can highly affect the efficiency of a solar cell[74]. In fact, the mentioned effect is one of the biggest drawbacks of the SiNWs. The massive increase of surface, due to the formation of the nanowires, leads to an increment of the surface recombination[75]. For this reason, it becomes necessary to find an effective way to mitigate this effect. It can be done through two approaches: passivating the surface or collecting the photocarriers in shorter distances.

The work in this chapter focuses on the second approach. For this purpose, usually transparent and conducting oxides (TCOs) layers are used. However, in the SiNWs case, their sharp shape and low separation do not allow the formation of a proper film[73], which

leads to low efficiency problems. Therefore, it is necessary to substitute the TCOs with another material with similar properties, and which can be adapted to the SiNWs surface. For this purpose, carbon nanotubes directly grown over the SiNWs by a CVD process, have been investigated. A full chemical and structural characterization of the nanotubes have been performed and their conductive and transparent properties have been analysed.

4.2 Experimental

The growth of the CNTs was performed on a CVD system using alcohol as carbon source and the bimetallic Co-Mo nanoparticles as catalyst[76]. The growth was carried out on SiNWs-covered surfaces. The CNT growth method consists of two consecutive steps. Firstly, the bimetallic catalyst was deposited on the surface of the sample by dip-coating into Mo and Co acetate solutions. After each dip-coating, the samples were calcined at 400ºC for 4 minutes. The molybdenum acetate solution had 0,02 g of $Mo(CH_3COO)_2$ salt per 100 ml of absolute ethanol, and cobalt acetate solution had 0,04 g of $Co(CH_3COO)_2 \cdot 4H_2O$ salts per 100 ml of absolute ethanol.

After catalyst deposition, the synthesis of the CNTs was made using a thermal CVD system at atmospheric pressure. Samples were placed inside the reactor and heated up to 800ºC under a 750 ml/min argon and 75 ml/min hydrogen flow during 24 minutes, in order to reduce the catalyst. Then, argon plus hydrogen flow was replaced with a nitrogen mixed with ethanol flow, **scheme 2.2**. This flow was kept constant for 20 minutes at 800ºC. After this time, the system was cooled down to atmospheric temperature under an argon flow. A schematics of the thermal treatment process is shown in **scheme 4.1**.

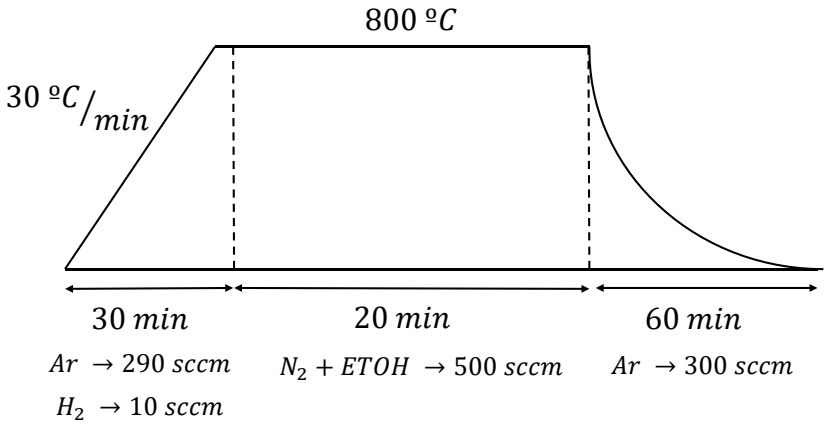

Scheme 4.1 Flow and temperature diagram of the growth process of the CNTs.

In order to extract the electrical properties of the CNTs, some SiNWs samples were subjected to a wet oxidation in the thermal CVD furnace. The samples were placed in the reactor which was heated up to 900ºC under N_2 flow of 500 sccm. Once the temperature reached the 900ºC, to the N_2 flow, water was incorporated through bubbling similarly as ETOH in **scheme 2.2**. The process is summarized in **scheme 4.2**.

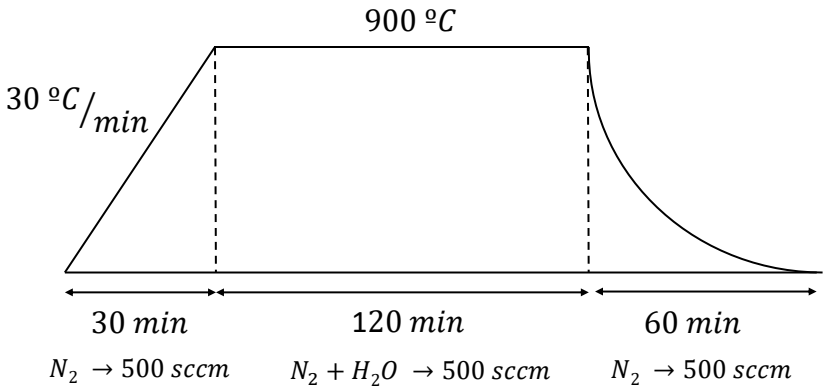

Scheme 4.2 Diagram of the wet oxidation process in CVD furnace.

4.3 Results and discussion

4.3.1 Morphological characterization

The growth method used generally produces vertically-aligned single-walled carbon nanotubes[76,77] when planar silicon or quartz substrates are used. However, in this case, the singular morphology of the silicon nanowires leads to the formation of an interconnected net, **figure 4.1A**. This net formation may come from the fact that the catalyst nucleation sites are in the side-walls and peaks of the SiNWs. These surfaces are rather parallel one to each other, so when the CNTs grow perpendicular to them, they find a neighboring wall or peak to which they get attached, interconnecting all the SiNWs. As result, the whole "forest" of nanowires is inter-connected by their uppermost points through the CNT net.

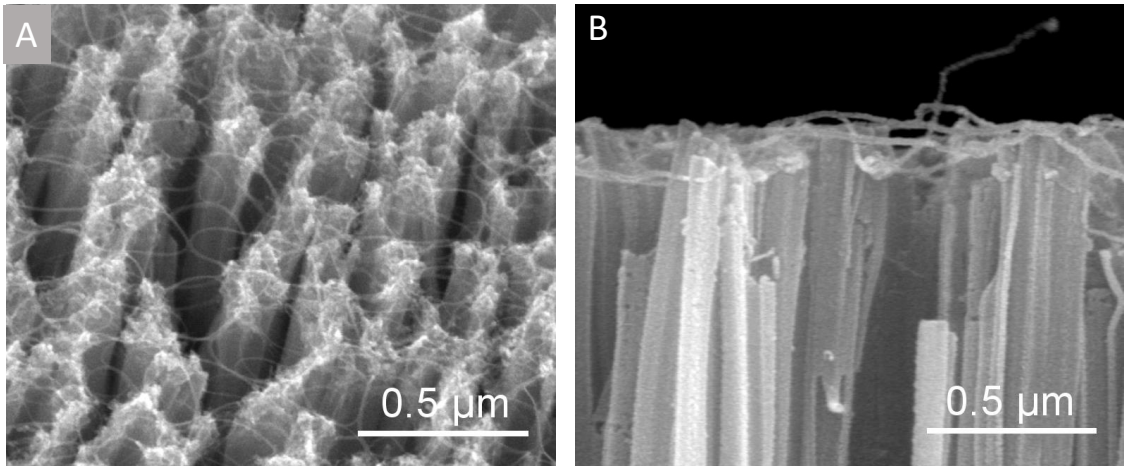

Figure 4.1 FESEM images of the CNT nets grown on SiNWs, top-view (A) and cross section (B).

It was also found that the net only grows very close to the top surface. The depth where the net is usually find is less than 200 nm, **figure 4.1B**. It is necessary to point out that in **figure 4.1B**, a 5 nm Au layer was deposited to improve the visibility of the CNTs. Therefore, the apparent thickness of the CNTs in the image is not representative of their true diameter.

4.3.2 Structural characterization

The structural characterization of the carbon nanotubes is essential due to the fact that both optical and electrical properties of the surface depend significantly on the type of nanotubes (single- or multi-walled). For this purpose, Raman spectroscopy have proved to be a very powerful tool, not only being capable of distinguishing between single and multi-walled CNTs, but also giving important details about their electrical nature. Raman spectroscopy was performed on the CNT net on SiNWs, obtaining spectra as shown in **figure 4.2A**. In this spectrum, the presence of the RBM, D, G and G' bands points out that the CNTs could be single- or double-walled[78]. However, the frequency at which the RBM appears (233 cm^{-1}) clearly indicates that the CNTs are single-walled[79].

$$w_B = A/d_t + B \qquad \textbf{Equation 4.1}$$

Additionally, the frequency of the RBM can be used to obtain the average diameter of the SWCNT from the empiric relation in **equation 4.1**. In this equation, the constants are typically $A = 234\ cm^{-1}$ and $B = 10\ cm^{-1}$ for SWCNTs bundles[78,80], leading to an average diameter of 1.04 nm.

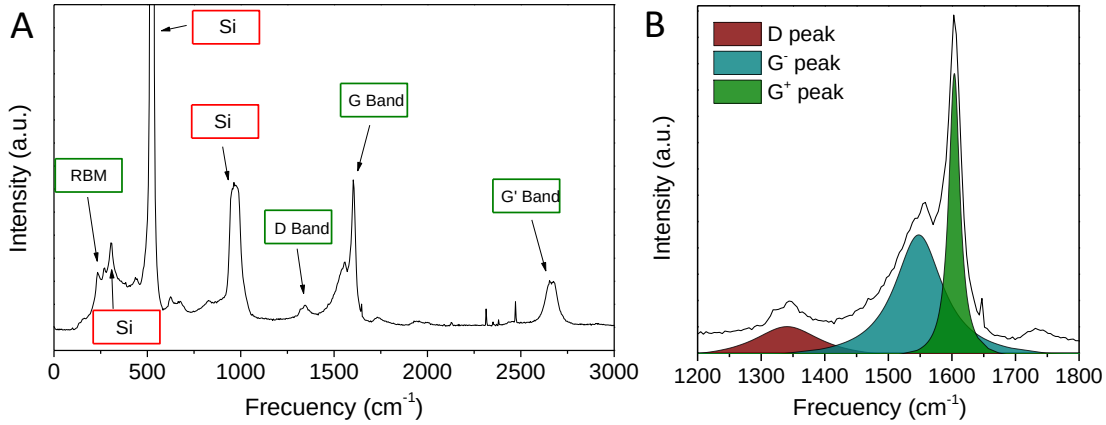

Figure 4.2 A) General Raman spectrum of the CNT net with the main vibrational bands of the CNTs marked in green and the ones corresponding to the silicon marked in red. B) the fitted D and G bands of the Raman spectrum.

On the other hand, the electrical nature of the nanotubes is given by the G and D bands. In particular, the deconvolution and fitting of the G band in terms of Lorentzian-shaped curves, **figure 4.2B**, can provide information about the electrical nature of the nanotubes. In this case, the Lorentzian shape of the G- peak and its low intensity relative to the G^+ peak, points out a predominant semiconductor behavior[78]. However, the widening of this Lorentzian shape also indicates the presence of nanotubes with metallic nature. It can be concluded that there is a mixture of both types of carbon nanotubes, a common result in large scale synthesis[81] due to differences in their chiralities[82].

The G and D bands can also provide information about the quality of the CNTs, as the ratio between their intensities can be used to get the defect concentration[78]. From **figure 4.2B** this ratio can be extracted, $I_D/I_G \approx 0.1$, indicating that the defect concentration is very low.

The fact that the CNTs are single walled, with some metallic behavior and high purity, is a great starting point for the application of this material as conductive and transparent films[83,84].

4.3.3 Optical properties

After Raman characterization, the optical properties of the CNT net were obtained by the analysis of hemispherical reflectance measurements. This technique was selected because the high absorption of the SiNWs would not allow the use of other techniques as transmittance configurations or ellipsometry. Two sets of samples were fabricated to isolate the contribution from the CNT net. The first set was composed by SiNWs samples with CNT net over them. The second one, SiNWs samples with all the CNT growth procedure but without introducing alcohol in the CVD during the growth. This way, the properties of the CNT net could be distinguished without introducing parameters associated to the lack of catalyst or thermal treatment. The results obtained are displayed in **figure 4.3**, where it can be seen that the reflectance of the sample with SiNWs is very low, decreasing even further with CNT net over them. From these results it can be obtained the absorption of the CNT

net by subtracting the SiNWs spectrum to the one of the SiNWs with CNTs. This absorption, in the 250 nm to 900 nm wavelength range, was lower than 1%. This means that the transparency of the CNT net is over the 99%, which is a good result in comparison with other results from the literature[83,85–87] with CNT layers. However, in transparent and conductive layers (TCL), there is always a trade between transparency and conductivity. Therefore, in order to compare our CNT net with other TCLs it is necessary to get its conductive properties.

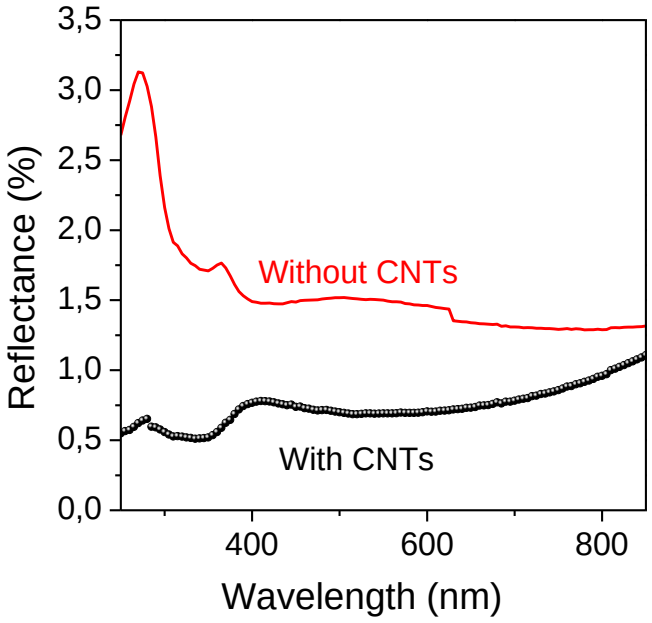

Figure 4.3 Hemispherical reflectance of SiNWs-covered surface with and without CNTs grown on them.

4.3.4 Electrical behavior

In order to experimentally obtain the electrical properties of the CNT net, four-point probe measurements were performed. The measurements were done over samples in different stages of the CNT net grow and with different treatments. On **Table 4.1**, the results are summarized, where the reference Si corresponds to pristine silicon wafer substrate. The nomenclature Si +SiNWs corresponds to the pristine Si after the SiNWs growth. The Si

+SiNWs+CNTs corresponds to SiNWs samples with CNTs. The Si +SiNWs + SiO_2 corresponds to SiNWs samples heavily oxidized by a wet oxidation on a CVD. Finally, the samples Si +SiNWs + SiO_2 + CNTs were the oxidized samples with CNTs grown on them.

Table 4.1 Sheet resistance values of samples in each step of the CNT net growth process

Samples	Average Sheet Resistance (Ω/□)	Standard Deviation (Ω/□)
Si	70	5
Si + SiNWs	80	5
Si + SiNWs +CNTs	3000	500
Si + SiNWs + SiO_2	∞	
Si + SiNWs + SiO_2 +CNTs	3200	500

It was found that all samples with carbon nanotubes shown the same sheet resistance (R_S), regardless of the substrate on which they were grown. This can be easily seen in **Table 4.1**, as samples Si +SiNWs+CNTs and Si + SiNWs + SiO_2 + CNTs have almost the same R_S value, despite their substrates had very different resistance value. The mentioned fact is even clearer when comparing the oxidized samples Si +SiNWs + SiO_2 with the Si +SiNWs + SiO_2 + CNTs. Before the CNT growth, the R_S of the oxidized sample was so high that it was impossible to measure. After the CNT growth, its R_S value changed to 3.2 kΩ/□, a value in the range of the other of our samples with CNTs. This proves unequivocally that the measured R_S value of 3 kΩ/□ was the one of the CNT net without any interaction from the substrate. A very low value for such a thin (nanometric size) and transparent layer (~99%). Despite the obtained R_S value is in the range of those reported by other groups in the literature[83–87] , the low absorbance value measured leads to a better relationship between transparency and R_S. Probably one of the reasons why this relationship is better, is because our procedure creates an interconnected net from the beginning, while in other procedures the individual CNTs are grouped in the deposition[83,85]. Also, as the CNTs have been grown

directly over the surface of the SiNWs instead of being deposited, the contact between the SiNWs and the CNTs is expected to be better.

In spite of the good results achieved, there are still some drawbacks that have to be taken in account. The obtained R_S is still considerably higher than the ones shown by the TCOs, which are in the range of hundreds of Ω/□. To further improve the R_S values of the CNT net it would be necessary to increase the density or thickness of the CNT net. However, in the tested conditions, the presented growth method does not allow the control of these parameters. This should be the objective of future research on the subject.

Opposite to this drawback, the reported method offers a simple way for obtaining a low resistance and high transparent film over a surface where the TCOs cannot be used.

4.4 Conclusions

Carbon nanotubes (CNTs) were synthetized by alcohol catalytic chemical vapor deposition (CVD) on SiNWs previously grown by MACE. By the selected growth method, a shallow, continuous and interconnected CNT net was obtained on top of the SiNWs. The CNTs were analyzed by Raman revealing a single-wall structure with an average diameter of 1 nm. Moreover, further analysis of CNTs Raman spectra shown a very low defect concentration and a mixed conductive-semiconductive nature.

The transparency and sheet resistance of the CNT net have been investigated by hemispherical reflectance and four-point probe respectively. It was obtained an excellent compromise between light absorption and conductivity, being comparable, or even better, than other methods in literature.

This layer has demonstrated to be a valid substitution of the TCOs, which are hardly applicable in the SiNWs surface.

Chapter 5:

SiNWs growth with patterns

5.1 Introduction

In the previous chapter the high recombination problem of the SiNWs was addressed by reducing the path that the photocarriers have to travel before being collected. However, as it was mentioned before, there is a more direct approach to this problem, the reduction of the recombination through surface passivation. Passivation of silicon is usually achieved by the deposition of thin dielectric layers such as SiC_x, SiN_x[88], a-Si:H[89] or Al_2O_3[90]. These layers fill the dangling bonds of the surface, which act as traps for the photocarriers, reducing the recombination process. Nevertheless, the sharp shape of the SiNWs hinders the proper deposition of any type of layer. Moreover, the low separation between the SiNWs does not allow a full coverage of their surface, leading to an inefficient passivation[91]. In order to avoid these problems, some attempts have been made using thermally grown SiO_x as passivation layer[92]. However, it was found that the segregation of impurities to the oxide layer neutralized the passivation effect[92], making this option not feasible.

All these difficulties require a new approach to the problem. The lack of control of the SiNWs separation prevents an efficient passivation of the surface, then, this chapter focuses on the development of an effective way to control the SiNWs diameter and separation. The applications of SiNWs with controlled characteristics are not restricted to solar cells. Other fields such as energy storage, nanoelectronics and nanophotonics can get benefit from the diameter control, as very thin (~5 nm) semiconducting nanowires have proven to be

promising building blocks for future FETs[93,94] , LEDs[95,96], lithium ion batteries[97] and many other nanodevices[12].

In order to achieve the desired controllability, in the present chapter, patterns are used for the catalyst deposition. As it was highlighted in the introduction chapter, by controlling the pattern of the catalyst, the morphology of the SiNWs can be effectively modified. In the literature, numerous methods have been used to create an appropriate pattern[5,13]. One of them is the anodic aluminum oxide membrane (AAO). The AAOs have been extensively used as patterns in numerous applications[98], due to the precise controllability of their pores and interpore distances through growth paremeters[99–101]. Traditional two step AAOs, grown on Al foils, have been previously used in conjunction with the MACE to obtain SiNWs[102]. However, in the present work, it is explored an effective but largely unused method to directly grow the AAOs over the surface of the Si[103,104] for the growth of patterned SiNWs.

5.2 Experimental

The synthesis of the AAO was performed over a p-type (1-10 Ωcm, Boron doped, 300 μm) <100> monocrystalline silicon wafer. First, the substrates were cleaned following the procedure described in chapter 1, which consists on the consecutive sonication in acetone, IPA and DI water followed by a 30 minutes bath in piranha solution and ending with an oxide removal in HF 5%. After cleaning, the Si substrates were introduced in a magnetron sputtering equipment (described in chapter 2, section 2.1.2) and high vacuum ($1x10^{-6}$ torr) was reached. The deposition of Al was performed using an Al 99.999% target (Goodfellow), at a pressure of $1x10^{-2}$ torr, with an Ar 99,99995% flow of 3 sccm and a RF power of 120 W. Deposition was performed at room temperature. In order to improve adhesion, after the Al deposition, samples were annealed in a tubular CVD furnace at a fixed temperature of 350ºC

for 2 hours under a 500 sccm N_2 flow. A diagram of this annealing is displayed in **scheme 5.1**.

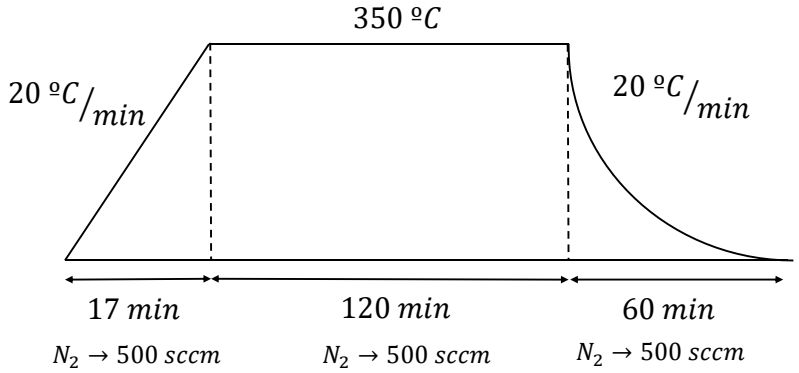

Scheme 5.1 Diagram of the annealing process of the Al in a tubular furnace. The duration of each step, temperatures and fluxes are displayed in the scheme.

Subsequent to the annealing process, the samples were ready for the two step AAO membrane formation. The anodizations were conducted in different electrolytes, temperatures and voltages which are described in the results section of the chapter. The anodization time was adjusted for the thickness of the deposited Al. For thicknesses of 300 nm, the duration of the anodization was settled to 200 seconds. Each anodization transforms approximately half of the deposited Al, accordingly to our observations and the previously reported AAO grow rates[98]. After the first anodization a poorly ordered membrane is generated, **figure 5.1A**. The irregular AAO is removed by a CrO_3 1.6% and H_3PO_4 6% etching solution at 20ºC for 30 minutes. The CrO_3/H_3PO_4 solution just eliminate the Al_2O_3 of the membrane, leaving shallow pits on the Al layer that will contribute to a better ordering in the second anodization. Consecutively to this oxide removal, the second anodization was conducted with the same electrolyte, temperatures, voltages and duration of the first anodization. As a result, a highly ordered AAO membrane is obtained, **figure 5.1B**.

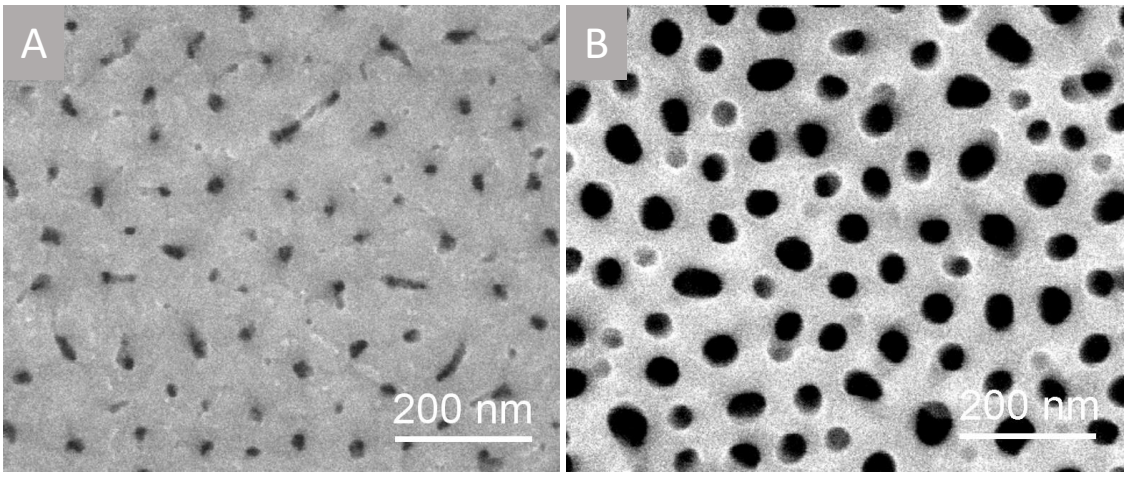

Figure 5.1 Top view FESEM images of the AAO after first anodization, A) and second anodization B).

Subsequent to the AAO formation, the catalyst was deposited on top of the membrane. Two catalyst were tested: Au and Ag. The Au was deposited with a pulsed plasma sputtering (Quórum, Q150T-S) and the thicknesses were ranged between 10 and 20 nm. The Ag film was also grown by sputtering with thicknesses ranged between 10 and 30 nm.

Once Au or Ag were on top of the membrane, the etching of the MACE was conducted. For this process, only the HF/H_2O_2 solution was used. Different molar ratios ($\varepsilon = [HF]/[H_2O_2]$) were applied to Au and Ag catalysts; for Ag it was ε=24 (the same as in chapter 3) and for Au was ε=10. The use of different ε in each system, is due to the higher catalytic activity of Ag in the reduction of the H_2O_2. Therefore, to keep similar etching rates with both catalysts, the amount of H_2O_2 was increased for the Au.

After the growth of the SiNWs, the catalysts were removed. The Ag was removed by a 30 minutes bath in 65% nitric acid and the Au by a 30 minutes bath in *Agua Regia* (HNO_3/HCl in a volume proportion 1/3).

A complete scheme of the whole process is displayed in **scheme 5.2**.

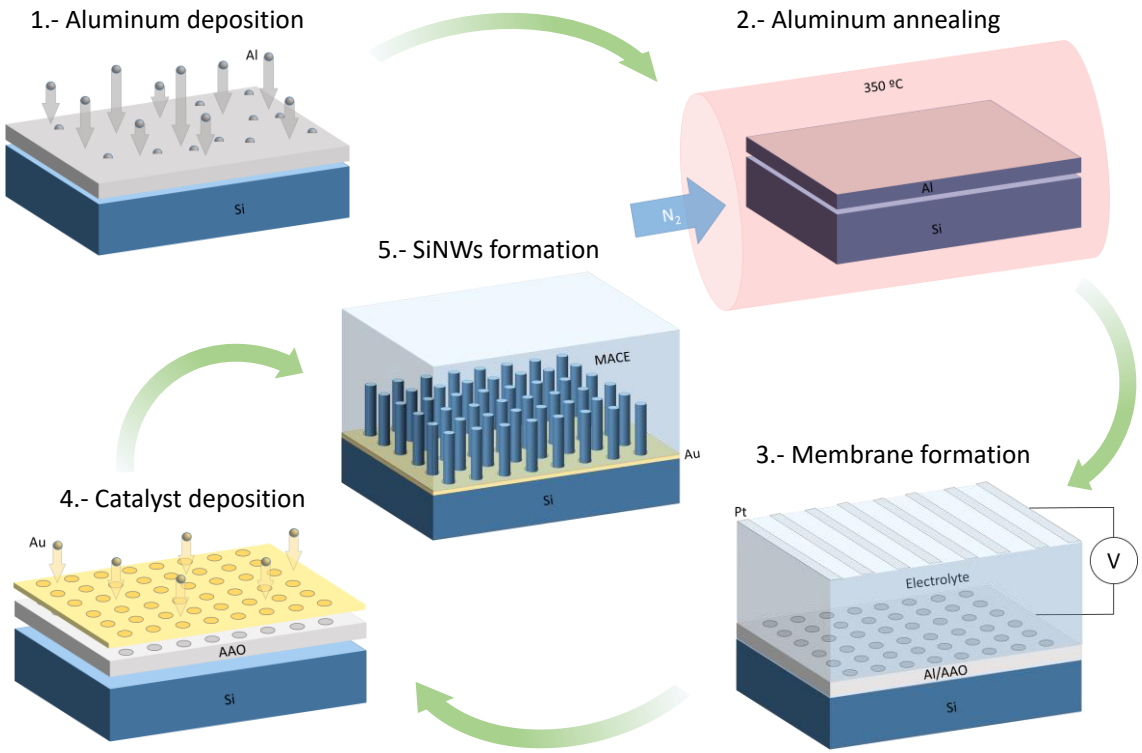

Scheme 5.2 Diagram of the steps performed for the synthesis of AAO patterned SiNWs

5.3 Results and discussion

5.3.1 AAO membranes: parameters and control

The traditional AAO procedure in Al foil usually begin with the electropolishing of the surface[105]. This pretreatment of the substrate improves the order of the final AAO, as any roughness or defect can disrupt the self-assembly process, leading to an alteration of the pore arrangement[98]. However, in deposited Al layers the application of this electropolishing resulted in the peeling off of the whole Al layer. For this reason, the purity of the surface has to be controlled during the deposition of the Al layer. If the roughness of the layer is too high, **figure 5.2A**, the anodization process results in a very poorly ordered pore array and irregular pores shapes, **figure 5.2B**. However, if the roughness is reduced, **figure 5.2C**, the arrangement of pores is more ordered, as well as the pores shape, **figure 5.2D**.

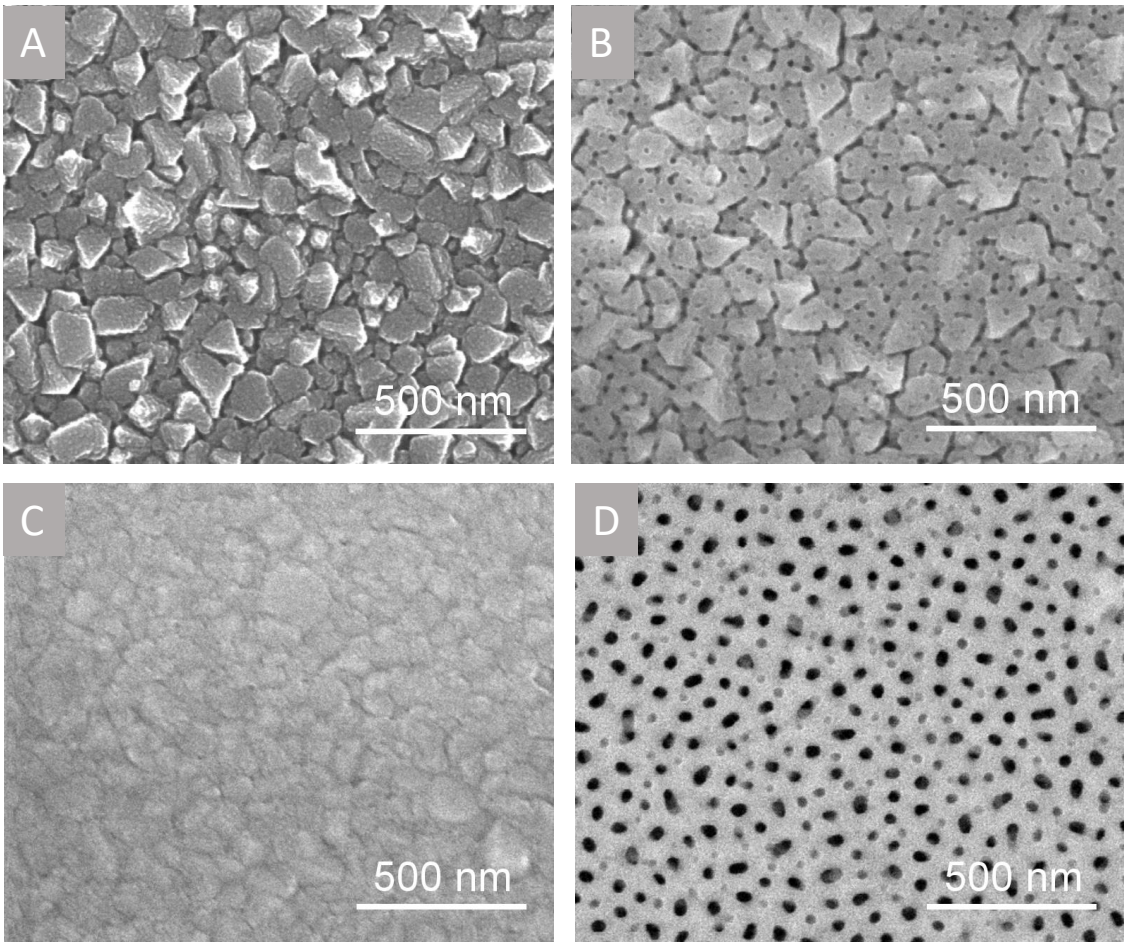

Figure 5.2 Top-view FESEM images of Al layers with different roughness before anodization (A and C) and after anodization (B and D). The AAO formation process for B and D was done with the same conditions.

Another important step previous to the membrane formation, is the annealing of the deposited Al. In AAOs grown on Al foil, annealing is not always necessary because the substrates usually have good crystalline structure. However, in deposited Al, this step is crucial. It improves the adhesion of the Al with the underlying Si substrate, making it harder to peel off during AAO synthesis.

The anodization process can be done with a large number of electrolytes[106], but the most commonly used are: sulfuric, oxalic and phosphoric acids. In Al foils, each of these acids have been reported to produce a determined pore diameter and separation[98]. Therefore, the sizes of the AAO features can be ranged from small ones, obtained with the sulfuric acid, to

bigger ones, produced by the phosphoric. This behavior is extremely useful as it provides a first approach for selecting the features of the membrane.

In order to check if the three mentioned electrolytes behave in the deposited aluminum as they do in the Al foil, a systematic study was performed to characterize their pore and interpore sizes. This study has not been found in the literature and it is fundamental because the Al/Si system is quite different from the Al substrate. One of the most important differences is the thickness limitation of Al in Al/Si systems. In Al substrates, the regular structures are achieved by long anodization times which consume large amounts of Al. However, in Al/Si the anodizations are restricted to the amount of Al deposited, making more difficult the achievement of structures as regular as in Al substrates. As a consequence, AAOs in Al/Si show a wider size distribution which is necessary to obtain. The study of the size distribution was performed using the standard voltages for each electrolyte, being 25 V for the sulfuric acid, 40 V for the oxalic acid and 60 V for the phosphoric acid. The temperature used was 10ºC and the anodization times and Al thicknesses were the same.

The results are displayed in **figure 5.3**. For the sulfuric acid it was obtained a narrow size distribution, both for the pore size, **figure 5.3B**, centered in 40 nm and the interpore distance (measured between centers) centered in 60 nm, **figure 5.3C**. In the case of the oxalic acid, the diameter distribution is also very narrow, centered in 55 nm, **figure 5.3E**, but the distribution of the interpore distance is wider, centered in 80 nm, **figure 5.3F**. The phosphoric acid shows a wide size distribution both for the diameter, **figure 5.3H** and interpore distance, **figure 5.3I**, having their mean value at 90 nm and 140 nm respectively. In SEM images it can be observed a regular rounded shape for the membranes grown in sulfuric and oxalic acids (**figure 5.3A** and **figure 5.3D** respectively), while the phosphoric acid shows a much more irregular pore shape, **figure 5.3G**. All the histograms shown in

figure 5.3 were made by measuring at least 140 distances (diameters or interpore) from FESEM images of different areas along the membrane.

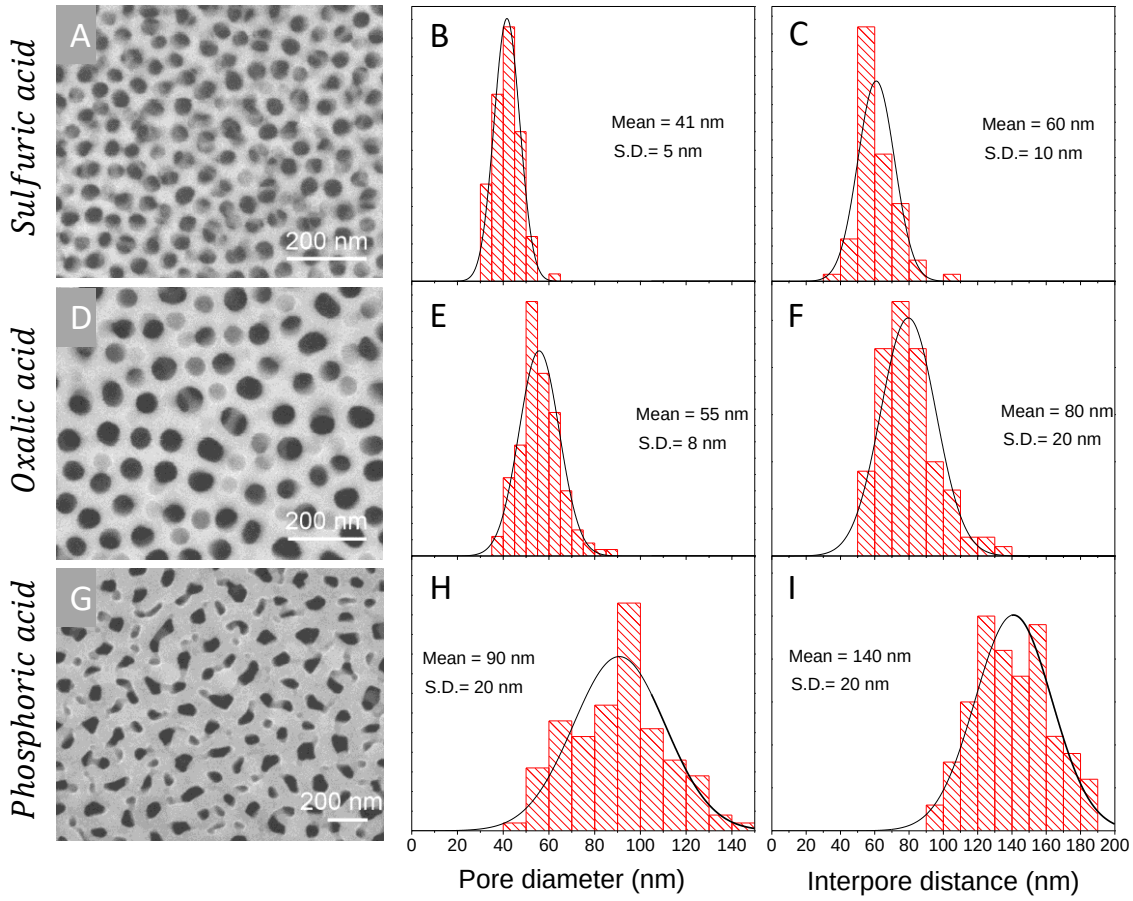

Figure 5.3 Top-view FESEM images of membranes grown in sulfuric A), oxalic D) and phosphoric G) acids. B), E) and H) are pore diameter histograms of the AAO grown with the mentioned electrolytes. C), F) and I) are interpore distance histograms of the AAO grown with the electrolytes displayed in each histogram.

Analogously to Al substrates, the AAOs in Al/Si show an increasing pore diameter and interpore separation with the use of sulfuric, oxalic and phosphoric acids. However, there are significant differences in the manner these acids influence the AAO features produced in Al/Si. The first important observation is that the 10% porosity rule of the AAO membranes[107] is not followed. This rule stablishes that the self-ordering of the AAO membranes always leads to a porosity of the 10%, where the porosity of the AAO is

determined by the **equation 5.1**, being P the porosity, r the pore radius and d_i the interpore distance.

$$P = \frac{2\pi}{\sqrt{3}}\left(\frac{r}{d_i}\right)^2 \qquad \textbf{Equation 5.1}$$

Nevertheless, it is no surprising that the 10% porosity rule is not followed in the present system, because this behavior is only observed in self-order regimes, in which pores forms hexagonal arrays. However, it was found that for the Al/Si system, all the samples lead to a same porosity value, but instead of being the 10% it was obtained to be the around 40%. The mentioned result indicates that the Al/Si system not only decreases the order of the AAO membranes but it also changes the relationship between pore diameter and interpore distance, inducing a porosity of 40%. It is important to mention the quite big error in the porosity, a 20%, due to the standard deviation of both diameter and interpore distances. This high error does not allow to set the 40% as an absolute value for the porosity. Nevertheless, is truly remarkable that all the samples analyzed both in this study and the ones in the following pages, led to a value very close to the 40%.

As it has been described, by choosing an appropriate electrolyte, a mean pore diameter can be selected. Furthermore, the pore diameters obtained with each electrolyte can be tuned by changing the anodization conditions. Voltage[99,108] and the temperature[108], are the factors that allow the change in the pore size and interpore distances. The influence of these parameters in the mentioned features are related with the interdiffusion of the Al^{3+} and O^- ions between the acidic electrolyte and the Al through the Al_2O_3. When the voltage grows, the electric field in the walls of the pores becomes stronger. The increased electric field permits the ionic species to reach further distances from the pore center, making thicker pore walls and enlarging the interpore distances. Also, voltage stimulate the electrolyte and allows the oxide removal during the grow stages, therefore, a higher voltage intensifies this effect, producing

bigger pores[108]. On the other side, the temperature increases the dissolution of the oxide as well as the diffusivity and availability of ionic species[108], affecting both diameter and interpore distances.

In **figure 5.4A**, it can be observed the influence of the voltage in the interpore distance, leading to an approximate augment of the interpore distance of 20 nm each 10V. This trend is kept for all the electrolytes, also there is a simultaneous increase of the pore diameter that keeps the porosity value constant at 40%.

Despite of the high tunability of the membrane parameters with the voltage, the range in which the voltage can be set for each electrolyte is very narrow, being typically 19-25V for sulfuric, 40-70V for oxalic and 60-90V for phosphoric[98,99,105] (in mild anodization conditions). In Al substrates, interpore distance and voltage are related by the well-known experimental expression, **equation 5.2**, being d_i interpore distance and U_a the anodization voltage[99].

$$d_i = -1.7 + 2.81U_a \qquad \textbf{Equation 5.2}$$

However, as it is shown in **figure 5.4A**, the samples grown in Al/Si systems does not follow the mentioned relationship and their linear adjustment has a considerable lower slope of $2.1 \pm 0.2 nm/V$. The obtained expression is extremely important, because it allows an easy manner to select the growth parameters for the desired membrane characteristics. Besides, the divergence of the data with the experimental model which applies in Al substrates, once more points out substantial differences between the both systems.

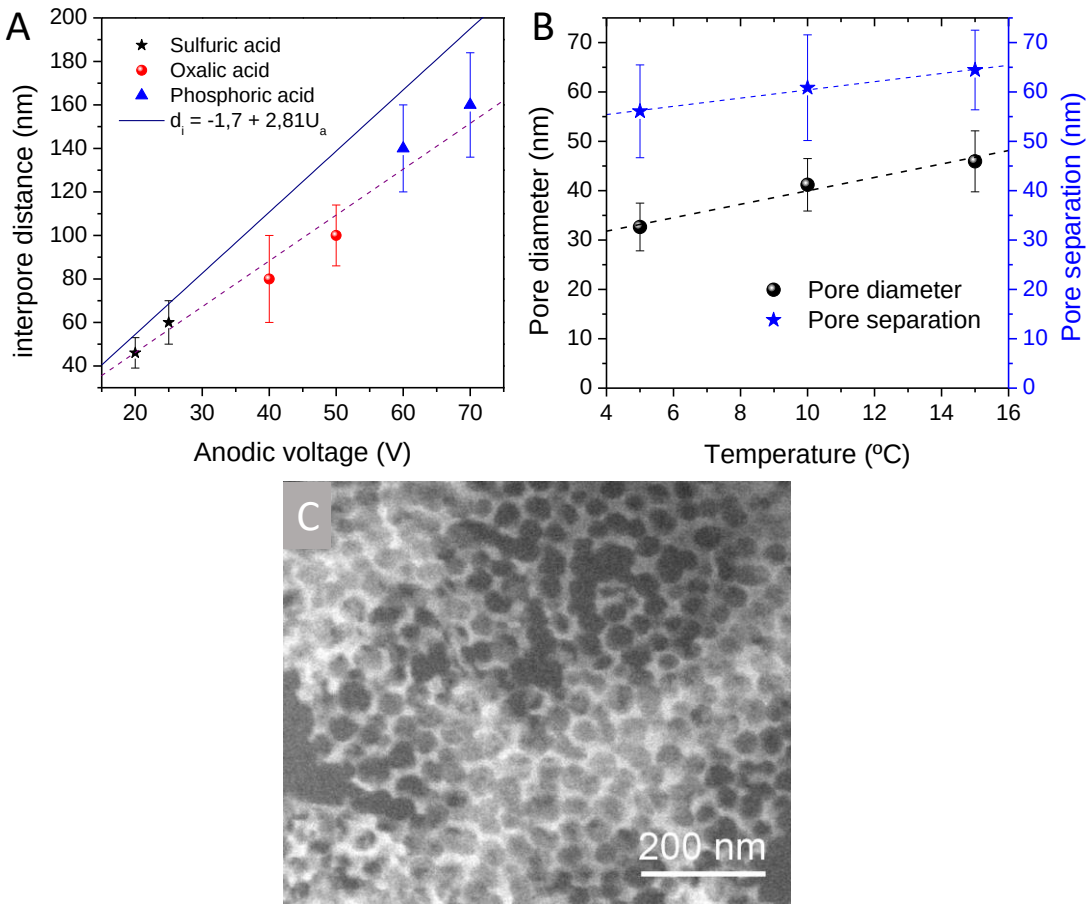

Figure 5.4 A) Interpore distances vs the voltage of the anodization of various electrolytes. The reference experimental relationship for the AAO grown in Al substrates is also displayed. B) Pore diameter and pore separation as a function of the temperature are represented. All samples were grown in sulfuric acid at a voltage of 25 volts. C) Top view FESEM image of the anodization made at 20ºC.

Figure 5.4B represents the pore diameter and separation as a function of the temperature of the anodization with sulfuric acid at the standard 25 V anodization process. It can be observed that the increase of the temperature can slightly change both interpore distance and diameter. However, it is worth to mention that the working temperature range is very narrow, and at temperatures as high as 20ºC, the membrane is destroyed, **figure 5.4C**.

The interpore distance can only be modified by changing the anodization conditions as it has been already shown. However, the pore diameter can be incremented by a post processing

of the membrane with a phosphoric acid treatment[109]. This acid is an Al_2O_3 removal that applied to the AAO membrane, slowly dissolve the pore walls increasing the pore diameters.

In order to obtain the pore enlargement rate of the treatment, the phosphoric acid was applied to an AAO grown with oxalic acid at standard conditions (10ºC, 40 V). The procedure was done at room temperature (20ºC) using a concentration of H_3PO_4 of 5%. Results are displayed in **figure 5.5**.

When the acid is applied for times lower than 40 minutes, a constant pore enlargement rate of 0.57 nm/min is found, **figure 5.5A**. For this range of treatment durations, all pores grow similarly, keeping almost the same size distribution, **figures 5.5B-C**. However, when the treatment durations are higher than 40 minutes, the trend is no longer followed, **figure 5.5A**. This behavior occurs because the diameter of the pore reaches its maximum value at the interpore separation. The mentioned fact is shown in **figure 5.5A**, where after almost an hour of acidic treatment, the diameter of the pores is limited to the mean interpore distance (80 nm). This result can be appreciated in **figure 5.5D**, where the walls separating the pores are very thin. However, histogram in **figure 5.5D** also shows some pores much bigger than the mean interpore distance. This is due to the excessive duration of the enlargement treatment, which destroy the walls between pores making double pores, **figure 5.5D**.

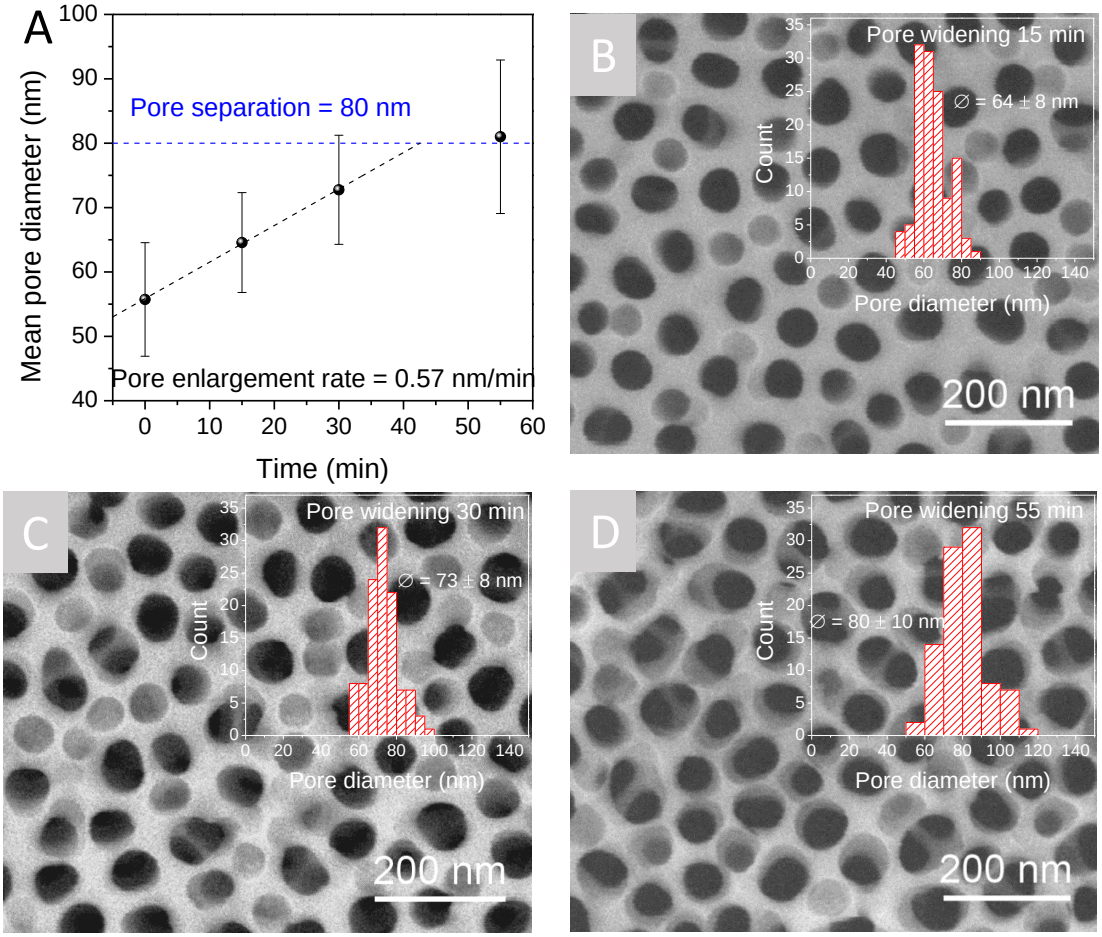

Figure 5.5 A) Mean pore diameter vs acidic treatment duration. B)-D) FESEM top-view images of membranes after the indicated pore widening treatment. Inset their corresponding histograms.

5.3.2 MACE on AAO membranes

In this section, the precise control of the AAO synthesis achieved, is used for the growth of patterned SiNWs by MACE.

As it was described in the experimental section of the chapter, previous to the etching bath of the MACE, the catalyst is deposited by a physical method over the pattern. Two catalyst were tested, Ag and Au. The first consideration to take into account is that the deposition of the catalyst produces a pore diameter reduction. The mentioned fact can be seen in **figure 5.6A-C**, were the as-produced membrane with a pore diameter of 39 nm, **figure 5.6A**, gets its diameter reduced to 33 nm after a catalyst deposition of 15 nm, **figure 5.6B**, and to 28

nm after a deposition of 30 nm, **figure 5.6C**. On average, it was found that the diameter reduction after the deposition of 15 nm of catalyst (that was stablished as the standard) was between 4-6 nm for both catalysts.

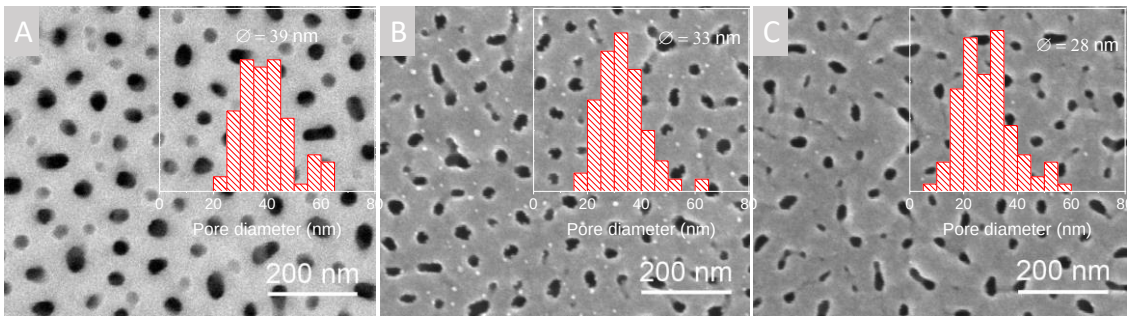

Figure 5.6 A) to C) top-view FESEM images of a same AAO membrane as-produced, after a catalyst deposition of 15nm and 30 nm respectively.

Both catalysts were tested in the next step of the procedure, the MACE process. It is worthy to mention that prior to using samples with the catalyst on the membrane, it was checked that the AAO membrane is removed when introduced into the MACE etching solution. Therefore, to put the catalyst in contact with the Si for the etching, no extra step has to be performed. Just introducing the membrane with the catalyst into the MACE etching solution should lead to the formation of a stand-alone catalyst membrane in contact with the Si. However, it was found that for the Ag this does not happen, the Ag layer lose the shape of the pattern very rapidly when introduced into the etching solution, **figure 5.7A**, no matter the thickness of the Ag layer. On the other hand, the Au keeps almost perfectly the shape of the membrane, **figure 5.7B**. The reason of the behavior of the Ag membrane into the MACE etching solution, is the low electrochemical potential of the Ag[13]. This leads to a dissolution/redeposition process that changes the shape of any deposited particle or layer to a rounded shape particle[67,110]. Then, the Ag under the tested parameters is not suitable for the pattern MACE method.

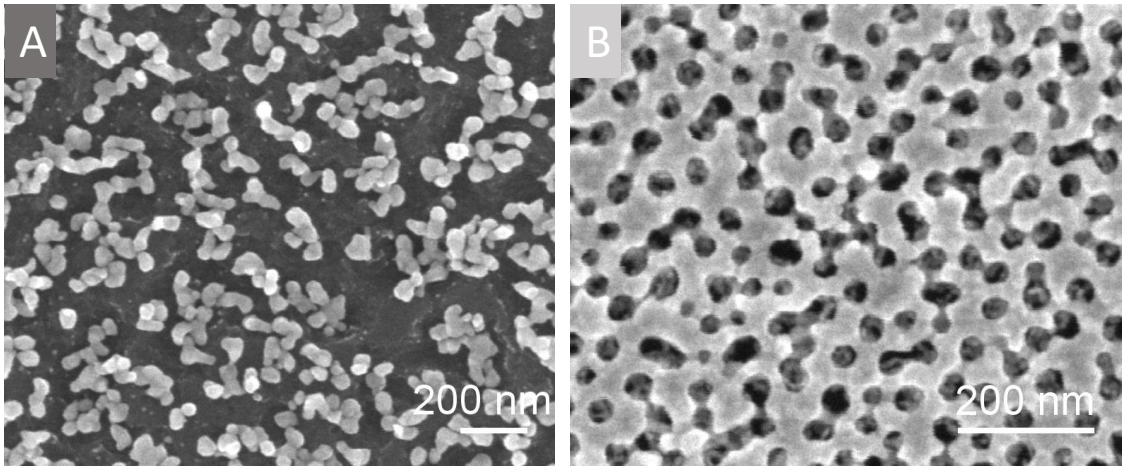

Figure 5.7 A) FESEM top-view image of an Ag deposition on a membrane after the MACE etching procedure and B) an Au deposition after the MACE etching.

During the first attempts applying the MACE with patterns, it was observed that the procedure led to a complete peel off of the membrane and catalyst, preventing the growth of SiNWs. Cross section FESEM images of the whole system Au/AAO/Si were taken, **figure 5.8**, in order to examine the interfaces between layers. It was observed that if anodization time is prolonged when the Al has been consumed, the inner Si gets modified, **figure 5.8A**. The voltage enhanced electrolyte probably oxidize the Si beneath the Al forming the observed porous layer. Once the sample is introduced into the MACE, this oxide layer is instantaneously removed by the action of the HF. This produces the observed peeling off the AAO with the catalyst. The mentioned problem can be solved by adjusting the anodization time to the Al thickness, **figure 5.8B**. This way no porous layer or peeling off were observed.

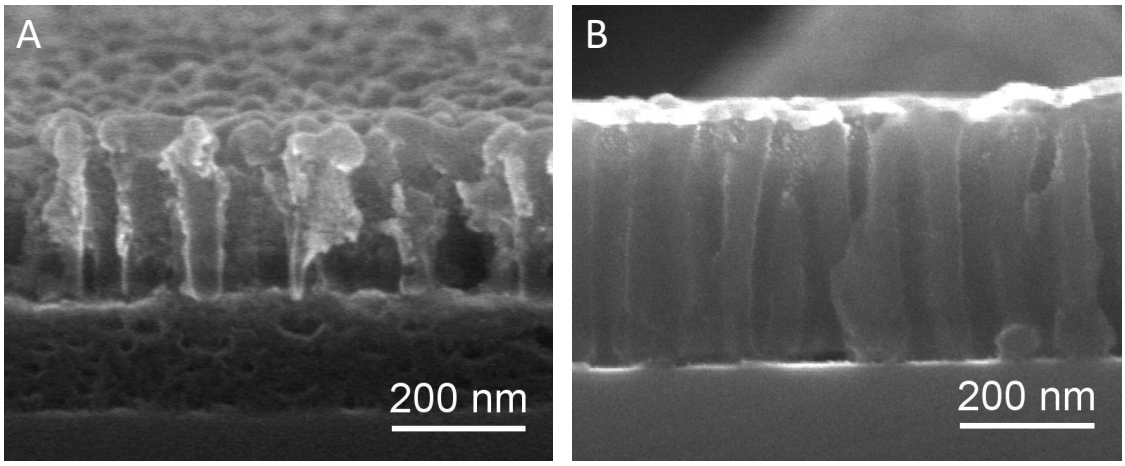

Figure 5.8 Cross-section FESEM images of AAO membrane on Al/Si with and excess of anodization time, A), and a membrane with an anodization time adjusted for the Al thickness B).

Once the peeling off and catalyst shape modification problems were addressed, the pattern MACE process finally led to the SiNWs formation. As a result, a dense forest of SiNWs with homogenous diameters could be obtained, **figure 5.9A**. The shape of the pattern during the etching is well kept and properly transferred to the SiNWs, **figure 5.9B**. However, it was observed that the diameter of the obtained SiNWs was a bit lower than expected. Several membranes were measured as-produced and the diameters of the SiNWs grown with those membranes were analized by FESEM, **figure 5.9C**. Through the mentioned analysis it was obtained an average diameter reduction of around 15 nm. This diameter reduction is consistent with the mechanics of the MACE process, as the catalyst has an area of effect of a few nanometers where the etching is produced[13]. This effect, overlapped with the closure produced by the catalyst deposition, can explain the diameter reduction. As a consequence, the diameter difference between the pores of the AAO and the SiNWs, is intrinsic of the method and has to be considered when selecting the diameter of the pattern.

Similarly to the MACE processes in other chapters, the length of the SiNWs is easily controlled through the duration of the etching. However, as the catalyst and solution molar ratios are different from the ones saw in the first chapter, the etching rate would be also

different. For this reason, it is necessary to investigate again the etching rate of this new system by the analysis of cross-section FESEM images, **figure 5.9D**. The study was performed with solutions at room temperature and with a catalyst thickness of 15 nm. It is worthy to mention that the catalyst thickness has its importance, because it has been proved to affect the etching rates[110].

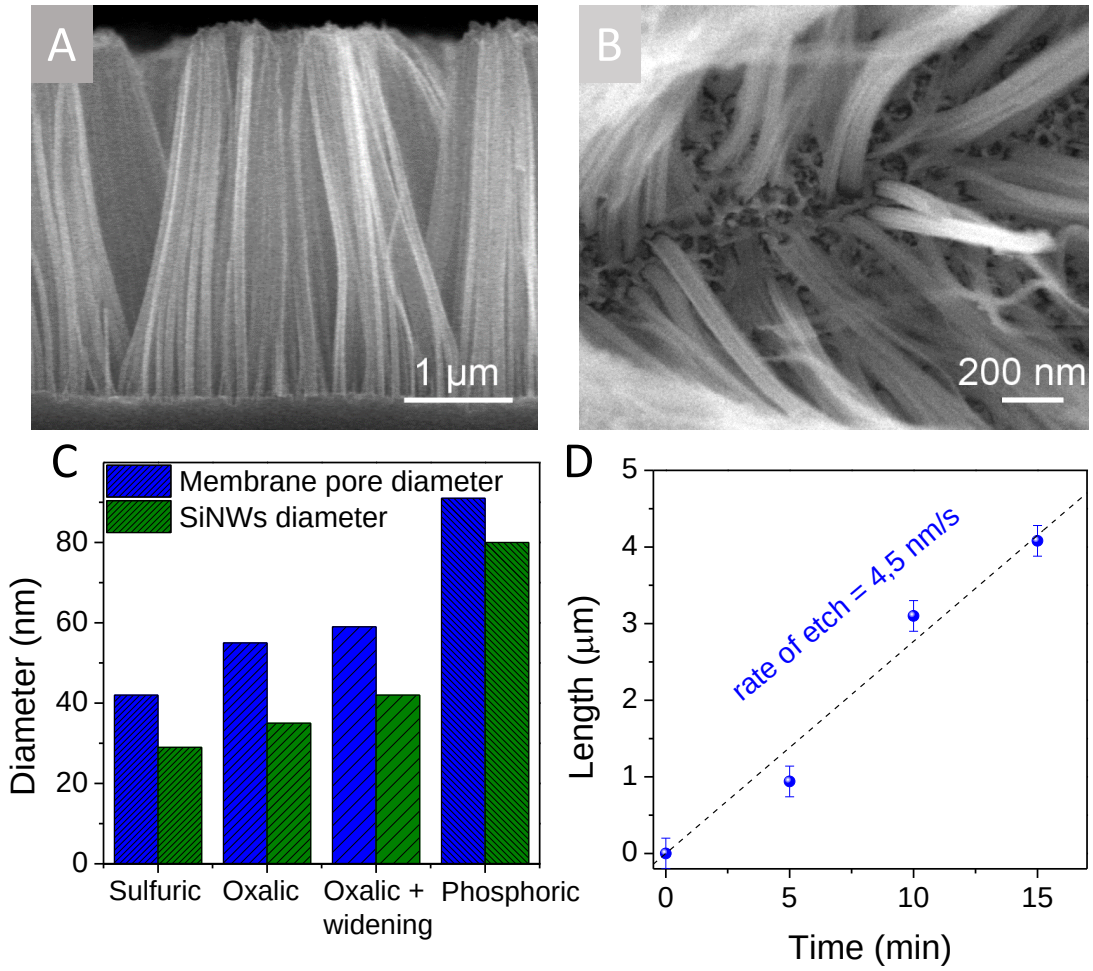

Figure 5.9 A) cross-section and B) top-view FESEM images of SiNWs grown with AAO patterns. C) diameter reduction of the SiNWs for different AAO. D) Length of the SiNWs vs etching time.

In order to check if the modifications of the MACE process (change of the catalyst and molar ratios) involved changes on the surface morphology of the SiNWs, nanowires grown through the patterned MACE were analyzed by TEM. By this technique it was corroborated

the good diameter homogeneity of the obtained SiNWs, **figure 5.10A**, and, also, that the surface oxide around crystalline core was as thin or even thinner than in the common MACE SiNWs (~3nm vs ~5 nm), **figure 5.10A** inset. This important result indicates that in this AAO/Si system, the good properties of the SiNWs are kept untouched.

After the exhaustive analysis performed, the diameter, separation and length of the SiNWs could be precisely controlled. Therefore, it was tested if the improved separation of the nanowires could facilitate the deposition of layers on top of the SiNWs. In order to do so, Al was simultaneously deposited on top of standard SiNWs, **figure 5.10B**, and on top SiNWs growth by AAO pattern, **figure 5.10C**. In this images it can be clearly seen how the small separation of the standard SiNWs leads to a very inhomogeneous covering of the surface, coating only the tips and some exposed surfaces of the SiNWs. On the other hand, the patterned SiNWs have all their surface fully covered, even allowing the coverage of their bases and the substrate. This result has an extraordinary transcendence for the passivation of SiNWs, which is, right now, probably the biggest drawback that SiNWs have for their application in solar cells. Moreover, this result, as well as the high controllability of each aspect of the SiNWs that the method offers, could be beneficial to many other applications.

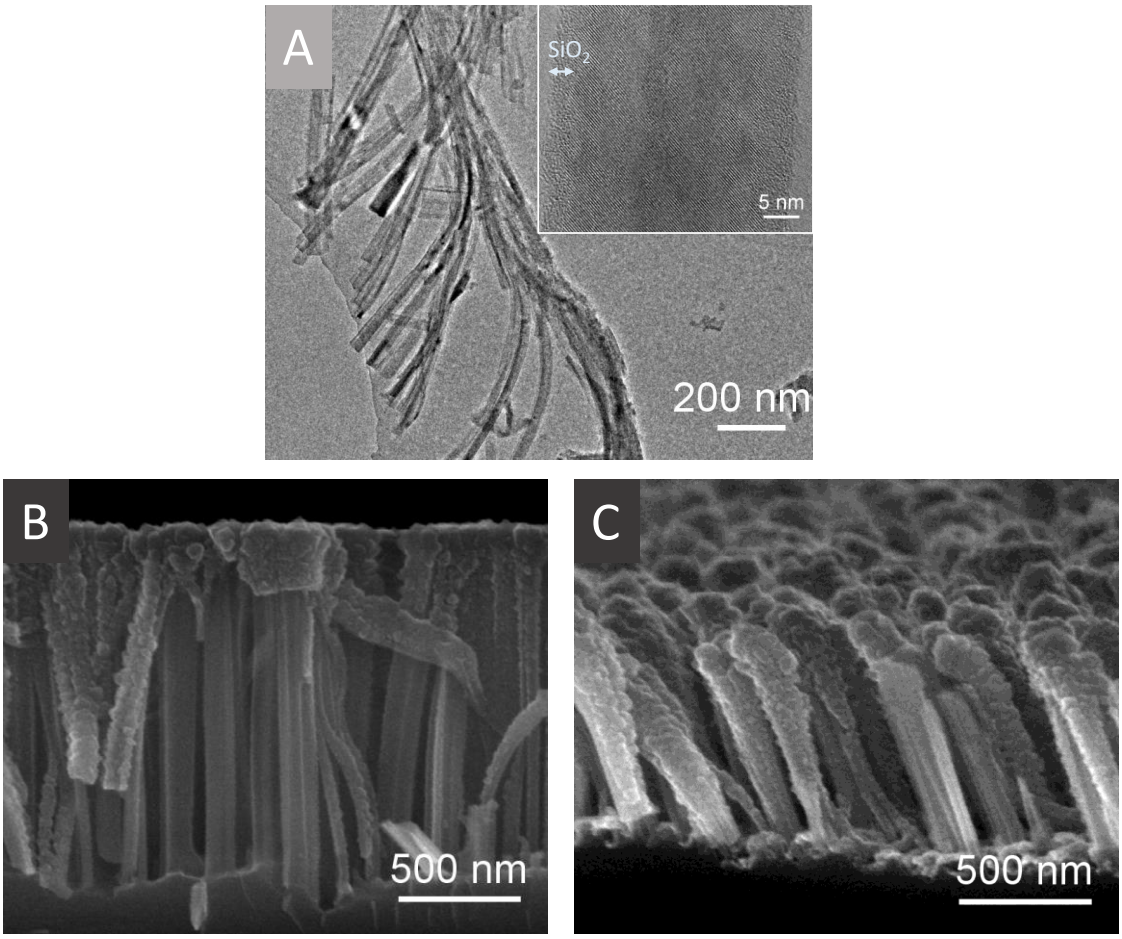

Figure 5.10 A) TEM image a bundle of SiNWs grown through AAO pattern and inset a zoom of a single SiNW with a very thin oxide layer. B) Standard SiNWs with a coverage of 150 nm of Al. C) SiNWs grown with AAO pattern with a coverage of 150 nm of Al.

5.4 Conclusions

In this chapter AAO membranes with controlled characteristics has been successfully grown directly on top of Si substrates. The influence of all the anodization parameters on the resulting membrane have been addressed, pointing out noticeable differences with the process on Al substrates. Among this differences, it can be highlighted the change in the 10% porosity rule, which in this studied system lead to a porosity of ~40%. Furthermore, it is noticeable the change observed in the empiric relation between interpore distances and anodization voltage.

Once the control of the membrane parameters was completely studied, the patterned MACE was applied to the growth of the SiNWs. Ag and Au were tested as catalyst, and from them, Au was the only one capable to transfer the patterns to the Si, generating SiNWs. The SiNWs arrays grown with patterns allow the deposition of subsequent films obtaining an extremely good coverage of the surface, which is not possible to achieve by using the standard MACE.

In this chapter, it has been proven the versatility of the SiNWs growth with patterns. This method permits the generation of crystalline SiNWs with selected diameters and controlled separation. Moreover, the objective of the chapter has been achieved, as the developed method had allowed the deposition of subsequent films.

Chapter 6:

Crystalline SiNWs grown by MACE for lithium ion batteries

6.1 Introduction

Along this chapter the study is focused on the application of the MACE SiNWs in lithium ion batteries (LIBs). In order to make the MACE a cost effective method for the obtainment of SiNWs for this application, the synthesis procedure has been modified. By this enhanced MACE process, the etching of the whole c-Si substrate thickness was achieved, transforming the full thickness into SiNWs. The SiNWs have been fully characterized taking into account the battery application and paying special attention to the surface of the material.

The formation of the SiNWs based electrodes was approached by two different ways. The first one, was done by the deposition of the material mixed as a paste on a conductive Cu foil. This method is the most well known and most common approach for the formation of electrodes both in research and industry. Among the advantages, it is found a great versatility, it can be used with any material, and the scalability, the same procedure applied in the research for a few electrodes, is applied in the industry for a large amount of material.

The second method is an adaptation of a practice that is lately gaining importance in the lithium ion anode research; the formation of a free-standing electrode containing the active material[111]. In this type of electrode, the Si material is embedded in a carbon based matrix, in

this case CNTs, without the presence of a Cu substrate. This method significantly enhances the conductivity while keeping a very good mechanical strength[97,111,112]. Also, the absence of binder[111] helps to improve the electrical contact with the material and allows the use of thermal treatments to the anode. Additionally, the CNTs also produce a strain release effect on silicon[113] which could potentially boost the cycling performance of the anodes by reducing the pulverization.

Both type of electrodes were systematically studied by electrochemical potential spectroscopy[114] and a deep description of their electrochemical performance is included. Moreover, other Si nanomaterials were tested in in order to compare the performance of our MACE SiNWs to current studies on Si-base anodes.

6.2 Experimental

6.2.1 SiNWs synthesis

The SiNWs were synthesized through MACE on p-type (100) monocrystalline (1-10 Ωcm, boron-doped, 270 μm) and n-type (100) monocrystalline (1-10 Ωcm, phosphorus-doped, 270 μm) silicon wafers provided by El-CAT. One side of the wafer was polished whereas the opposite side was unpolished.

The standard two step MACE procedure, described in chapter 1, was applied, with a molar ratio between HF and H_2O_2 of ε=24. Samples were immersed into the $AgNO_3$/HF bath for a period of 2 minutes, in order to obtain a good coverage of Ag nanoparticles on the surface with an excess of Ag. When using silver as catalyst, is critical to deposit a thick layer of Ag nanoparticles, especially if an entire etch on the thickness of the wafer is going to take place. This is because a fact already discussed in the previous chapter, the relative low electrochemical potential of the Ag produces the dilution of the nanoparticles in HF/H_2O_2 solutions. If the initial amount of nanoparticles is not enough, the longitudinal etch along

the entire wafer thickness is not completed and the etching depth across the wafer is not uniform.

In order to adjust the duration of the HF/H_2O_2 bath to achieve a full thickness etching of the wafer, a detailed study was performed. For this study, a longitudinal piece of Si wafer was subjected to a progressive MACE process. At different times after the process start, a small piece of sample was taken out from the acid solution, leaving the rest of the sample inside the solution. Every 30 minutes the etching solution was changed in order to avoid the slowing of the process due to a shortage of reactants. As can be observed in **figure 6.1**, both sides of the wafer were simultaneously etched. At low times (up to 150 min) it can be detected two different behaviors depending on the wafer surface morphology. While the etching of the polished side of the wafer (top side of the images from **figure 6.1**) evolves from a clean and organized front, the etching of the non-polished side presents some irregularities, mainly caused by the surface roughness of that side of the wafer. Despite the etching rate is larger at the non-polished side at the beginning, at intermediate stages (around 200 minutes), the evolution of both sides seems to be very similar. The faster etch found at the beginning can be related to the specific action of the silver nanoparticles on preferential sites of the non-polished side. After 300 minutes both silicon etch fronts reach contact.

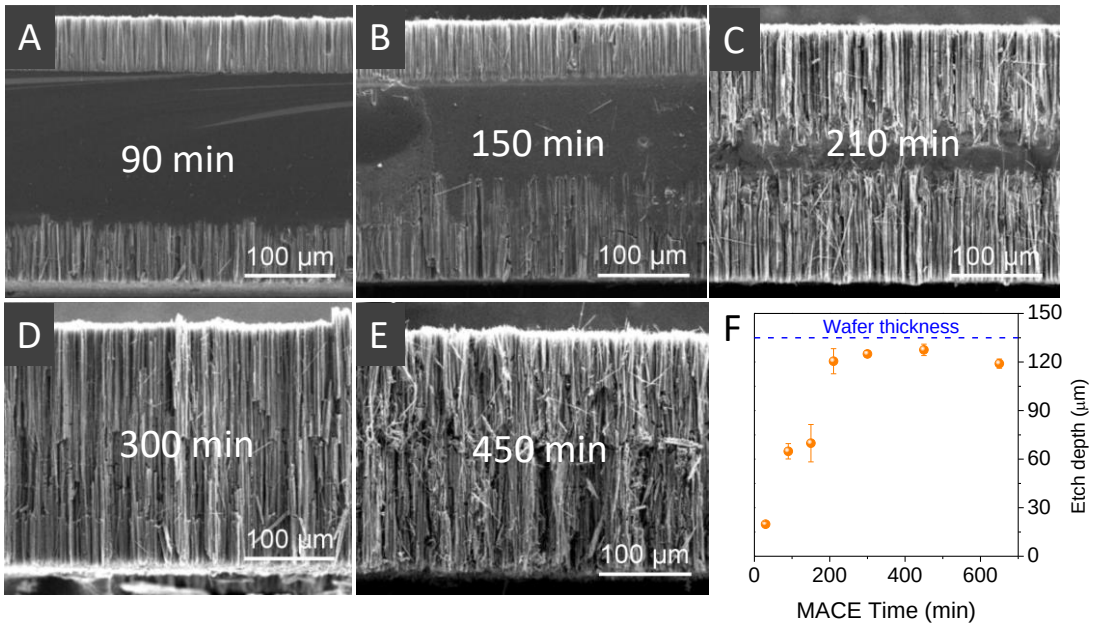

Figure 6.1 A) to E), cross-sectional FESEM images of a Si wafer after the displayed MACE times. F) Etching depth as a function of time.

The etching fronts advance linearly with time at a rate of 10 nm/s, **figure 6.1F**, being this rate consistent with the rates obtained in the first chapter, as the temperature of the bath was kept constant at 30ºC. Due to the thickness of the wafer, the etching saturates when fronts reach in contact at approximately 130 µm. If the etching time is prolonged, **figure 6.1E-F**, the total thickness is slightly reduced. This result indicates that the uppermost parts of the wafer is beginning to dissolve, losing some of the starting material and provoking nanowires tapering at the tip. Thus, this study establishes that 300 minutes is the appropriate time to etch the whole thickness of the wafer, in the standard conditions of reagents of this work. Moreover, it concludes that the etching time should not be extended beyond eight hours (480 minutes) to avoid consuming material.

Once the process is completed, the full etched wafer is rinsed in DI water for cleaning. After this step, the samples were stored in DI water, or ETOH, and sonicated until no solid pieces were visible.

6.2.2 Single nanowire device for electrical characterization

In order to investigate the electrical properties of the SiNWs without the interference of a substrate, single nanowire devices were fabricated. First, the dispersed SiNWs were deposited over an oxidized silicon substrate pre-patterned with pairs of conductive AZO:Al electrodes fabricated by optical lithography. The spacing between electrodes ranged from 4 to 8 microns. The nanowires were individually aligned in the gap between each pair of electrodes by AC dielectrophoresis with an amplitude of 20V and a frequency of 100 KHz. Under these parameters, the method allows to obtain a single nanowire contacting both electrodes, **figure 6.2A**, and enabling its electrical characterization. To improve the contact between the electrodes and each nanowire, aluminum was deposited atop the tips of the nanowire by lithography and lift-off without pre-treatment acids. This insured that the chemical properties of the SiNWs obtained from the MACE process remained unmodified. A scheme of the single nanowire device is also shown in **figure 6.2B**.

Once fabricated, the chips with the devices were wire bonding and encapsulated in a Transistor Outline (TO-5) header to minimize the background electrical noise whose level was as low as 0.1 pA in the electrical setup.

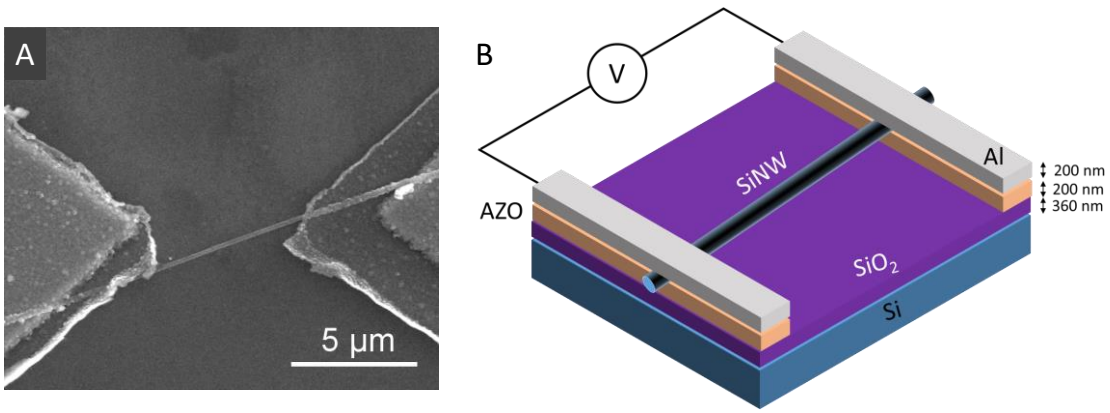

Figure 6.2 A) FESEM image of a finished single nanowire device. B) Scheme of the single nanowire device.

6.2.3 On-foil electrodes and batteries assembly

The first synthesis method used for the SiNWs based electrodes was the on-foil deposition of the SiNWs, scheme 4. Firstly, the active material, in this case the SiNWs and/or other Si nanomaterials, were mixed with the additives. The used additives were Carbon Black (Timical Super C65, MTI Corp), which enhances the conductivity of the material forming a conductive matrix, and Li-PAA (3g PAA (35%)+0,6 g LiOH+ 78,9 g DH_2O prepared as described by Eberma *et al* [115]), which provides adhesion, porosity and hardness to the Si electrodes. The mentioned mixture, usually called slurry, was performed in a weight proportion of 70% of Si material, 20% the carbon black and 10% of Li-PAA. Previous to the mixture step, the weight of the SiNWs was obtained by drying the SiNWs solution in an oven at 80ºC for a whole night. The dried SiNWs were redispersed in the desired concentration and used for the slurry formation. Once the weighting of each component was done, the mixing was accomplished by a manual milling in an Agatha mortar until a homogenous viscous fluid was obtained. Then, the slurry was applied on a Cu film (MTI Corporation 99.99%, 9 μm) by a micrometer adjustable film applicator (Doctor Blade), which allow the thickness control of the deposited layer by a gauged blade. The thickness of the layer was selected in the range between 100 or 150 μm, which was also checked by a contact profilometer (Dekat 6M, Veeco Instruments). Afterwards, the Cu film with the wet slurry was dried in an oven at 100ºC in vacuum for 5 hours. Once dried, 12 mm diameter round shaped electrodes were cut with an EL-CUT (provided by EL-CELL) device.

Finally, the electrodes were introduced into a glove box (GP Campus, Jacomex) filled with Ar and the assembly of the batteries was performed. The LIBs were assembled in a half-cell configuration with a counter electrode of pure Li. This configuration is usually used for the characterization of novel materials, allowing the study of their electrochemical properties without the interference of the counter electrode compound. The use of metal Li as counter

electrode implicates a high negative reduction potential of the Li^+/Li, therefore, every working electrode, even the ones designed for anode, in the half-cell configuration have to act as positive electrode[111].

The assembled batteries were encapsulated in CR2032-coin cells following the diagram presented in **scheme 6.1**. The electrolyte used was a solution of 1M $LiPF_6$ in ethylene carbonate and diethyl carbonate (EC:DMC, 1:1 v/v supplied by Sigma-Aldrich), and as separator, a glass microfiber filter disk (Whatman grade GF/B, thickness 0.68 mm) of 16 mm diameter. Once assembled, the batteries where left at least 2 hours to homogenize previously to be measured.

The electrochemical characterization consisted on galvanostatic cycling of the batteries. The first lithiation/delithiation profiles for the samples were carried out at a constant current density of 0.5 A/g. The subsequent cycles were performed at 2 A/g, except in those cases that is explicitly denoted. The specific capacities of each electrode were calculated based on the active material mass.

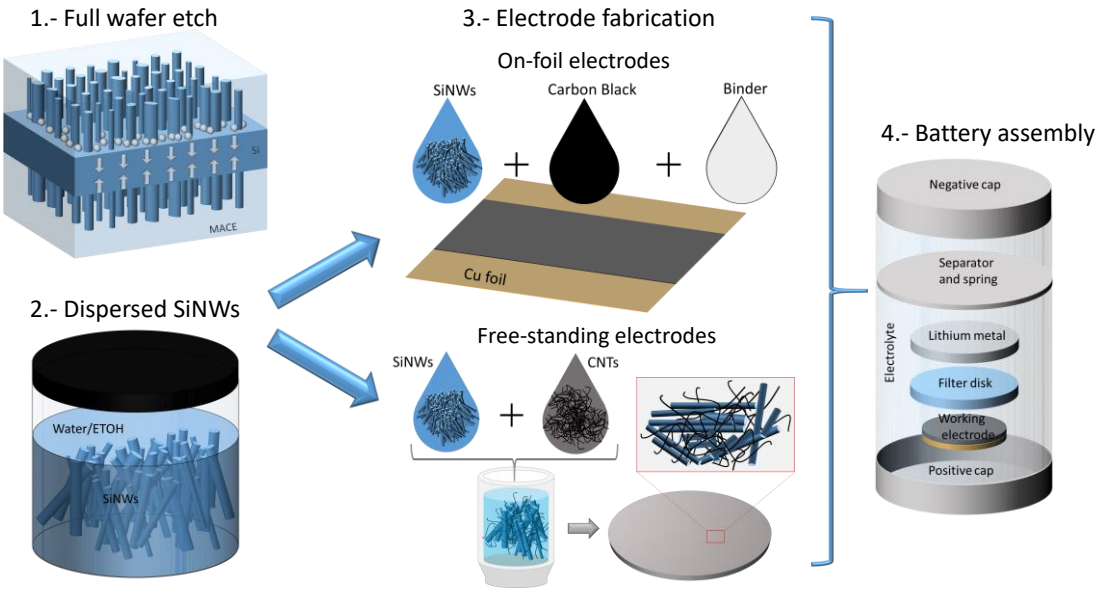

Scheme 6.1 Diagram of the two presented methods of obtaining SiNWs based electrodes.

6.2.4 Free-standing SiNWs/CNTs electrodes formation

The fabrication of free-standing electrodes was conducted by the percolation of a solution composed by a mixture of SiNWs and CNTs, **scheme 6.1**. The CNTs were commercial (TUBALL BATT without surfactants, water based dispersed at 2%). The mixture of the SiNWs and CNTs was performed in a ratio ranging from the 5% to 30% in weight of dried CNTs. After mixing, the dispersion was sonicated for 10 min at room temperature, obtaining a good entanglement between the CNTs and SiNWs, avoiding the formation of CNTs or SiNWs aggregates. After the sonication process, the homogenized mixture was filtrated in a vacuum filtration system on a CELGARD membrane (Celgard 3501, PP coated, USA). In order to avoid any segregation or the formation of aggregates of the CNTs or SiNWs, the filtration took place right after the sonication process and with a low amount of solvent. A low amount of solvent is recommended because if the percolation process takes too long, the SiNWs tend to precipitate forming an electrode with a high concentration of SiNWs on one side and a lack of them on the other. This inhomogeneity can highly affect the performance of the battery due to the discontinuity of the conductive matrix. The amount of material used in the percolation was fixed to a proportion of 1 mg/cm^2 of the area of the filtration system. This way the superficial density could be maintained between experiments.

Subsequent to the percolation, the electrodes on top of the membrane were introduced into a desiccator for a whole night. When they are dry enough they automatically peel off from the filtering membrane, leaving a free-standing SiNWs/CNT electrode. In order to remove any solvent remains or impurities from the CNTs, they were subjected to a thermal treatment at 700ºC at a pressure of 10^{-2} bar and Ar flow for 4 hours. Further details of the thermal treatment are displayed in **scheme 6.2**.

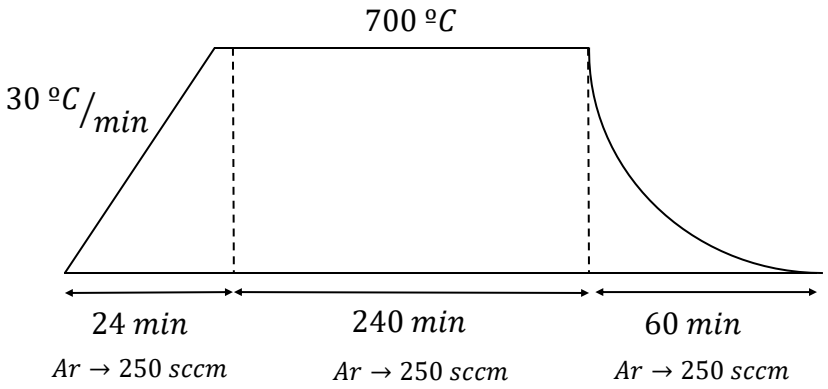

Scheme 6.2 Thermal treatment applied to the SiNWs/SWCNTs electrodes in a tubular oven

Successive to the thermal treatment, the electrodes were cut in the desired size/weight and introduced into the glove box for the battery assembly. The battery assembly was performed as described previously and according to the **scheme 6.1**.

6.3 Results and discussion

6.3.1 Characterization of the full etched SiNWs

As it has been addressed in the introduction, the performance of anode materials for LIBs is affected by many factors[97], being conductivity one of them. Low conductivity values on the electrodes could lead to high energy losses and overheat. Due to the fact that many of the emerging materials for the LIBs have low conductivity values, it is necessary to implement higher amounts of conductive additive[116]. Its disadvantage is that the percentage of active material in the electrode is reduced. Also, for some nanomaterials with bad conductive properties, the common additives are not enough. In these cases, surface modification and inclusion of other conductive nanomaterials are necessary to achieve good conductivities for the operation of the battery[117,118].

On the basis of the exposed arguments, it becomes necessary to investigate the conductive properties of the synthesized SiNWs in order to apply them into LIBs. On this purpose, the

I-V curves of several SiNWs with different diameters were measured using the single nanowire device method described in the experimental section, **figure 6.2**. In the I-V measurements it was observed that the devices had different electrical behavior as a function of the nanowire diameter. For large diameters, between 400 and 600 nm, the I-V characteristics obtained were as the one shown in **figure 6.3A**. Those I-V characteristic shown a linear behavior with a large resistance. The value of the resistance was significantly higher than that expected from the resistivity of the wafer and the SiNWs dimensions. Indeed, the expected resistance was in the order of MΩ but the obtained resistance was around 5 TΩ. Thus, the most feasible explanation of these values is the presence of a thick insulating oxide layer in the surface of the SiNW. The TEM analysis, already shown in the first chapter, for the on-wafer SiNWs did not revealed an oxide layer thick enough to cause this high resistivity. Therefore, the full-etching procedure might be changing the surface morphology in an unexpected way. In order to investigate this effect, TEM was performed in the full-etched SiNWs. It was found that for nanowires with diameters around 500 nm, the oxide layer was way thicker than the one previously observed, **figure 6.3B**, being on average 15 nm. The obtained oxide thickness could indeed be responsible of the high resistivity, limiting the transport through the nanowire and producing a large resistance in comparison to the resistance associated to the conduction through the crystalline core[1].

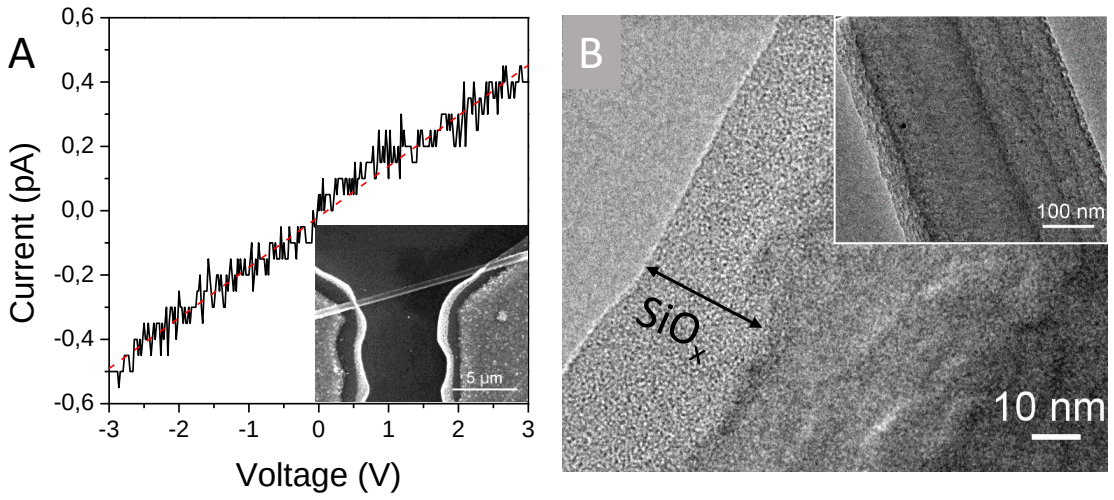

Figure 6.3 On A) I-V characteristics of a SiNW of 500 nm diameter measured by the formation of a single nanowire device which can be seen in the inset. B) TEM images of 500 nm diameter SiNWs where it can be seen a thick SiO_x layer on the surface.

When thinner SiNWs, diameters around 300 nm, were tested, the I-V characteristics were considerably different to the ones of bigger diameters, **figure 6.4**. In this medium sized nanowires, the I-V curve have a behavior typically shown by two opposing diodes. Besides, the current reached at 3 V was larger than the shown by the thicker NW device. By analyzing in TEM the medium sized SiNWs, it was observed notable thinner oxide thicknesses, **figure 6.4B**, of around 7 nm. Taking into account the thickness reduction of the oxide layer, one may conclude that the different electrical behavior is caused by a thinner oxide layer. In fact, the thin oxide layer have the appropriate thickness to lead to the formation of two opposing MIS structures on each contact area, what would explain the I-V characteristics[1].

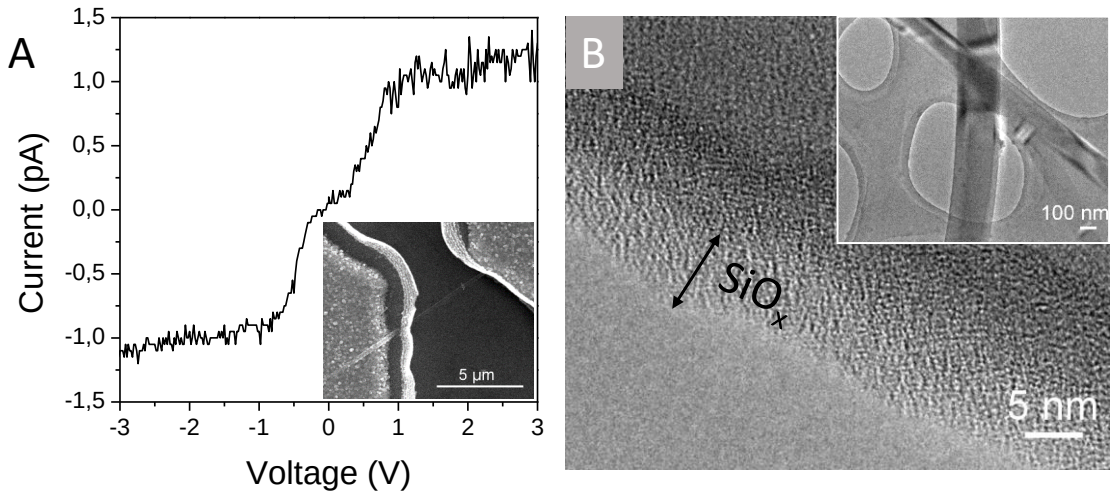

Figure 6.4 A) I-V characteristic of medium sized SiNW obtained from a single nanowire device. B) TEM images of medium sized SiNWs with an oxide thickness around 7 nm.

For SiNWs with small diameters, lower than 150 nm, the I-V characteristic was found to be as the one shown in **figure 6.5A**. The I-V characteristic exhibit a very high current level compared to thicker nanowires and asymmetric reverse and forward characteristics. Also, TEM imaging revealed the presence of an extremely thin oxide layer, **figure 6.5B**, being in average close to 4 nm. The high current seems to be in good agreement with the findings of an extremely thin surface oxide layer, which produces a scenario that resembles to the one found in metal-semiconductor Schottky junctions[1]. In this scenario, the oxide is so thin that when a voltage is applied, electrons are capable to tunnel through the oxide barrier, not highly affecting the conduction. The asymmetrical behavior observed could be related to the different contact area between the NW and the electrodes. As shown in the FESEM image inset in **figure 6.5A**, the contact area is almost five times larger at the right electrode, an asymmetry caused by the dielectrophoresis alignment process.

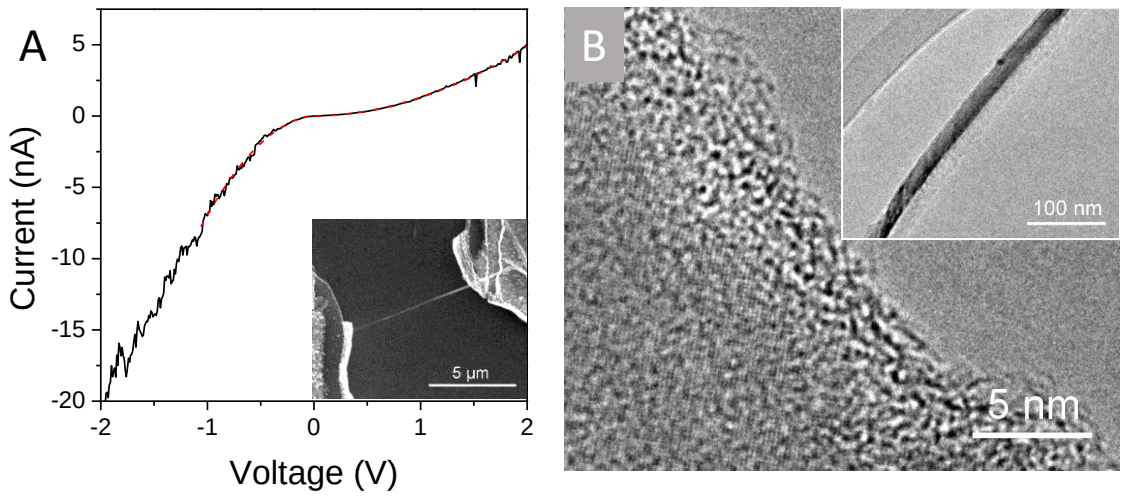

Figure 6.5 A) I-V characteristic of small SiNW obtained from a single nanowire device. B) TEM images a small SiNW showing an extremely low amount of oxide in the surface.

On the premises of the above discussed, a systematic TEM study of the SiNWs was conducted in order to endorse the size dependent oxide thickness. In this study, numerous samples with the same etching processes were analyzed by TEM. To avoid any extra oxide formation, all the samples were dispersed and deposited right before TEM measurements. The measurements of the oxide layer thicknesses in dependence of the diameter are summarized in **figure 6.6A**, presenting the results divided into four ranges of diameters. The trend shown by this results clearly confirms the observations made along the whole chapter, as the diameter of the nanowire grows, the wrapping oxide around it grows too. Moreover, the results of the electrical characterization, outlined in **figure 6.6B**, clearly match with this observations, as the different electrical behaviors seem to be determined by the change of the oxide thickness. From a practical viewpoint, this behavior reveals the need of optimizing the MACE process to adapt the SiNW structure and morphology to the application requirements.

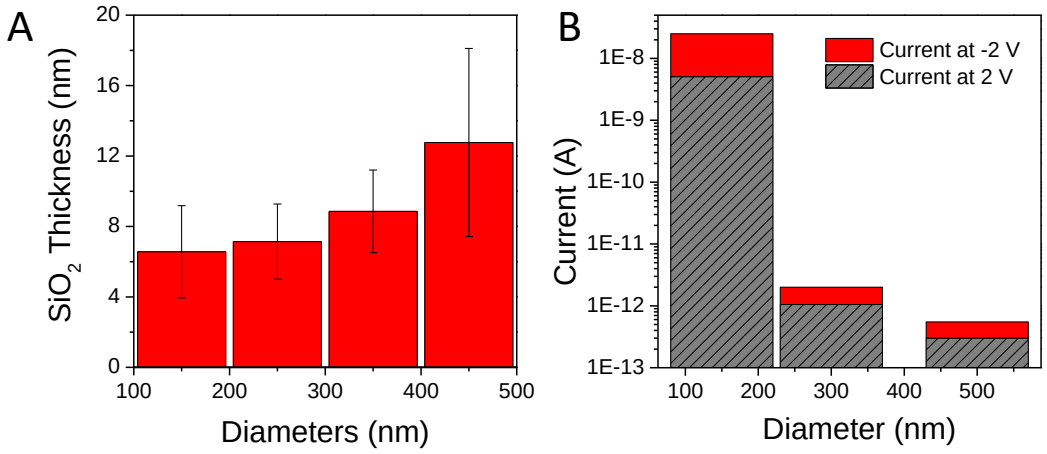

Figure 6.6 A) Silicon oxide thickness as a function of the diameter of the SiNWs from TEM observations. B) currents at 2V and – 2V obtained by the single nanowire devices are displayed as a function of the SiNW diameter.

After these results, it can be hypothesized that the difference between the oxide thicknesses has its origin in the growth mechanism. In MACE, the dissolution of Si is a complex process produced through three different mechanisms in presence of Ag nanoparticles NPs[13].

The first one is the direct Si dissolution in tetravalent state[119]:

$$Si + 4h^+ + 4HF \rightarrow SiF_4 + 4H^+$$ **Equation 6.1**

$$SiF_4 + 2HF \rightarrow H_2SiF_6$$ **Equation 6.2**

The second one, the direct Si dissolution in divalent state[120]:

$$Si + 4HF_2^- + 2h^+ \rightarrow SiF_6^{2-} + 2HF + H_2$$ **Equation 6.3**

The third one, the Si dissolution through oxide formation[120]:

$$Si + 2H_2O + 4h^+ \rightarrow SiO_2 + 4H^+$$ **Equation 6.4**

$$SiO_2 + 6HF \rightarrow H_2SiF_6 + 2H_2O$$ **Equation 6.5**

In principle, all the reactions are possible and can occurs at the same time in the Ag/Si interface. However, since the smaller nanowires grow in areas highly covered by Ag nanoparticles (NPs), while bigger SiNWs are produced in regions where the density of catalyst NPs is lower, **figure 6.7A-B**, the reactions that takes place in each case might be different.

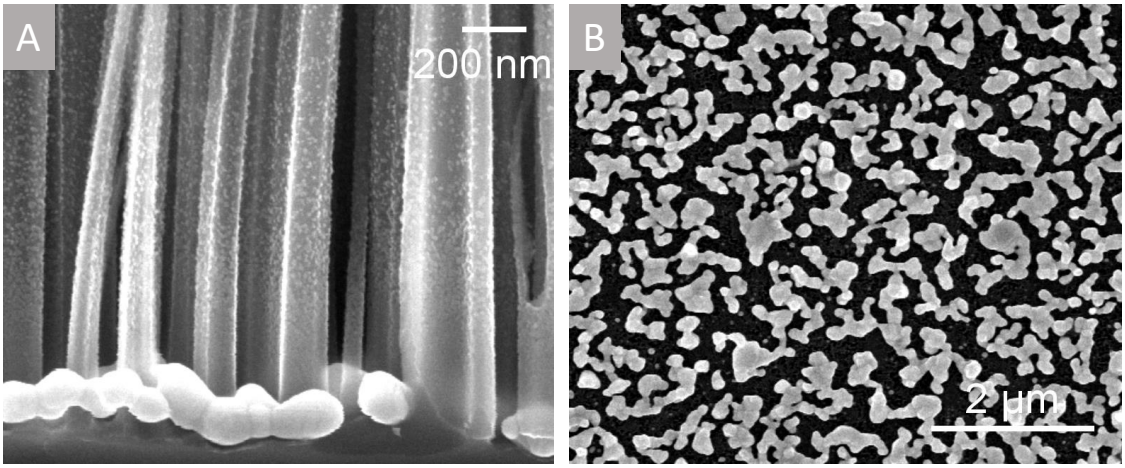

Figure 6.7 A) Cross-section FESEM image of Ag NPs around SiNWs of different diameter. B) Ag NPs distribution on the surface of the Si. The wider spaces between Ag NPs produces bigger SiNWs, while the closer ones, thinner SiNWs.

In the case of small SiNWs, the high density of Ag NPs in the surroundings of the attack area might hinder the diffusion of all the reactants required for the dissolution through the oxide formation. This could make the etching of thin SiNWs more likely to occur from the direct dissolutions (**Equation 6.1, 6.2, 6.3**). As a result, the oxide formed in the walls of those SiNWs may be thinner.

On the other hand, for bigger nanowires, we might have the opposite case. The wider space between Ag NPs could preferentially enable the etching through the oxide formation, leading to a thicker oxide thickness in the walls of the nanowire.

This oxide, formed during the growth of the nanowires, is preserved until the end of the MACE process. However, as the solution contains HF, the oxide formed in the walls of the nanowires should be removed. Thereby, it seems that without the catalytic action of the Ag NPs, equation 6.4 and 6.5 reach an equilibrium with a very low etching rate, keeping the oxide thickness constant but reducing the Si core. This could explain the reduction of length of the SiNWs once the full thickness of the wafer is consumed, an effect observed in **figure 6.1F**. In that case, the lateral etch through the walls of the nanowires is only noticed in the uppermost parts of the SiNWs after long exposition times.

The above exposed has a great interest for the application of the SiNWs in any kind of device, because the observed SiO_2 barriers have proven to highly affect the conductive properties of the SiNWs. Moreover, focusing on the application of the synthetized SiNWs in LIBs, the obtained results are very important due to the high influence that the oxide thickness has in the electrochemical performance of the batteries[121]. *McDowell et al* observed a progressive reduction of the electrochemical performance of c-SiNWs wrapped by SiO_2, with the increase of the oxide thickness. In their studies, they found that the oxide layer induce a compressive stress in the c-Si which reduce the equilibrium concentration of Li in the lithiated nanowire[121], leading to a lower capacity of the material.

6.3.2 On-foil electrodes

According to the results from the previous section, the thick oxide present in the as-etched SiNWs could hinder the lithiation capacity. Therefore, an extra step was added to the experimental procedure of the SiNWs synthesis: an oxide removal. Once the wafer was completely etched, the still entangled as synthetized nanowires were dipped into an HF 5% solution for 3 minutes. After this step, the SiNWs were normally sonicated and disperse in the selected solvent. The SiNWs with and without the HF cleaning, were deposited on a HOPG substrate and analyzed by XPS to obtain the oxide content. The SiNWs without the

HF treatment, **figure 6.8A,** shows a notable presence of SiO_2 and a shift of 1.4 eV in all Si peaks. Very interestingly, this shift is not observed in the C peaks, inset of **figure 6.8A**. This behavior comes from the fact that the carbon peak arises from the HOPG, which is conductive and does not get charged from the incident X-rays. On the other hand, the as-synthesized SiNWs, due to their oxide thickness and poor conductivity, get charged, resulting in a shift on binding energies. The mentioned carbon peak can be univocally identified to be from the HOPG and not from the adventitious carbon. This can be stated from the asymmetric tale of the C peak towards higher energies, **figure 6.8A** inset, which is a feature of the sp^2 carbon, usually found in HOPG or graphene.

In **figure 6.8B** it can be found the XPS spectrum of HF treated SiNWs, which show a much smaller SiO_2 peak and none energy shifting, indicating a good conduction to the substrate.

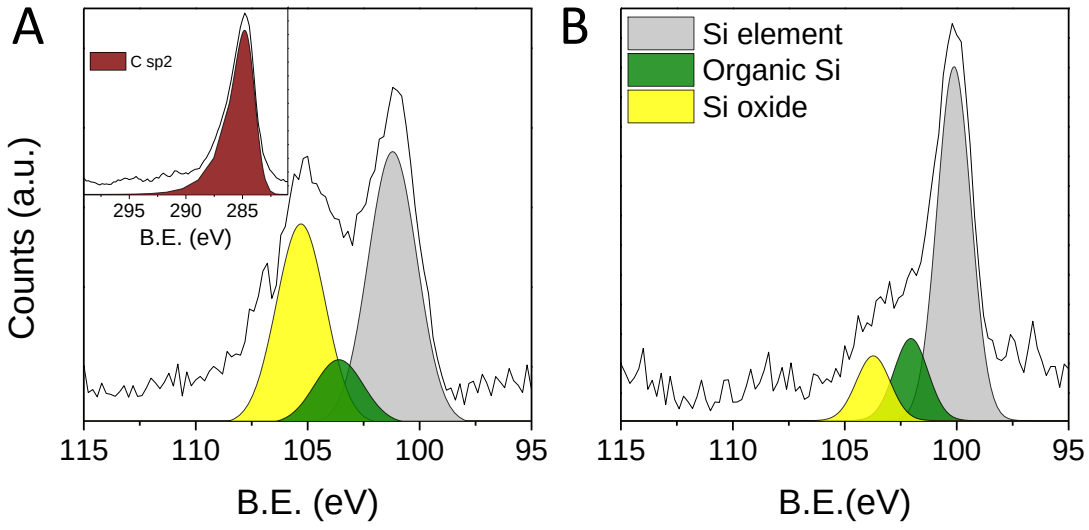

Figure 6.8 XPS of the Si 2p region of SiNWs produced by a full-etching MACE A), and after an extra HF post-processing treatment, B). The inset in A) corresponds to the C s1 region.

To further test the usefulness of the oxide removal, batteries were assembled using the SiNWs with and without the HF treatment. For analysis the batteries were subjected to galvanostatic cycling. Electrochemical potential spectroscopy data was extracted and

displayed in **figure 6.9**. Voltage profiles (VP) (right column in **figure 6.9**) and differential capacity (DC) curves (middle and left column in **figure 6.9**) were represented for both HF and non HF treated SiNWs electrodes.

During the first lithiation (**figure 6.9A-C**) both electrodes show a small peak in the DC curves around 0.9 V, which is also observed in the VP as a slight change of slope. This peak is identified as *"1"* in **figures 6.9A-C** (in **figures 6.9A-B** is also shown as an inset) and can be attributed to the formation of the SEI†[122]. Interestingly, this peak is bigger in the sample treated with HF (**figure 6.9B**), meaning a higher irreversible capacity due to the SEI in the less oxidized sample. This behavior is corroborated in the VP on **figure 6.9C**, where it can be seen a bigger change of slope in the HF treated sample. This higher slope, results on reaching the ~100 mV plateau at higher capacities, meaning that the accumulated capacity until that point is irreversible capacity due to the SEI. This result is consistent with the literature observations, [123] where it is concluded that SiO_2 may suppress the formation of the SEI layer when compared to pristine Si.

At ~100 mV during the lithiation process, it is found a sharp peak in the DC curves of both samples, **figure 6.9A-B**. The mentioned peak is displayed in the VP as a constant plateau and is identified in **figures 6.9A-C** as "*2"*. Due to its shape and behavior in the VP, it can be assumed to be a two-phase lithium addition reaction[62]. It is well accepted that this reaction corresponds to the lithiation of the c-Si through the **equation 6.6**[124].

$$c-Si+xLi \rightarrow a-Li_xSi \qquad \textbf{Equation 6.6}$$

† The solid electrolyte interphase (SEI) is a passivating films that is formed in the surface of the anode due to the electrochemical reduction of solvent and salt of the electrolyte. Because the reduction of the electrolyte is produced by the interaction with the Li^+, it produces an irreversible capacity loss[123].

Through this reaction, all the c-Si is alloyed with the Li forming an amorphous compound. As more lithium is alloyed with the Si, the specific capacity of the battery grows, what is indicated by the length of the plateau *"2"* in the VP. In **figure 6.9C**, it can be observed that in the first lithiation, the HF treated samples show a much enhanced specific capacity than the samples without treatment, 2800 mAh/g compared to 2000 mAh/g.

As occurs with the lithiation, in delithiation, the different reactions that take place have characteristics peaks and slopes, both in the VP and DC curves. During the first delithiation, it is observed in both electrodes a sharp peak at ~480 mV marked as "3". This two-phase reaction is believed to be the delithiation of the crystalline $Li_{15}Si_4$ to form a-Si[124–126] **equation 6.7**.

$$Li_{15}Si_4 \rightarrow 4Si + 15Li \qquad \textbf{Equation 6.7}$$

The formation of the crystalline $Li_{15}Si_4$ is believed to take place in the lithiation around 50 mV, however the exact voltage at which this crystalline phase appears is not clear in the literature, as many groups have reported different voltages[124–126]. The difference of the reaction voltages between the literature could be governed by the different rate processes which are associated with many factors including Si size, crystallinity of Si particles, conductivity of electrode, applying current condition etc. The assumption that peak "3" comes from the delithiation of the $Li_{15}Si_4$ is either clear in the literature[122]. Previous reports have proven the formation of this phase in bulk Si [127] but, it is not certain if this also happen in SiNWs. The reason why is not clear, is that the formation of $Li_{15}Si_4$ seems to highly depend on the material strain, which is also related with the size of the particles[122,125]. Therefore, in small particles, the strain could not be enough to allow the $Li_{15}Si_4$ formation.

The $Li_{15}Si_4$ phase, despite of giving a very high theoretical specific capacity of 3579 mAh/g, is not desirable for Si based electrodes. The high internal stress that the two-phase reactions produce, can cause particle cracking and capacity loss[127]. In fact, the lithiation of Si anodes is

usually restricted to minimum voltages of 50 mV in order to avoid the formation of this crystalline phase.

In the delithiation, both samples present peak "3", which leads to a plateau in VP in **figure 6.9C**. Analogously as in lithiation, as longer is the plateau, larger is the amount of Li extracted, meaning a higher delithiation capacity. For the first cycle, the specific capacity values of both samples are 2100 mAh/g for HF treated sample and 1200 mAh/g for non HF-treated.

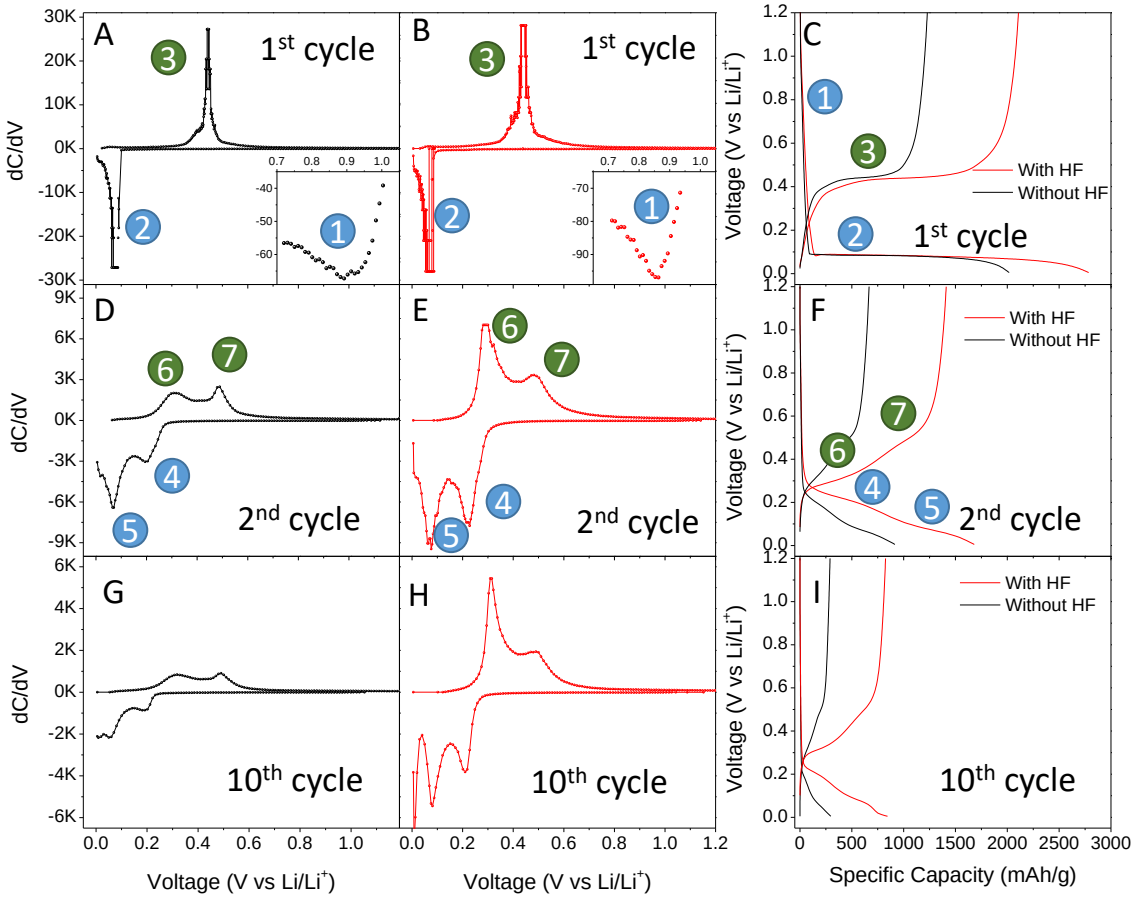

Figure 6.9 Electrochemical potential spectroscopy data of SiNWs with and without HF treatment. A)-C) graphs corresponds to the first cycle in the galvanostatic cycling, D)-F) to the second and G)-I) to the tenth. The differential capacity curves in the right side column corresponds to SiNWs without the HF treatment and the ones in the central column to the SiNWs with the HF. Graphs in the right side column are voltage profiles of both samples. Peaks marked in blue are due to lithiation and in green to delithiation.

The differences between the lithiation and delithiation capacities for each cycle, are a good indicator of the reversibility of the lithiation process. The evaluation of this reversibility is usually quantified by the coulombic efficiency (CE). The CE is obtained through the **equation 6.8,** where C_L is the lithiation capacity and C_D the delithiation capacity.

$$CE = \frac{C_D}{C_L} \cdot 100\% \qquad \textbf{Equation 6.8}$$

In most of the batteries, the coulombic efficiency is quite low in the first cycle due to irreversible parasitic reactions during the first lithiation. As lower is the CE value, higher is the capacity loss between the lithiation and delithiation. Among the irreversible processes that causes the capacity losses, are the formation of the SEI and loss of electrochemically active material due to pulverization[10]. In the case of our electrodes with SiNWs, with and without HF treatment, we obtain CE values for the first cycle of 78% and 60% respectively.

In the second lithiation/delithiation cycle (**figures 6.9D-F**) it is observed a significant change in the DC and VP curves for both samples. In the lithiation, peak "1" has been substituted by peaks "4" and "5", which are related with the alloying of lithium with a-Si. These two peaks are broad, indicating one-phase transition reactions, so no crystalline phase is involved. In the VPs, these peaks correspond to slope changes, leading to a more sloping curve without any straight plateau. The exact compounds formed in each reaction are not known, but they are known to be two consecutive incorporations of Li to amorphous Si-Li phases[62]. The reactions involved are displayed in **equation 6.9** and **6.10** for "4" and "5" respectively.

$$a-Si + xLi \underset{7}{\overset{4}{\rightleftharpoons}} a-Li_xSi \qquad \textbf{Equation 6.9}$$

$$a-Li_xSi + yLi \underset{6}{\overset{5}{\rightleftharpoons}} a-Li_{x+y}Si \qquad \textbf{Equation 6.10}$$

In the subsequent delithiation, one-phase transition reactions "6" and "7", are observed in both samples. These reactions are the reverse situation of "5" and "4" respectively, meaning

that the delithiation, as the lithiation, occurs between the a-Si and a-$Li_{x+y}Si$ in two steps. The VP in **figure 6.9F** indicates again a bigger lithiation/delithiation capacity for the SiNWs with HF treatment. The mentioned result can also be noticed in the DC curves, **figures 6.9D-E**, where the higher intensities shown by the treated HF SiNWs curves, reveal a larger amount of material activated during the lithiation/delithiation.

After 10 cycles, the shape and positions of the peaks in the DC curves remain unchanged, **figures 6.9G-H**, being only altered the intensities displayed. This behavior means that for both samples, the amount of active material which was involved in the electrochemical reaction has been reduced. The mentioned fact is also observed in the VP in **figure 6.9I,** where both capacities have been significantly reduced, but still being much higher in HF treated sample.

The specific capacity of both electrodes for the 50 first cycles, as well as the coulombic efficiency, are presented in **figure 6.10**. In this graph, it is observed a much better performance of the SiNWs treated with HF than the SiNWs without the treatment. The difference between capacities is almost a 75% in the first cycle (2100 mAh/g against 1220mAh/g) and it grows to 175% after 50 cycles (465mAh/g vs 168 mAh/g).

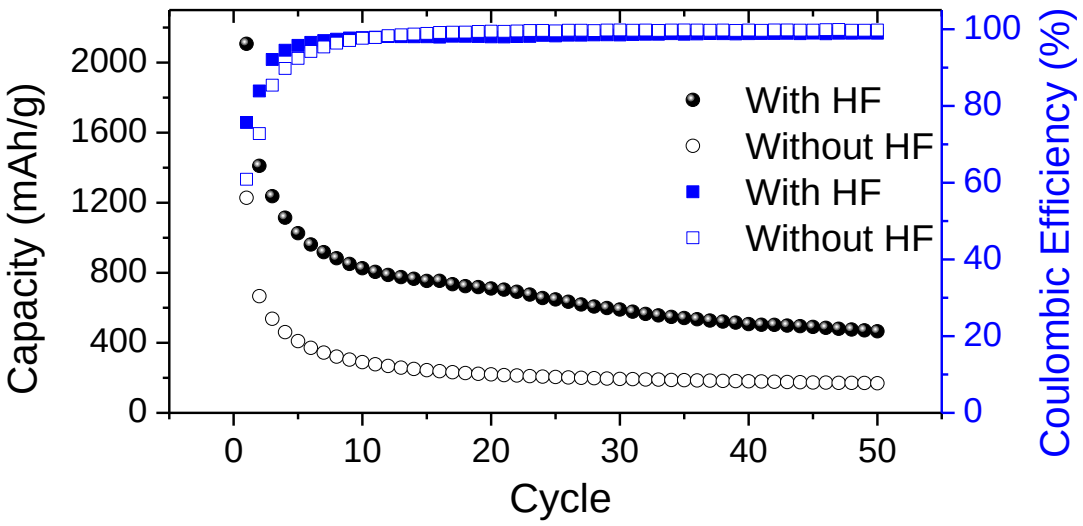

Figure 6.10 Specific capacity and coulombic efficiency of SiNWs electrodes with and without HF treatment, for 50 galvanostatic cycles. The charge and discharge rates were 0.5 A/g for the 1st cycle and 2 A/g for the subsequent cycles.

All the above discussed results make clear the high influence of the silicon oxide on the electrochemical performance of the LIBs, as well as the extreme usefulness of the simple HF treatment to improve the efficiency of the full etched SiNWs in LIBs.

In order to compare the quality of the produced SiNWs with commercial Si-based nanomaterials for batteries, a detailed study was performed. Commercial silicon nanoparticles (SiNPs) (Alpha Aesar) and commercial SiNWs/NPs mixture (US Research Nanomaterials) electrodes were prepared and characterized with the same procedure as our MACE SiNWs electrodes. The commercial nanomaterials were selected so their diameters were similar to MACE SiNWs. This consideration is very important because the size of the nanomaterials determines their surface/volume ratio[97,112], which is known to affect their electrochemical performance.

In **figure 6.11A** it is represented the EC potential spectroscopy data of the commercial electrodes. It can be observed that the MACE electrode possess much higher specific capacities than those for commercial Si-based electrodes. Even though the first lithiation

capacities of MACE and commercial Si NWs/NPs electrodes are similar (~2800 mAh/g), MACE electrode retained much higher delithiation capacity (2100 mAh/g) during subsequent delithiation step. As a result, the initial coulombic efficiency of the MACE electrode (78 %) was higher than those for the other electrodes (75% and 38% for commercial Si NPs and NWs/NPs mixture electrodes, respectively).

The DC curves of the electrodes during the first lithiation/delithiation cycle (**Figure 6.11B**) provide further evidence of the advantage for the MACE electrode. All of these Si-based electrodes show the characteristic cathodic peak (due to the alloying) lower than 0.15 V and anodic peak (due to de-alloying) at ~0.45 V during the first lithiation and delithiation. However, there is a difference between the electrodes in terms of the potential at which these peaks appear. During the first lithiation, the formation of the Li-Si alloy phase for commercial Si NWs/NPs electrode occurs at a slightly higher potential (0.1 V) than other electrodes (0.09 V for MACE electrode and 0.05 V for Si NPs electrode). Conversely, the anodic peak (de-alloying of Li-Si phase) for MACE electrode initially occurs at a lower potential, indicating that a relatively low anodic over-potential was induced for MACE electrode during subsequent delithiation. The over-potential is very important issue in batteries. Its existence indicates that more energy than the expected is being used to perform the reaction. This extra energy is being lost in the cell as heat due to poor electrical contact with the reacting material or slow electron transfer kinetics of the material. Therefore, as lower is the over-potential, more efficient in the cell.

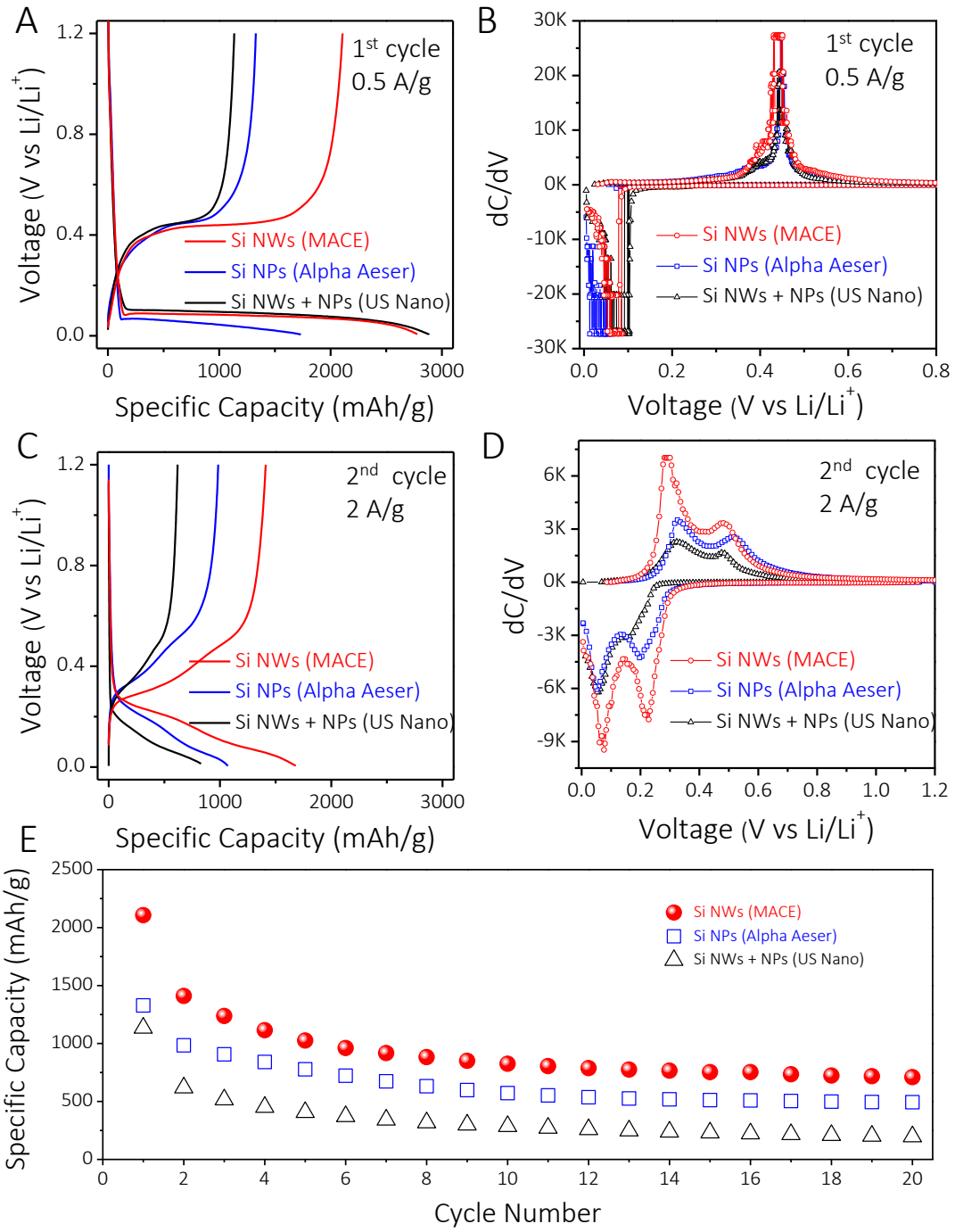

Figure 6.11 Electrochemical potential spectroscopy data of MACE and commercial electrodes of the first cycle, A) and B), and of the second cycle, C) and D). Evolution of the specific capacity with the cycles for the three mentioned electrodes at a rate of 0.5 A/g the 1st cycle and 2 A/g for the rest, E).

As mentioned above, both MACE and NWs/NPs electrodes exhibit similar lithiation capacity (~2800 mAh/g), thus they might undergo similar volume expansion over 200%

(ideally ~300% when reaching maximum specific capacity of 3579 mAh/g with formation of $Li_{15}Si_4$). However, MACE electrode shows higher delithiation capacity with lower anodic over-potential, which indicates that the electrode could better maintain its electrically conductive network after this huge volume variation. Additionally, during the next cycle at 2 A/g, MACE electrode exhibits much higher specific capacity (**Figure 6.11C**) and higher peak intensity (**Figure 6.11D**) than other electrodes. After galvanostatic charge/discharge tests at 2 A/g for 20 cycles, the specific capacity of MACE electrode gradually decays to 710 mAh/g (**Figure 6.11E**), which is commonly observed in Si based electrodes mainly because the pulverization and loss of electrical contact due to the large volume variation during alloying/de-alloying reactions. Nevertheless, MACE electrode displays better cycling performance compared to the other commercial Si-based electrodes, which retain less than 500 mAh/g after 20 cycles in latter electrodes.

The above results prove better electrochemical performance of our MACE electrode when compared with commercial Si electrodes, with similar medial size. However, compared with other present Si-based anode studies with smaller nanomaterials, the results are not as satisfactory. In **figure 6.12A**, it is shown the VP of an electrode composed by commercial SiNPs (US Research Nanomaterials) with particle size lower than 80 nm, considerably smaller than our SiNWs (~200 nm). In the mentioned figure, it can be appreciated an outstanding electrochemical performance of the SiNPs even after 10 cycles, maintaining a specific capacity around 2100 mAh/g. In comparison, MACE electrodes, **figure 6.9I**, only retained ~820 mAh/g after the same cycling length.

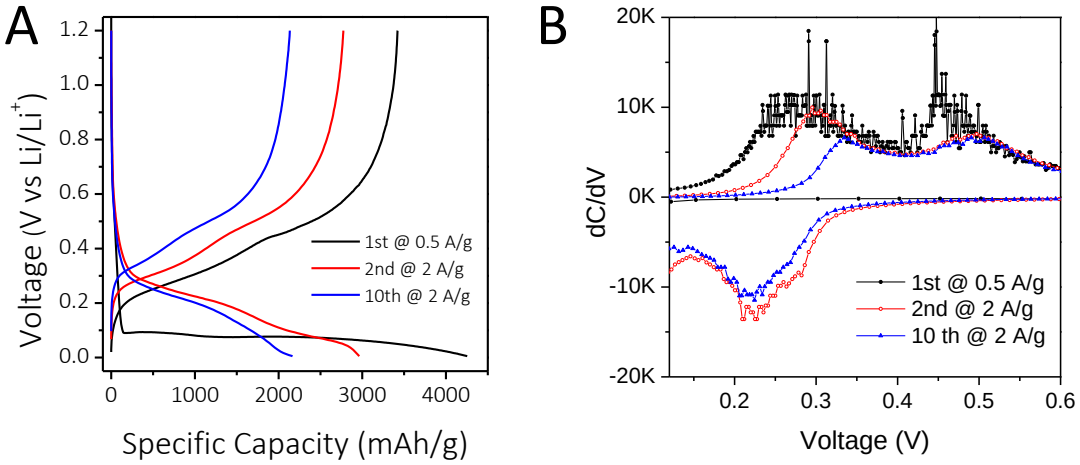

Figure 6.12 Voltage profile, A), and differential capacity curves, B), of SiNPs electrodes of the first, second and tenth cycle.

Moreover, the anodic peaks on the DC curves, **figure 6.12B**, present an absence of the two-phase transition peak, at ~0.45 V, corresponding to, presumably, the delithiation of the crystalline $Li_{15}Si_4$. This peak cannot be observed even for the first cycle, what contrast with all the tested Si nanomaterials with bigger dimensions (see **figure 6.11B**). Despite it is not clear the nature of the reaction behind this sharp peak, its shape makes clear that is a two-phase region reaction. Consequently, its absence is an advantage.

On the other hand, the DC curve of the SiNPs electrodes, **figure 6.12B,** reveals a huge shifting of the voltage position of the anodic peaks as the cycles advance. This increasing overvoltage means that with the cycling, the contact with conductive matrix in which the SiNPs are embedded, is being degraded. This effect hinders the cycling performance of the battery in the long term. Therefore, in order to investigate more deeply this effect, the morphology of the SiNPs electrodes were studied by FESEM, **figure 6.13A**. The morphological study revealed that even before the cycling, the electrodes presented huge cracks all over the surface. This is symptomatic of poor cohesion, which could explain the overvoltage observed in the differential capacity curves.

Under these premises, we decided to make a mixture of the SiNPs and the MACE SiNWs in order to take advantage of the good electrochemical capacity of the SiNPs while keeping good integrity of the electrical network shown by the SiNWs.

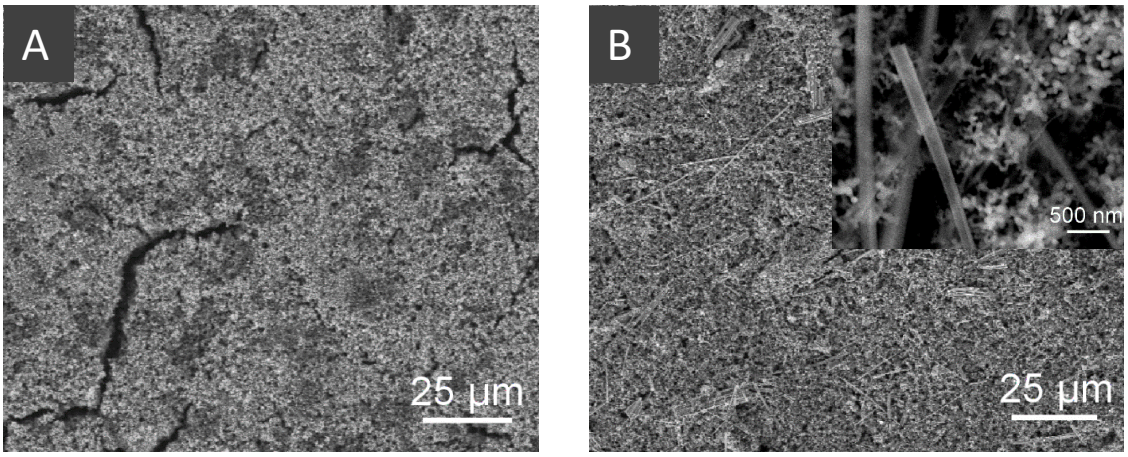

Figure 6.13. SEM images of a SiNPs electrode, A), and the hybrid SiNWs/SiNPs electrode, B). Inset in B) is displayed a closer SEM image of the SiNPs/SiNWs mixture.

Thus, 0D-1D mixture electrodes were fabricated by mixing MACE SiNWs and the SiNPs in a mass ratio 1:1. As first result, it was observed that with the addition of the SiNWs the cracks did not appeared, **figure 6.13B**. Taking a closer look at the material, inset of **figure 6.13B**, it was also observed that the mixing of the material resulted in a homogenous distribution of both SiNWs and SiNPs. The SiNPs were found surrounding the SiNWs, preventing the formation of clusters of SiNWs or SiNPs.

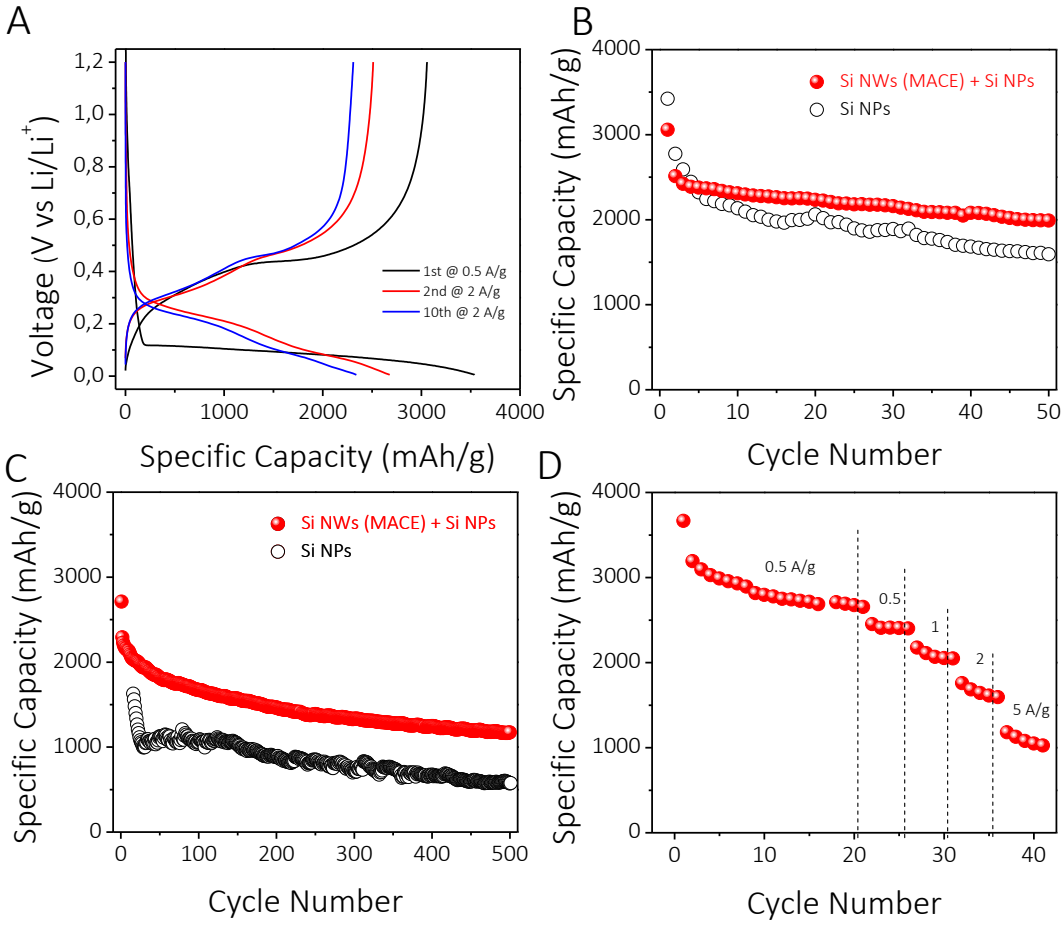

Figure 6.14 In A) is displayed the voltage profile from the galvanostatic cycling of the hybrid electrode on its first, second and tenth cycle. Specific capacity as a function of the cycles for the hybrid electrode and the SiNPs electrode for 50 cycles B) and extended to 500 cycles C). Specific capacity of the hybrid electrode for different charge/discharge rates D).

Additionally, the electrochemical characterization of the MACE SiNWs /Si NPs hybrid electrode, **figure 6.14A**, revealed a delithiation capacity of 2764 mAh/g, which is between the capacity values for single component Si-based electrodes (SiNPs electrode and MACE SiNWs electrode). This is very common feature observed for the general mixture system under lever rule, but surprisingly, this hybrid electrode maintained much higher specific capacity in further cycling. After 10 cycles, the delithiation capacity for the hybrid electrode (2307 mAh/g) is higher than SiNPs electrode (2135 mAh/g) despite of its lower specific capacity values during initial cycling stages. Moreover, in the voltage profile, **figure 6.14A,**

the increasing over-voltage shown by the SiNPs electrode is not presented in the hybrid one. Definitively, the absence of this overvoltage in the hybrid electrode contributes to the improved capacity retention.

Finally, in **figure 6.14B** can be appreciated that the hybrid electrode retained 25% more specific capacity after 50 cycles, clearly indicating better cycling performance. To further investigate the long-term cycling stability of these Si-based electrodes, faster charge and discharge measurements were carried out at a constant current density of 2 A/g over 500 cycles, shown in **figure 6.14C**. While the specific capacity of Si NPs electrode is markedly decreased to ~1000 mAh/g at the earlier cycling stage (1~50 cycles), under faster charging/discharging condition, MACE SiNWs/Si NPs hybrid electrode only shows gradually decaying of its capacity during the overall cycling stage. After 500 cycles, hybrid electrode retained specific capacity of 1990 mAh/g, 25% higher than that of Si NPs electrode (1593 mAh/g), indicating improved cycling performance based on the 0D-1D hybrid structure. Additionally, MACE/SiNPs hybrid electrode exhibits quite competitive rate performance when cycled at current densities from 0.5 to 5 A/g, **figure 6.14D**; the hybrid electrode only suffered a 44% decrease in capacity when the current density was increase by a factor of 10 (0.5−5.0 A/g).

The above exposed results demonstrate the exceptional electrochemical properties of the hybrid electrode, probably due to the synergistic effect which comes from the mixture of the different dimensional structure (0D-1D hybrid). Its performance has proven to be superior to any commercial Si-based electrodes tested, being even attractive among the present Si-based anode studies[6,8,9,128–131] because of its high cycling performance even at high current densities. The quite impressive electrochemical results and easy transferability to the industry, makes this material a very promising candidate for future LIBs.

6.3.3 Free-standing SiNWs/CNTs electrodes

The study of the SiNWs for LIBs was further extended with the formation of the free-standing electrodes. These electrodes take advantage of the high conductivity and mechanical support that the CNTs offers, forming a well entangled composite where the active material is involved in CNTs. The advantage of using CNTs instead of the standard polymer binder/carbon black combination, is that their higher mechanical/electrical properties could improve the cycling of the Si-based anode. In this type of electrodes, the ratio between the active material and the CNTs is very critical[132]. If the amount of CNTs is too low, the CNT matrix may not be conductive enough or unable to compensate the dimensional changes during lithiation/delithiation. This could influence the LIBs by inducing an overvoltage or a fast degradation. On the other hand, if the amount of CNTs is too high, the total amount of active material in the electrode is significantly reduced, lowering the capacity of the electrode. Due to the required balance between attributes of one excess and the other, it is necessary to investigate the optimal SiNWs/CNTs ratio. In literature, this subject has been addressed[132,133], however the significant differences between mixing method and materials used, makes necessary a specific study for our materials. Most of the Si/CNTs mixtures reported, are situated in a range between the 10% and 30% of CNTs[133–137] respectively to the Si content. Therefore, that CNTs range will be the initial concentration of the presented study.

Free-standing electrodes with CNTs percentages of 5%, 10%, 20% and 30% were fabricated by the percolation method described in the experimental section. Their morphology was studied by FESEM, **figure 6.15**, obtaining in all cases a good mixture with no significant differences between top and down sides. In **figure 6.15A**, it is seen how the CNTs completely covers the SiNWs forming a very compact matrix with most of the SiNWs fully covered by CNTs. However, the degree of coverage of the SiNWs is highly influenced by

the CNT percentage. **Figures 6.15B-E** show the surface of the electrodes with increasing amount of CNTs, from 5% to 30% respectively. In these images it can be clearly seen how, for the lower CNT percentages, an important amount of SiNWs are not coated. This lack of coverage mainly observed in the 5% samples and in some areas of the 10%, potentially affect the resistivity of the medium and their electrochemical performance.

In order to further characterize the electrodes, their sheet resistance (R_S) values were obtained through the 4-point probe method, **figure 6.15F**. The displayed R_S values agree with the coverage observations made by FESEM, pointing out that at very low concentrations of CNTs, the electrodes show a high resistance. The increase of CNTs concentration rapidly reduces the observed R_S, starting with a very high value of 260 Ω/□ in the 5% sample and only showing 30 Ω/□ in the 20% sample. At higher percentages, the R_S reduction is much less sharp, only getting 15 Ω/□ for the 30% sample. This small R_S reduction comes at the expense of a 10% SiNWs loss, making this percentage less interesting than the 20%. The trend of **figure 6.15F** clearly shows an exponential decay of the R_S with the increase of CNTs, which tends to the 100% CNTs R_S value of 2,7 Ω/□. This behavior emphasizes the problem shown between the 20% and 30%, a minor gain of conductance with a major loss of active material. For this reason, the 20% CNT percentage was fixed as the ideal percentage for the electrodes used in the LIBs fabrication.

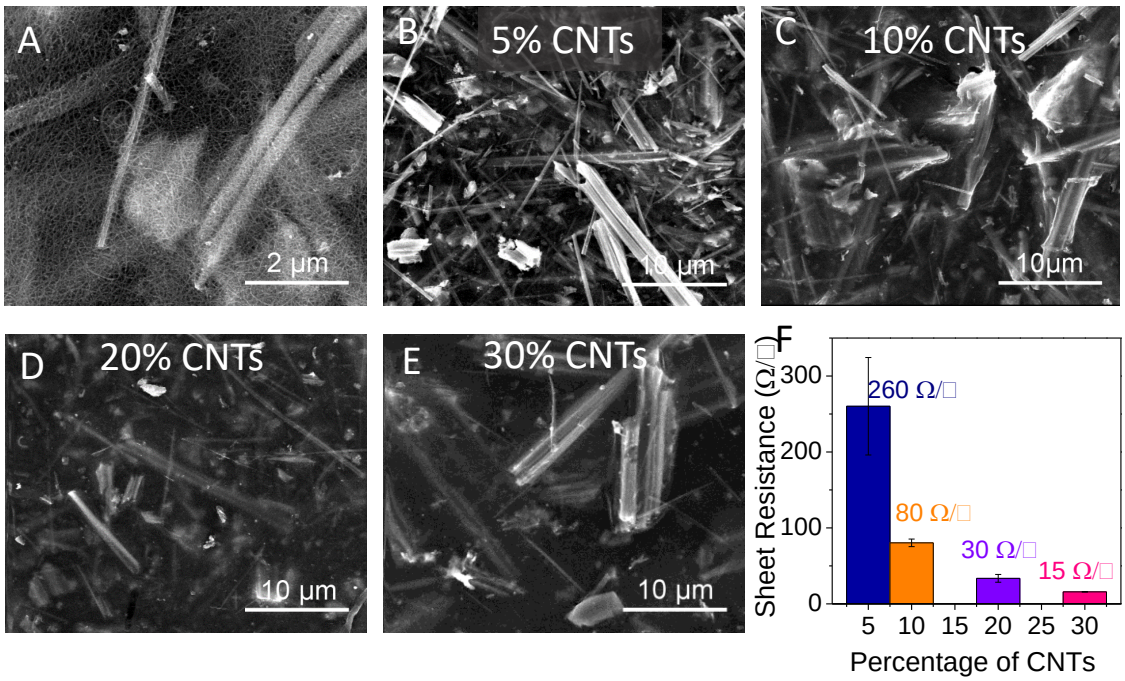

Figure 6.15 FESEM top-view images of electrodes composed by SiNWs and CNTs A) to E). Electrodes B) to E) have different CNTs/SiNWs ratios which are shown in the images. In F) a comparative study of the sheet resistance as a function of the CNTs/SiNWs ratio, is shown.

The LIBs were assembled as described in experimental section, and then they were subjected to galvanostatic cycling. The specific capacity shown by these SiNWs/CNTs electrodes at the first cycle was very high, **figure 6.16A**, being initially 3300 mAh/g with a quite high CE of 79%. Surprisingly, the capacity loss in the second cycle was very small showing an extremely high CE of 98%. The high capacity retention from the first to the second cycle contrast with our results with the on-foil batteries, where capacity loss was quite sharp. This behavior can be attributed to the high mechanical toughness of the CNT conductive matrix in which the SiNWs are imbibed. The CNT matrix compensates the dimensional changes of the Si avoiding the contact loss due to the crumbling[132]. The mentioned effect is well kept during the cycling, showing a very slow capacity decay which allow the obtainment of a specific capacity of 2500 mAh/g after 40 cycles. These results highly contrast with our previous results of the SiNWs, which after the same cycling only shown 500 mAh/g.

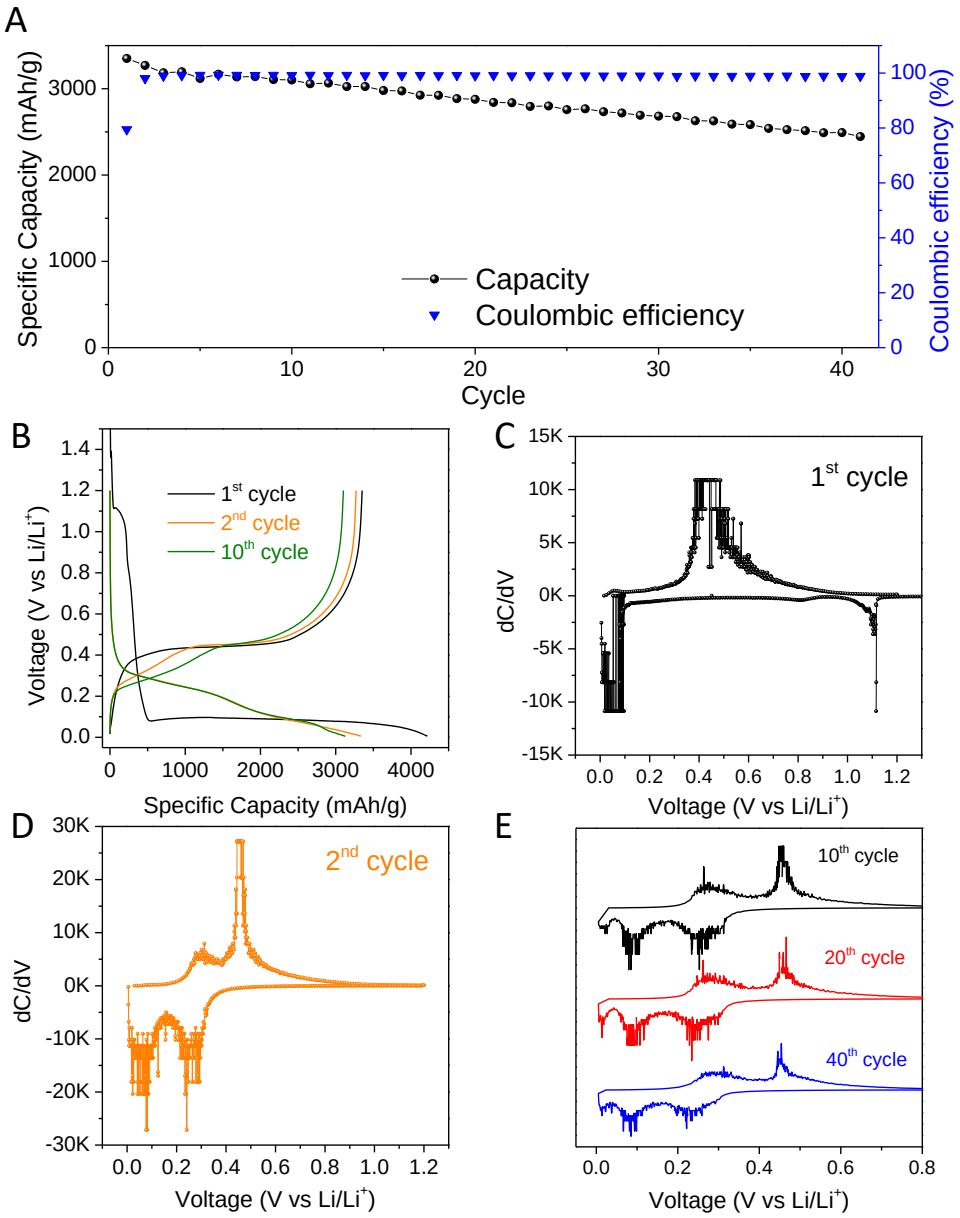

Figure 6.16 Electrochemical spectroscopy data of the 20% CNTs/SiNWs electrode. A) Specific capacity and CE as a function of the cycle number. B) VP of the cycles 1, 2 and 10. C) to D) DC curves of cycles 1, 2 respectively and E) DC curves of cycles 10, 20 and 40.

To further delve into the electrochemical performance of the electrodes, VP and DC curves were obtained from the galvanostatic cycling, **figure 6.16 B-E**. The VP for the first cycle in **figure 6.16B,** shows the typical plateau at 100 mV from the lithiation of the c-Si, which is further confirmed by the DC curve in **figure 6.16C**. However, in this first discharge it can

also be detected an anomalous behavior at high voltages. In the DC curve this behavior is observed as a sharp peak at 1.1 V, followed by a much smaller peak at 0.8 V. The fact that these peaks are only present in the first cycle, compare **figure 6.16C** with **figure 6.16D**, reveal that are due to irreversible interactions between Li-ion electrolyte and CNT+Si active material. Indeed, the 1.1 V and 0.8 V peaks can be identified as the reduction of oxygen-containing functional groups at the surface of the CNTs[138] and the formation of SEI[111,138] respectively.

Very interestingly, in **figure 6.16E**, it can be observed that, with the cycling, no significant overvoltage is induced, keeping the lithiation/delithiation peaks at the same position even after long cycling. This indicates that the CNT matrix is well preserved with cycling and the contact with the SiNWs is not significantly altered after their high volume expansions and crumbling.

Apparently, the above results indicate that the CNTs matrix significantly enhance the electrochemical performance of the SiNWs by solving one of their biggest problems, the contact loss due to the crumbling. However, it would be necessary to extent the cycling to confirm if the CNTs effectively suppress the effect of the crumbling as the first analysis suggest.

The extremely good electrochemical performance and good cycling that this free-standing electrode presents, makes them a very promising material for the LIBS. Moreover, their good electrochemical properties not only surpass the more traditional ways of forming SiNWs electrodes, but also current researches on the CNTs free-standing electrodes area[113,135,136].

6.4 Conclusions

In this chapter, the MACE has been applied to etch the whole thickness of the c-Si wafers. This improvement of the MACE procedure was done to obtain a sufficient amount of

SiNWs to apply in SiNWs-based electrodes for LIBs. The analysis of the full-thickness MACE SiNWs revealed an oxide layer on the surface of the SiNWs which thickness depends on the diameter of the SiNWs. This observation permitted the design of an extra oxide removal step in the SiNWs synthesis for the optimization of SiNWs based LIBs.

Once characterized, the SiNWs were used for the fabrication of anodes for LIBs. The electrode formation was performed by two different methods. The first one was the deposition of SiNWs, mixed with carbon black and a binder on a Cu foil. The second one was the formation of free-standing CNTs/SiNWs electrodes.

The batteries assembled using the first method, shown a good electrochemical performance compared with other commercial Si-based nanomaterials. Additionally, the SiNWs were mixed with small SiNPs forming a homogenous hybrid electrode. The cycling performance of this hybrid electrode was much better than the one exhibited by the components separately, owing to the synergy observed between the two nanomaterials.

Due to the novelty of the free-standing electrode formation process, the first research step in the study was the optimization of the CNTs/SiNWs ratios. Several percentages of CNTs were tested attending to their morphology and sheet resistance. Finally, the percentage of the 20% resulted the optimal ratio, and it was selected for the assembly of the LIBs. The obtained electrodes exhibited extremely good specific capacities and very stable cycling. This improved electrochemical performance can be attributed to the influence of the CNT matrix, which significantly reduced the affectation of the crumbling to the capacity.

Chapter 7:

Amorphous SiNWs for lithium ion batteries

7.1 Introduction

In the previous chapter it has been demonstrated the huge potential of the MACE SiNWs for the LIBs. However, the experimental procedure is quite complex and the MACE usually leads to a low mass yield; drawbacks which could difficult its use in the industry. In order to improve this aspect, in this chapter, a different approach was addressed: the direct growth of the SiNWs on the electrode. It was proposed to directly grow, over the Cu foil, a Si film which could act as substrate for the etching of the SiNWs by MACE. Through this method, the SiNWs would be directly attached to the Cu without the use of any binder, and the etching process would be more efficient, losing less material in the process.

An important difference it can be find in this process is that the deposited Si films are usually amorphous. It is possible to recrystallize the deposited films, but the processes are usually costly. Besides, it would require high temperatures which Cu foils cannot stand. However, as seen in the EC characterization in the previous chapter, the crystallinity of the SiNWs plays no role in the LIBs, since in the first cycle the Si gets amorphized. Indeed, the crystallinity is a drawback. When compared with amorphous materials, the c-Si much more compact structure have more difficulties accommodating the volume expansion due to

lithiation, leading to a higher material pulverization[139]. For this reason, the amorphous silicon (a-Si) has attracted great attention in the field of the LIBS[140–145].

Despite of an internal structure more suited to insert lithium, when the a-Si is deposited as film, the volume expansion produces cracks in the material and the capacity rapidly fade[143]. This problem is directly related with the film morphology, and, because of that, the SiNWs could be a good response to it. Indeed, the pillar structures are known to have better expansion capabilities[146] and better surface-volume ratio[141], which could improve the electrochemical performance of the material.

The growth of SiNWs on amorphous substrates was firstly reported by Douani *et al* [147] in 2011. However, their research focused on the influence on the impurities in the growth rather than exploring any application. Moreover, to our knowledge, since that first report, the amorphous silicon nanowires (a-SiNWs) has not been used in any new work in the literature. In this chapter the application of the a-SiNWs in the LIBs is explored and their electrochemical performance analysed.

7.2 Experimental

7.2.1 Hydrogenated amorphous silicon (a-Si:H) growth

For the growth of hydrogenated amorphous silicon (a-Si:H), two types of substrates were used: intrinsic monocrystalline Si wafers (100) with thicknesses 525 μm and resistivity > 10000 Ωcm and Cu foils (purity 99.99%, MTI) with thicknesses of 9 μm. Previous to the deposition, the Si substrates were cleaned with HF 5% and rinsed in DI water. The Cu substrates were cleaned with acetone and IPA subsequently. The reason behind the use of the intrinsic Si wafers instead of the p-doped Si wafers used in the rest of the chapters, is that to obtain the hydrogen content of the a-Si:H films by FTIR, is highly recommended to use substrates without any doping, due to possible interferences.

The growth of the a-Si:H was performed by two techniques: plasma enhanced chemical vapor deposition (PECVD) and radio frequency magnetron sputtering (RF-MS).

The silicon source, for the RF-MS was an intrinsic Si target of purity 99.999% (Goodfellow). The power during the growth was set to 100 W to achieve a growth rate of 0.8 Å/s, the substrate temperature was set to 180ºC and the inlet gases for the plasma were Ar (Premier 99.9992%, Carburos Metálicos) and H_2 (Premier Plus 99.9992%, Carburos Metálicos). The gas H_2/Ar mixture was ranged from 1:3 to 1:1 in volume with a flow of 3 sccm and a chamber pressure of 9 mTorr. The gas mixture proportions were ranged in order to investigate the influence of those parameters in the properties of the deposited material.

On the other hand, the deposition via PECVD (MVSystems Inc) was performed with an inlet flux of SiH_4 (purity 99.999%) of 20 sccm at a pressure of 400 mTorr. The substrate temperature was set to 198ºC and the power of the RF source was 1 W.

7.2.2 MACE on a-Si:H

At it has been commented in chapter 3, the MACE is highly influenced by the structure of the Si where it is applied. In this case, where the MACE is applied on an amorphous Si layer, two significant differences can be found with the etching on c-Si. The first difference is the lack of crystalline structure on the Si. This implies that there is no preferential etching direction and, therefore, the SiNWs could grow slanted. Furthermore, the material shows lower densities and less number of backbonds, so it is much more sensitive to the MACE. Thus, the material is likely to show higher etching rates even for the secondary etchings.

The other significant difference is the limitation in the amount of material. The chapter objective is to grow the a-SiNWs directly on the Cu substrates, therefore, the etching has to be restricted to the thickness of the deposited a-Si:H. If the etching goes further than the a-Si:H thickness, the Cu substrate, which is known to be a catalyst of the MACE[13], would

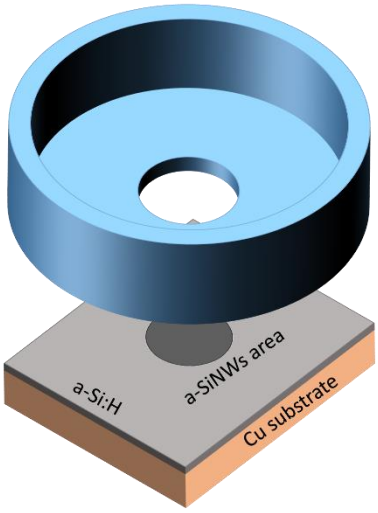

Scheme 7.1 Diagram of the experimental layout of the MACE on a-Si:H over a Cu substrate.

induce an etching on the base of the a-SiNWs peeling off the whole layer. Also, for the same reason, the MACE cannot be done just immersing the sample into the etching solutions. The process has to be limited just to the side where the a-Si:H is deposited, excluding the borders of the sample. In order to implement those changes experimentally, special cells were fabricated fulfilling the requirements, **scheme 7.1**. Cells with different hole diameters and shapes were fabricated. For characterization purposes, cells with small size (1 cm diameter) and round shape holes were used. On the other hand, for the fabrication of electrodes, cells with much bigger reaction area (4.5 cm x 4.5 cm) were used. The large area cells, allowed the fabrication of numerous electrodes with the same SiNWs length and growth conditions. The mentioned improvement resulted on a very good electrode repeatability.

In the aforementioned cells, both baths, $AgNO_3$/HF and H_2O_2/HF, were consecutively done with an intermediate cleaning with DI water. The molarity of the HF of the first bath was kept at 4.8 M, as described in chapter 3, while the molarity of the $AgNO_3$ was ranged between 0.01 M and 0.0025 M in order to investigate its influence on the growth of the a-SiNWs. The molarities of the second bath were fixed at the values used in chapter 3, 4.8 M for HF and 0.2 M for the H_2O_2. The duration of the first bath was fixed to 30 seconds, while for the second bath it was ranged between 30 seconds to 3 minutes, depending on the desired length.

Once the MACE procedure was done, the samples were rinsed in DI water and dried in a desiccator for a whole night.

7.2.3 Electrodes processing

For thin film materials, the electrode cutting is probably one of the most important steps in whole process of the electrode formation. As discussed in the results section, a high precision electrode cutting is crucial to obtain the active mass. In order to achieve the highest precision possible, all the electrodes were cut in circular shape with a diameter of 1.2 cm by Nd:YVO_4 (Super Rapid-HE, Coherent) laser with pulse length of 15 ps, wavelength of 532 nm, frequency of 100 kHz and power of 3.5 W. The extreme precision of this cutting technique results on an area with an almost negligible error. In **figure 7.1** a SEM image of the edge of the laser cut electrode is displayed. As can be seen, the precision is extremely high.

A diagram of the whole fabrication process is shown in **scheme 7.2**.

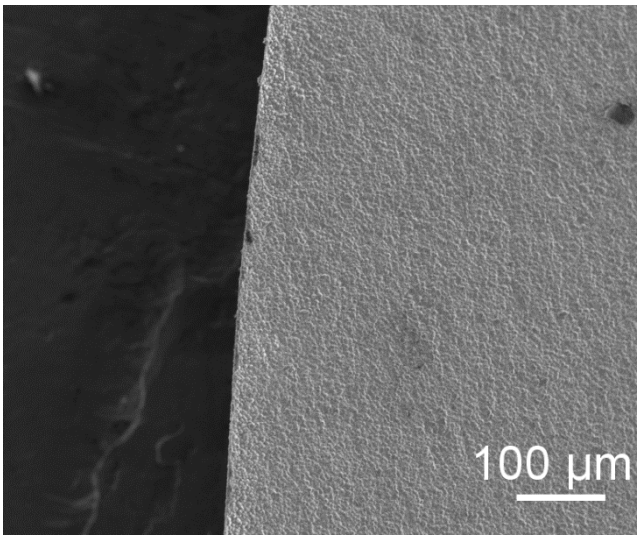

Figure 7.1 Top-view SEM image of a laser cut electrode.

The batteries assembly was performed as it was exposed in the previous chapter. The characterization of the batteries was also performed by galvanostatic cycling with standard rates of 0,5 A/g for the first cycle and 2 A/g for all the consecutive cycles.

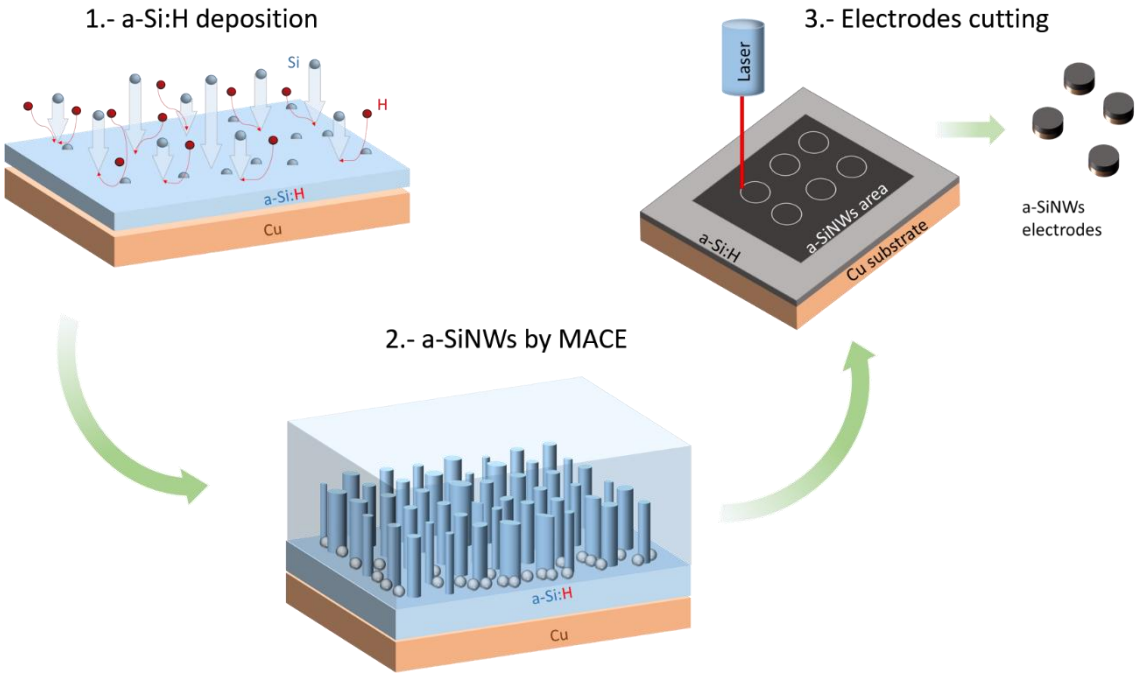

Scheme 7.2 Diagram of the a-SiNWs electrode fabrication process

7.3 Results and discussion

7.3.1 Growth of a-SiNWs

As it has been exposed in the experimental section, the MACE on a-Si:H present important differences with the MACE done in c-Si. Therefore, an optimization of the experimental parameters is required in order to apply it on further steps.

As first step, the morphology of the deposited films by the different techniques was explored by FESEM, **figure 7.2**. Despite of quite similar growth conditions, the morphology of the films was considerably different for the two techniques. The samples grown by PECVD show a dense appearance, **figure 7.2A**, while the samples grown by RF-MS looks much more porous with a columnar morphology, **figure 7.2B**.

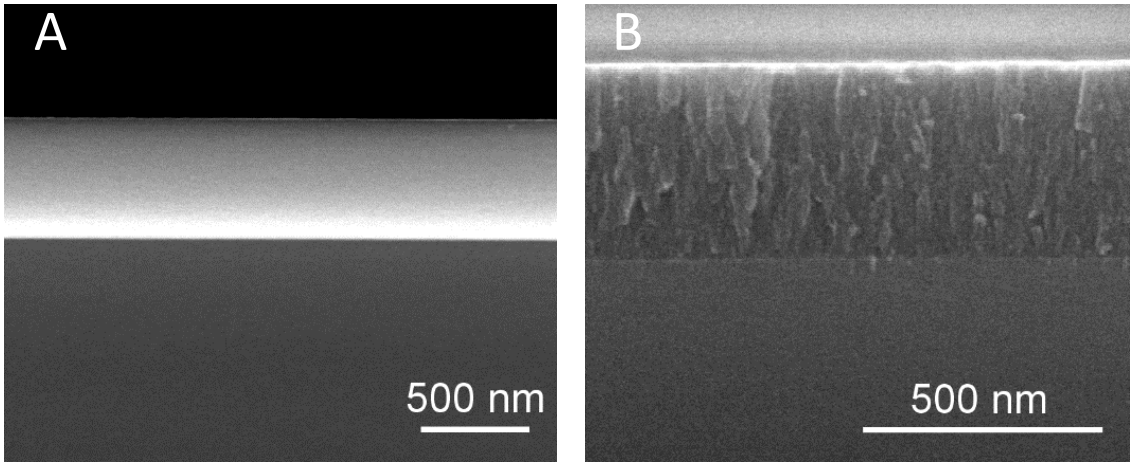

Figure 7.2 FESEM images of a-Si:H by PECVD, A), and RF-MS, B).

The investigated films, deposited on c-Si substrates, were subjected to the MACE process. The process was applied to films on top of the c-Si because in case of an excess of etching time, the etching can continue in the c-Si. However, if the process would have been applied on an a-Si:H/Cu sample, the excess of time would had led to the removal of the film.

The adjustment of the MACE parameters was begun with the investigation on the influence of $AgNO_3$ concentration in the electroless deposition. In this study, the duration of each bath of the MACE were fixed to 30 seconds and the reactants concentrations of the second bath were kept as mentioned in the experimental section of the chapter. Firstly, a concentration of 0.01M was used, as it has been done in previous chapters. Surprisingly, this concentration led to the removal of the a-Si:H film grown by both techniques, only observing SiNW growth in the c-Si substrate, **figure 7.3 A-B**.

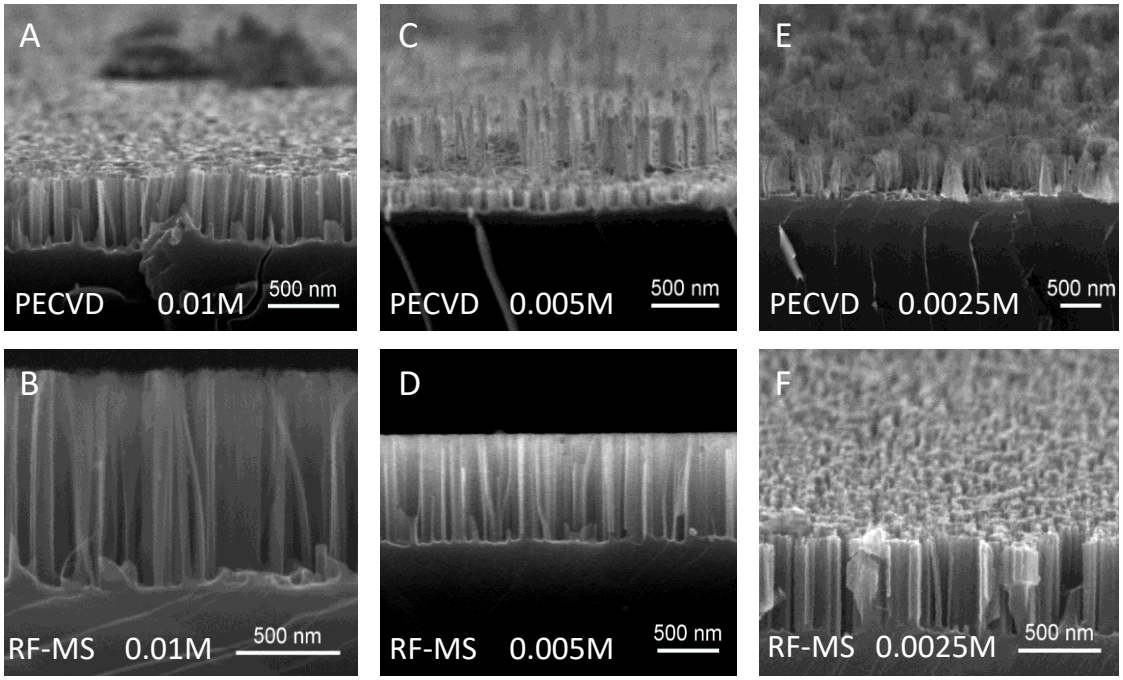

Figure 7.3 FESEM images of a-Si:H films on c-Si after the MACE procedure. On A), C) and E) the a-Si:H were grown by PECVD while on B), D) and F) the deposition was conducted by RF-MS. In each image, the concentration of $AgNO_3$ used is displayed.

After this result, the MACE was repeated slightly reducing the $AgNO_3$concentration to 0.005M. Again, in the RF-MS sample, the etching resulted in the growth of SiNWs in the c-Si underneath the removed a-Si:H layer, **figure 7.3D**. On the other hand, in the PECVD sample it was observed a-SiNWs growth, **figure 7.3C**, but much sparser than their counterpart in c-Si.

Lastly, the molarity of the $AgNO_3$ was set to 0.0025M, while keeping the rest of the parameters untouched. This set of parameters resulted in a very dense growth of a-SiNWs on the PECVD sample, **figure 7.3E**, while in the RF-MS only c-SiNWs from the substrate were observed, **figure 7.3F**.

Due to the strong opposition of the results from one type of film to the other, the electroless deposition of the Ag NPs was performed without the subsequent etching step. The reason for applying only the half of the MACE, is to observe the differences between the films in

the first instants of the SiNWs growth. For this test, as well as for all the following MACE procedures in this chapter, the molarity of 0.0025M was selected.

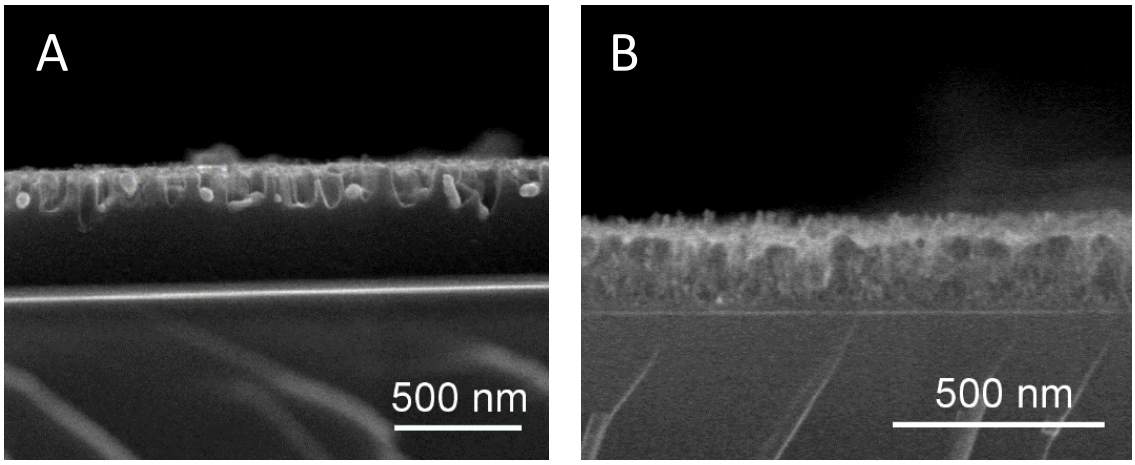

Figure 7.4 FESEM images of the an electroless deposition of Ag NPs on a-Si:H grown by PECVD, A), and RF-MS, B).

After the application of the electroless deposition, it was observed that while the PECVD samples presented an Ag NPs deposition on the surface, **figure 7.4A**, similarly to the observed in c-Si; the samples grown by RF-MS shown an extreme texturization with a considerable thickness loss, **figure 7.4B**. This means that the RF-MS film gets rapidly removed even for the mild etching of the electroless deposition.

The above results clearly indicate substantial differences between the growth methods of the films. This differences have such high influence in the MACE process, which even leads to precluding the a-SiNWs growth. In order to better understand the differences and their impact on the MACE process, a much thoroughly characterization of the films was performed.

Hydrogen in a-Si:H is known to passivate the dangling bonds of the amorphous silicon[89]. This translates in a better stability of the material which tends to be less reactive with its surroundings. Due to the lack of studies on the influence of the hydrogen on the formation

of a-SiNWs by MACE, we cannot know beforehand the role it plays on the success of the process. However, because the huge importance it has in the passivation of the surface, a poor incorporation of hydrogen on the RF-MS films could be behind its low stability against the MACE. In order to investigate this possibility, the hydrogen content was studied by FTIR measurements on the films. As commented in the experimental section, intrinsic c-Si wafers two side polished wafers have to be used as substrates for this technique. The reason why these substrates are required, is that they are mostly transparent in the wavelength region of the technique, allowing the transmission configuration necessary to extract the hydrogen content (c_H).

The c_H obtainment of the a-Si:H films form FTIR spectrum, is based on the analysis of the two main bands presented in the material; one centered in 630 cm^{-1} and other between 2000 and 2100 cm^{-1}. The first band is known to contain the rocking and wagging modes of all possible Si-H bondings, being related with the total amount of the hydrogen on the samples[148]. On the other hand, the second band arises from the stretching modes, which slightly changes their central frequency depending if Si-H bond corresponds to a monohydride (SiH) or polyhydride (SiH_x)[149]. Therefore, this band allows the identification of the form in which the hydrogen is incorporated, something which have deep implications in the morphology and characteristics of the deposited material. Moreover, the 2000-2100 cm^{-1} band can also be used to obtain the c_H, helping us to double check the c_H value obtained from the first band.

The analysis of the c_H was performed following the BCC method[148] with the corrected proportionally factors of Langford *et al* [149]. By this method, the c_H is obtained from the integration of the two bands, **Equation 7.1** and **Equation 7.2**, where A_{630}, A_{2000} and A_{2100} are the proportionally factors.

$$c_H = A_{630}\int_{-\infty}^{\infty}\frac{\alpha_{630}(\omega)}{\omega}d\omega \qquad \textbf{Equation 7.1}$$

$$c_H = A_{2000}\int_{-\infty}^{\infty}\frac{\alpha_{2000}(\omega)}{\omega}d\omega + A_{2100}\int_{-\infty}^{\infty}\frac{\alpha_{2100}(\omega)}{\omega}d\omega \qquad \textbf{Equation 7.2}$$

In **Equation 7.2** two contributions are clearly distinguished in the stretching band, one in 2000 cm^{-1}, which corresponds to the SiH, and other one at 2100 cm^{-1}, corresponding to the SiH_X. Is important to mention that in the polyhydride band are not only found the SiH_2 and the SiH_3, this band usually include other bonding configuration such as hydride clusters, internal voids etc.[89]; which are usually considered as defects and an indicator of poor quality of the material.

To explore the characteristics of the a-Si:H films deposited by PECVD and RF-MS; a set of 3 samples were prepared with approximately the same thickness. Two samples were grown by RF-MS, the first one without introducing hydrogen in the chamber during the synthesis, serving as reference, and other sample with an H_2/Ar flux ratio of $^1/_3$. The last of the three samples was grown by PECVD in the standard conditions. The FTIR spectra of these samples are shown in **figure 7.5A**. As expected, the RF-MS sample grown without H_2 show none of the vibrational bands of the SiH (displayed in the figure as discontinuous straight lines). On the other hand, the PECVD sample show very clear SiH bands with a stretching band clearly centered in 2000 cm^{-1} which indicates a majority of monohydride composition. Performing the BCC method for the obtainment of the c_H, we can get a total amount of hydrogen of 12.5%, which approximately 10.8% comes from SiH and 1.7% from polyhydrides.

Surprisingly, the RF-MS sample assisted with H_2 during the growth only show a faint band in the 630 cm^{-1}. The stretching band is a bit more visible, but only the component centered in 2100 cm^{-1} is appreciable. This result clearly indicates a majority incorporation of polyhydrides, formation of microvoids and anomalous microstructures[89]. A high intensity of

the 2100 cm^{-1} component, is usually related with a very high incorporation of H_2[149]. However, when the BCC method is applied on this spectrum, it is found a mismatch on the concentrations in each band, leading to the impossibility to apply the method accurately. This problem might arise from the fact that FTIR needs very homogenous layers, and the irregular film morphology observed by FESEM, **figure 7.2B**, might be disturbing the low frequency bands of the spectrum. Moreover, this columnar and porous shape observed in FESEM, is usually related with microvoids formation, which appears in the spectrum as a high polyhydride component. Summarizing, the rough morphology of the layer might be preventing the obtainment of an accurate c_H, but this morphology might be caused by a huge H incorporation in the form of ploy hydrides, what is coherent with the obtained spectrum. However, as the c_H cannot be precisely extracted, it cannot be identified if those microstructures come along with an excess of hydrogen or if we are only incorporating H in the form of polyhydrides. This matter is indeed important because it could help to reveal the role of the c_H in the success of the MACE etching.

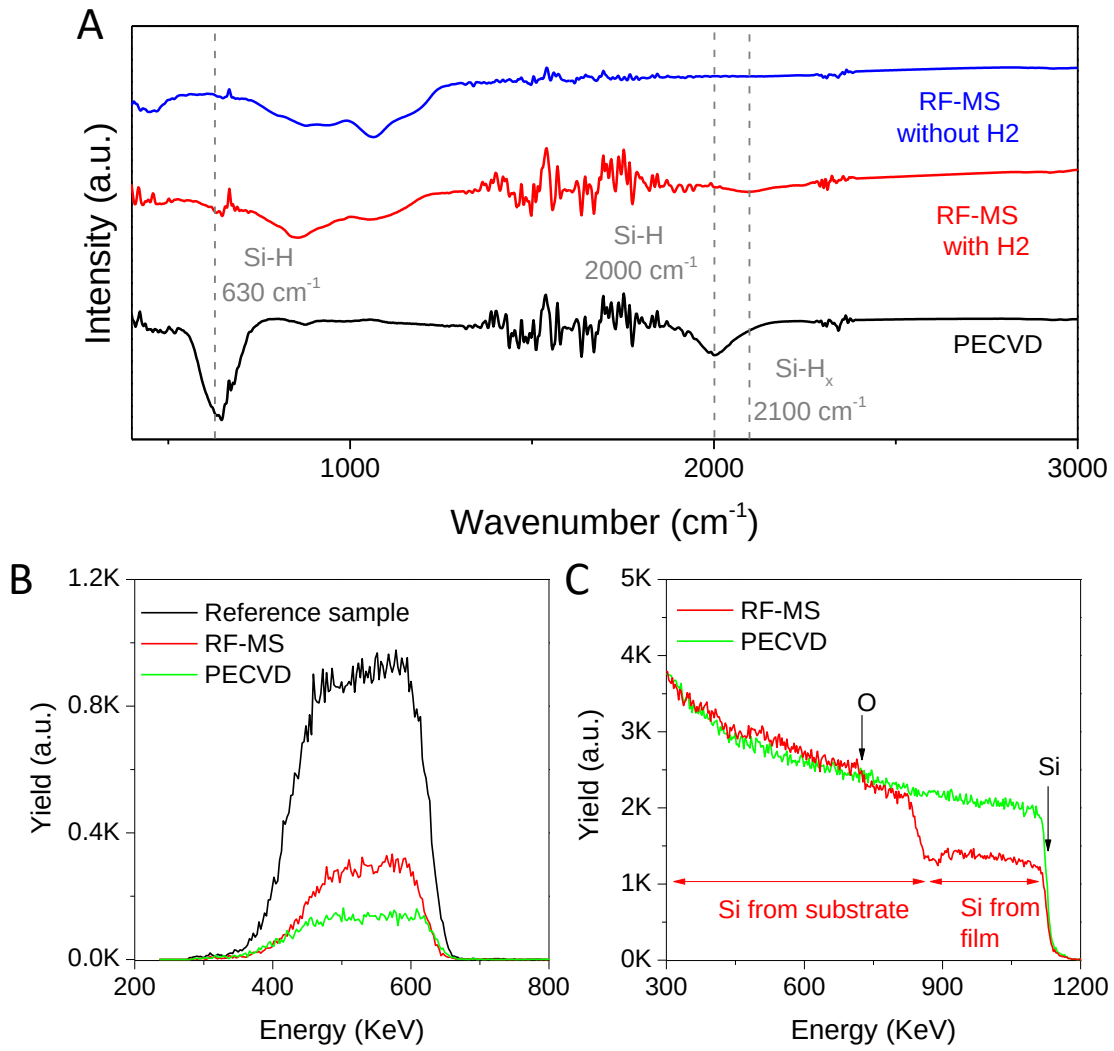

Figure 7.5 A) FTIR spectra of samples growth by PECVD and RF-MS with and without H_2 during the deposition. In dashed lines the rocking and wagging band (at 630 cm^{-1}) and stretching bands for the monohydrides (2000 cm^{-1}) and polyhydrides (2100 cm^{-1}). On B) and C) ERDA and RBS spectrum respectively, of a-Si:H deposited by RF-MS and PECVD.

In order to delve into the subject, RBS and ERDA measurements were performed on the of the PECVD and RF-MS samples (with H_2 during the growth). These techniques were done in the CMAM facilities of the UAM in a Tandem Cockcroft Walton accelerator. Both Ion Beam Analysis (IBA) techniques were simultaneously performed with helium ions of 2 MeV with a grazing incidence of 15º. The ERDA detector was at 30º relative to the incidence direction, and the RBS at 170º. As absorber for the ERDA, a 8.5 μm mylar film was used.

Results are displayed in **figure 7.5B-C**, where, in ERDA spectra, **figure 7.5B**, it is also shown a calibration sample of carbon containing a well-known amount of hydrogen (32%).

Very interestingly, ERDA spectrum, **figure 7.5B**, shows a stronger hydrogen signal in the RF-MS sample than in the PECVD one. The intensity of the signal is directly related with the atomic percentage of the element in the sample. Therefore, in RF-MS more hydrogen atoms are incorporated. Also, the flatness of the signals in all the samples indicates a homogenous distribution of hydrogen along the thicknesses.

On the other hand, the RBS spectra, **figure 7.5C**, shows an atomic percentage of silicon much bigger in the PECVD sample than in the RF-MS sample. The difference is also observable in the interface between the RF-MS deposited film and its c-Si substrate, where the sharp increase of the signal indicates a sudden change in composition to a richest Si compound (the c-Si substrate). Solely the presence of hydrogen would not be able to explain this difference. However, the explanation can be found at lower energies on the RBS spectra. Around 750 KeV the recoil of the oxygen atoms is found, which shows no contribution in the PECVD samples, but a noticeable intensity in the RF-MS ones. This indicates that while the RF-MS films have a presence of Si, O and H, the PECVD only shows Si and H. By adjusting the RBS and ERDA spectrum, we can extract the atomic composition of the samples. For this calculations the SIMNRA software was used. The atomic percentages calculated are displayed in **table 7.1**.

Table 7.1 Atomic composition obtained by IBA techniques of RF-MS and PECVD a-Si:H samples.

	Silicon	**Oxygen**	**Hydrogen**
RF-MS	52%	31%	17%
PECVD	90%	0%	10%

The atomic composition of both layers shows that although the RF-MS film possesses a higher percentage of hydrogen, it is much more unstable under oxidation. The mentioned film gets significantly oxidized with time even in air, which is just a mild oxidizer. It is worthy to mention that the oxide does not come from the film growth, as XPS performed right after the film deposition, **figure 7.6**, shown a very little oxygen contribution.

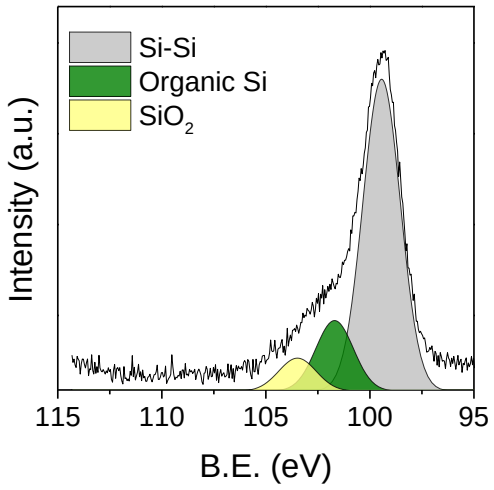

Figure 7.6 XPS spectra of a-Si:H RF-MS sample right after the deposition.

The composition of the RF-MS sample obtained by IBA along with the observations made by FTIR, indicates that the most of the hydrogen is incorporated in the form of polyhydrides, which have several hydrogen atoms per Si atom. This leads to a poor passivation of the Si dangling bonds which results ineffective even under de action of the ambient oxidation, producing an oxygen incorporation not only in the surface of the sample but in the whole volume of the film. Thus, when the sample is introduced in a much more reactive media, as the HF/H_2O_2 solution, the oxidation/oxide removal eliminates the film way to fast to allow the growth of the SiNWs.

On the other hand, the PECVD film have shown a very good agreement on the c_H obtained by the two techniques used. The homogeneous distribution of monohydride bonds has demonstrated to passivate effectively the material, not leading to the incorporation of oxygen to the film even after several weeks of storing. Moreover, it has allowed the obtainment of a-SiNWs by a highly oxidizing method, the MACE.

On the basis of the above exposed, the PECVD, on the described conditions, has proven to be the ideal technique for the growth of a-Si:H films for its application in MACE processes. In further experiments only those films will be used as growth material.

The next step on the growth control of the a-SiNWs, was the adjustment of the etching times on the HF/H_2O_2 solutions. As it has been previously highlighted, in a-Si:H/Cu the etching step is especially crucial, even a small excess of time could lead to the peeling off of the whole deposited material. Thus, a study on the etching rate was performed. Results displayed in **figure 7.7** show an etching rate of 12 nm per second at ambient temperature conditions (~20ºC). As predicted, the etching rate obtained in the a-Si:H films was considerably higher than the one obtained in c-Si, which shown a 10 nm/s rate at 30ºC.

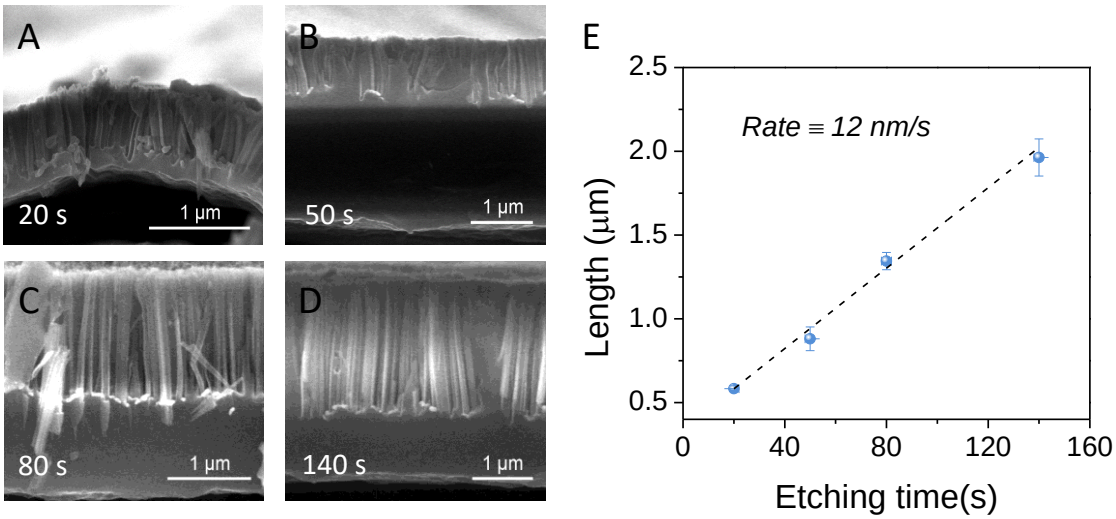

Figure 7.7 A) to D) cross-section FESEM images of a-SiNW on Cu after displayed etching times. E) summarized results of FESEM images and linear fitting of the experimental data.

Summarizing, in this section, the experimental parameters of the MACE process has been adjusted for the obtainment of SiNWs on deposited a-Si:H. The starting material (a-Si:H) has been deeply investigated and its requirements for permitting the a-SiNWs growth has been obtained.

7.3.2 Calculation of the active material mass

When the electrochemical properties of a material are evaluated, the active mass plays a crucial role in the analysis. As it has been already seen, the specific capacity of a material is always displayed in terms of mAh/g. However, the use of this units has a drawback, the errors in the active mass calculation highly influence the specific capacity results. Moreover, when the amount of material is very low, the uncertainty of the mass can shift hundreds or even thousands of mAh/g the specific capacity, inducing incorrect results.

In the materials seen in previous chapters, the obtainment of the active material mass has been a straightforward subject. It has been done by directly measuring its weight, as in the case of free-standing electrodes, or by weighting the electrode before and after the material deposition, as for the case of the on-foil electrodes. However, in the a-SiNWs electrodes we cannot take any of these routes. The direct weighting of the material is not possible because it is deposited over Cu substrates. The same way, the electrodes cannot be weighted before and after the growth of the material because the process involve many steps which needs areas much bigger than the electrodes. Specifically, the PECVD and the MACE on the cells need an excess of substrate in order to fit into the holders.

Due to the mentioned difficulties, the a-Si:H and a-SiNWs mass obtainment was done following different indirect routes in order to achieve a good estimation. The study was firstly focused in the obtainment of the a-Si:H layer mass, which acts as base material for the a-SiNWs, then, it was turned to the evaluation of the a-SiNWs mass.

The first route for the a-Si:H mass obtainment was a statistical study of the weight of electrodes composed by Cu foils, with and without a-Si:H on them. The electrodes were cut by laser so the area of all of them was approximately the same. The thicknesses of the layers were obtained from FESEM cross-section images. A total of 40 electrodes were analyzed. The result of this study is displayed in the first entry of **table 7.2**, expressed as a density of

the material. As can be seen in the table, the error for this method is quite high. This comes from the fact that the low weight of the electrodes has associated a considerable measuring error that, when accumulated, grows to a considerable percentage of the magnitude.

In order to improve the precision of the measurement, another route was taken. The deposition area of the a-Si:H layer was augmented to 10x10 cm (the maximum allowed by the PECVD holder) allowing an increase of the total weight of the Si material. The Cu substrates were weighted before and after the deposition, and the thicknesses of the layers were again extracted from the study of FESEM cross-sectional images. The density value of this large area deposits, displayed in **table 7.2**, it is consistent with the previous value. Moreover, the increased amount of material leads to a high reduction of the measurement error, which allows a good precision.

Table 7.2 Density values and their error obtained by various methods.

Method	Density (g/cm3)	Error (g/cm3)
Electrodes weighting	2.2	0.4
Large area deposits	2.22	0.01
Theoretical model[150]	2.193	0.008

Another way to obtain the density of the a-Si:H is through its structural parameters. The a-Si:H has been investigated since more than 50 years, in all this time, many models has been proposed for its structure. Remes *et al.*[151] proposed a model in which the a-Si:H structure was described as a mixture of the a-Si structure with the substitution of some Si atoms by H atoms, with the presence of some vacancies or voids. The definition of vacancies in this model is the absence of one (monovacancies) or two (divacancies) atoms by the influence of local Si-H bonds, and voids are large areas of missing material also produced by H influence.

The model was proposed after the observation that the a-Si:H films presented densities which could not be explained just with the substitution of some Si atoms by H. By FTIR analysis it was proven that the hydrogen incorporation led to the formation of vacancies or voids which could explain the experimental mass deficiencies observed. Remes *et al.* model was afterwards corroborated and extended by Smets *et al* [150], who set a boundary to the validity of this model. They proposed that the mass deficiency is dominated by vacancies when the hydrogen content is lower than the 14%, while upwards that limit is dominated by voids. In the vacancy dominated area, they observed that the density follows the **equation 7.3**[150], where ρ_{a-Si} is the density of the amorphous silicon, ρ_H is the density of hydrogen and δ is the hydrogen incorporation parameter. The δ varies between $^1/_3$ and ¼, depending on the presence of monovacancies or divacancies, however, Smets *et al* found experimentally a good agreement with a δ value of $\delta = 0.33 \pm 0.03$

$$\rho_{a-Si:H} = \rho_{a-Si} - (\delta\rho_{a-Si} - \rho_H)c_H \qquad \textbf{Equation 7.3}$$

The validity of this relation has been proved among the literature[150], being this model one of the most accepted in the subject.

Appling **equation 7.3** to our material, we obtain a density which is displayed in **table 7.2**.

It can be conclude that all methods used to obtain the density have led to a very similar value, which also agrees with the theoretical models and with the literature values[149,152]. Therefore, the value of 2.20 g/cm^3 will be used from now on as the a-Si:H density. It is worthy to say that the use of the density to obtain the active mass is a well-accepted method in literature[143,144].

For the obtainment of the a-SiNWs density, the same methodology used for the a-Si:H layers was tested. A large amount of electrodes, composed just by the Cu foil and others by the a-SiNWs/Cu, were cut by laser and measured in order to extract the a-SiNW density. However,

the obtained mass of the a-SiNWs was in the range (or even higher) of the a-Si:H mass. This effect could be attributed to the extremely low mass difference before and after the MACE, which is close to the weighting error. A similar thing happened when the MACE process was performed on cells with a larger reaction area; the values were not consistent within the measurements, overestimating or underestimating the weight loss. This weighting erratic behavior probably comes from the enormous surface increase due to the growth of the a-SiNWs, which does not allow a proper mass measurement due to the humidity absorption. Moreover, when the MACE were performed on large surfaces, small areas were peel off due to local imperfections. The mentioned defects, despite of being small enough to be avoided when cutting the electrodes, can alter the weight of the whole layer making inaccurate the calculations.

Because of this problem, an alternative route was proposed: the estimation of the material loss through FESEM observations. This method consisted in the observation of the amount of material removed through top-view and cross-section FESEM images. From top-view FESEM images, **figures 7.8A**, **C** and **E**, the top part of the a-SiNWs were extracted and leaving the images as a black and white diagrams, **figures 7.8B**, **D** and **F**. Those diagrams had a white part which correspond to the a-SiNWs and a black part which is the removed material by the MACE. The ratio between the removed and the kept gave us the percentage of remaining material, inset of **figure 7.8B**, **D** and **F**. The statistical study of various samples led to an average of material loss of the 54% with error of ±5%.

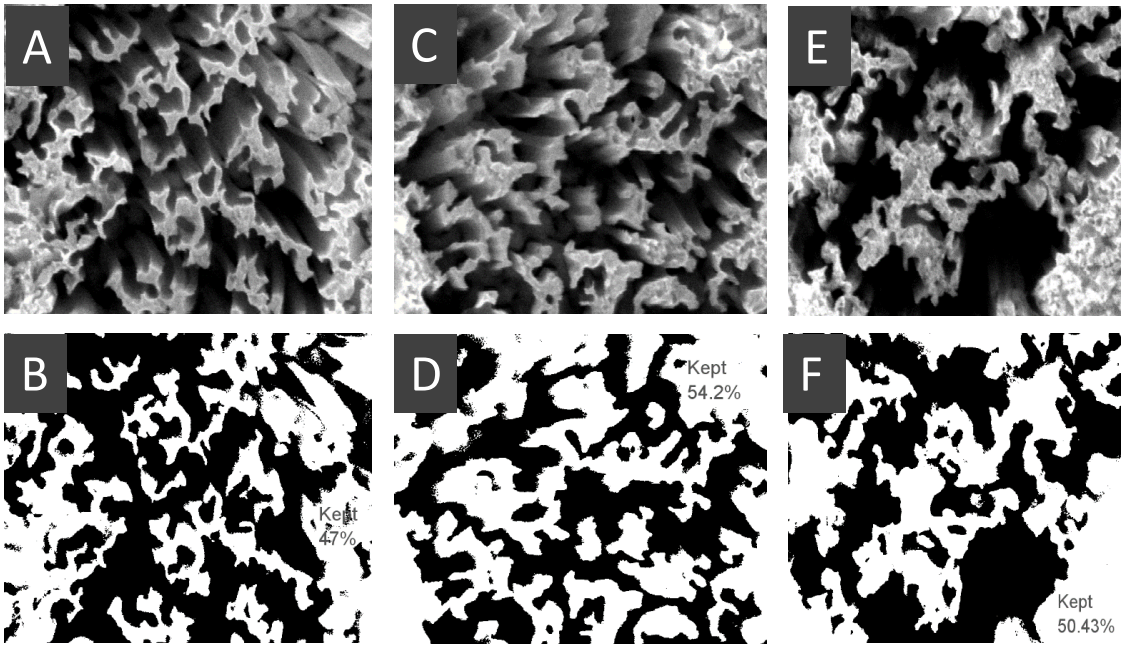

Figure 7.8 a-SiNWs top-view FESEM images (A, C and E) and respective processed images (B, D and F) with the remaining percentage of material labelled.

After the obtainment of the percentage of material removed and the length of the a-SiNWs (by cross-sectional FESEM images) the estimation of the total mass of the a-SiNWs could be made.

7.3.3 Electrochemical performance of the a-SiNWs

Once the mass of the electrodes was properly obtained, the batteries were assembled and their electrochemical performance was obtained by galvanostatic cycling. In order to compare the electrochemical properties of the a-SiNWs with the original material (the a-Si:H film), only a part of the deposited a-Si:H film was transformed to a-SiNWs. This way, the a-Si:H electrodes come from the same deposition as the a-SiNWs electrodes, and have exactly the same composition.

For the electrochemical characterization, the a-Si:H samples had a thickness of 1 μm and a-SiNWs ones had originally the same thickness but, after the MACE, 650 nm were transformed into nanowires.

The electrochemical potential spectroscopy data of this two type of electrodes is displayed in **figure 7.9**. Firstly, it can be appreciated that the a-SiNWs electrode shows a much bigger specific capacity than the a-Si:H film, **figure 7.9A**. From this figure it is observed that the a-Si:H film show for the first cycle a specific capacity around 2800 mAh/g, while the a-SiNWs 4100 mAh/g. It is worthy to mention that, the specific capacity value shown by the a-Si:H film is very similar to the reported capacities of other Si thin films with similar thickness[140,141,143,145]. This similarity with literature results once more corroborate our mass estimations and points out the extraordinary improvement obtained by the growth of the a-SiNWs.

The huge difference in the capacity may be explained by several reasons: shorter diffusion lengths, higher volumetric expansion and less film stress in the a-SiNWs. The high surface-volume structures, such as the SiNWs, have shorter diffusion distances than plane structures due to a higher contact area with the electrolyte[141]. The higher is the surface, the lower is the influence of Si poor ionic conductivity of lithium and slow mass transfer, which usually hinder the electrochemical performance of Si electrodes. The mentioned effect can be appreciated in the DC curves of the a-Si:H films, **figures 7.9B-D**, where is shown a considerable shifting of their cathodic and anodic peaks (compared to a-SiNWs) to lower and higher voltages respectively. Furthermore, the commented over-voltage of the a-Si:H films is even more notable in the inset **figure 7.9C**, showing a sharp peak downwards due to the material poor kinetics. This anomalous behavior is also noticeable in the DC curves in **figure 7.9C** and **figure 7.9D** as a cathodic peak in the positive area. On the contrary, the a-SiNWs does not show any of the mentioned problems, making clear a much faster mass transfer due to the increased area in contact with the electrolyte.

Another likely reason for the increased performance of the a-SiNWs is that the pillar structure is known to allow a higher volumetric expansion capabilities[146]. This structure could

also permit the achievement of a Li richest compound in a similar way that the case of the thick oxide presence against oxide-free surface[121]. The aforementioned is much difficult to state from the EC data, as is usually observed as a displacement of the anodic peaks to lower voltages [153,154]. However, in our data, this can be obscured by the presence of overvoltage in the reference material (the a.Si:H electrodes). Therefore, to approach this possibility, another kind of analysis should be performed.

Lastly, the capacity gain could also come from a lower film stress compared to the starting film[141,155]. The reduction of the stress of the a-SiNWs may be due to the thickness reduction of the film which accompanies its growth. A lower film stress should reduce the fracture that the layer suffers with the cycling, improving the capacity. Indeed, the differences in the film fracture can be noticed in **figure 7.9A**. The capacity of the a-Si:H film after the 2nd cycle increases reaching a maximum in the 7th cycle. On the other hand, the a-SiNW film reach its maximum in the 3th cycle. This interesting effect is related with the cracking of the film. The expansion and shrinkage of the film due to the lithiation/delithiation produces some cracking on the film. After the material achieve an enough crack density, it becomes resistant to further cracking increasing the material activation[141]. The mentioned fact is even more clear in the VP of the a-Si:H film in **figure 7.9E**, where it is seen how the capacity is substantially reduced in the 2nd cycle and is surpassed by the capacity of the 10th cycle. The indicated behavior is also noticeable in **figure 7.9C-D**, as in the 10th cycle more material is activated than in the 2nd one. As mention, the commented effect is largely reduced in the a-SiNW electrode, what indicates a much lower fracturing.

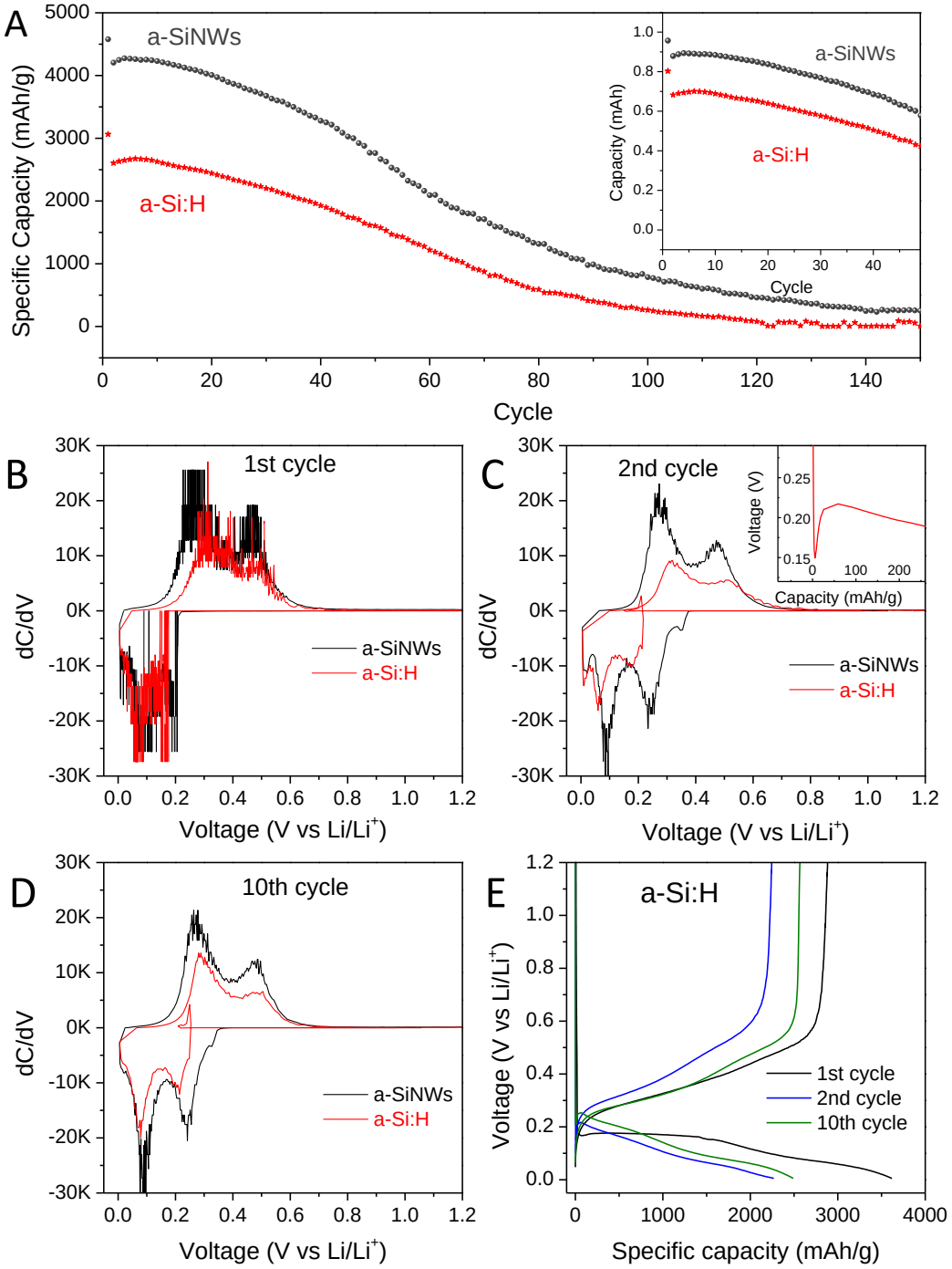

Figure 7.9 A) Graph of the specific capacity as a function of the cycle number for two electrodes: A reference electrode of a-Si:H and an electrode of the same batch but with a-SiNWs grown on it. Inset, the capacity of the same electrodes but without normalizing the capacity by the mass. B)-D) Diferencial capacity curves of the mentioned electrodes of the 1st, 2nd and 10th cycle, respectively. Inset in C) a section of the voltage profile of the lithiation of the 2nd cycle. E) voltage profiles of the a-Si:H electrode for the 1st, 2nd and 10th cycle.

As it has been shown along the chapter, the formation of the a-SiNWs from the a-Si:H entails a material loss and some experimental difficulties. Therefore, the higher specific capacity is not a sufficient reason to opt for the formation of the a-SiNW if the total capacity of the material (regardless of the mass) is lower than the starting material. In order to check if this is our case, in **figure 7.9A** it is displayed the total capacity of the electrodes without the mass normalization. The a-SiNWs shows an important capacity gain, over the 20%, of the total capacity respectively the a-Si:H film. This result is truly interesting, because it means that even with smaller amount of material, the a-SiNWs are capable of activating more material than the pristine a-Si:H film.

The herein exposed makes clear that the growth of the a-SiNWs produces an extraordinary improvement of the electrochemical performance respectively to the starting material. The a-SiNWs allow to overcome many of the problems of the films by: reducing the diffusion distances, allowing a higher volume expansion and reducing the fracturing of the films. Despite of the extremely good results shown, the a-SiNWs still show one of the biggest drawbacks of the a-Si films, the fast capacity fading. In **figure 7.9A** it can be seen how the extraordinary specific capacity of the first cycles gets reduced to ¼ of the original specific capacity after 100 cycles and after 150 cycles the specific capacity has been reduced to only 500 mAh/g. As it has been commented in previous chapters, this is a classical problem of the Si; without an additive that helps him to maintain the integrity of the structure, it slowly degrades due to the shredding produced by the volumes changes. In a-Si films, the overcoming of this problem is rather difficult; the rapid decrease of surface/volume ratio with the increase of thickness reduces the effectiveness of any additive applied in the surface. The aforementioned, force us to keep low thicknesses and, therefore, low mass per electrode. At this point the a-SiNWs are a great response to the problem, their high surface/volume ratio could potentially allow the surfaces additives (CNTs, carbon layers etc.) reach to the majority of the mass, which could increase the electrode cycling performance.

7.4 Conclusions

The first result which can be highlighted from the chapter, is the grow of a-SiNWs from a-Si:H on top of Cu substrates through a MACE process. To our knowledge, this is the first reported work on the growth of a-SiNWs by MACE on a substrate different from the c-Si.

The a-Si:H deposition was done by two techniques (RF-MS and PECVD). However, the a-SiNWs growth was only achieved by PECVD. Along the chapter an extensive analysis has been made to determine the reasons for the unsuccessful growth of a-SiNWs on the RF-MS samples. This study has concluded that the microstructure formation during the deposition and an inefficient hydrogen passivation, are the main causes which prevent the growth of a-SiNWs on RF-MS samples.

Another important achievement of the chapter has been the mass estimation of the a-Si:H and a-SiNWs electrodes. We have applied several routes for this purpose and all of them have shown a very good agreement on the results.

The novel a-Si:H/Cu and a-SiNWs/Cu electrodes has been electrochemically characterized. The results shown an impressive increase of the capacity when the a-SiNWs are grown (20% in neat capacity and 45% in specific capacity). The causes of this capacity increase has been addressed by the analysis of the EC data and it has been attributed to the shorter diffusion lengths, higher volume expansion capabilities and reduced internal strain of the film.

In spite of the fact that the a-SiNWs still show an important capacity fading, the huge increase of surface could permit the application of carbon based materials which could boost their cycling performance. This topic is currently under research and future work will be done in this direction.

Chapter 8:

Stability of Titanium Carbides (MXenes)

8.1 Introduction

The present chapter focuses on the oxidation stability of MXenes, an emerging class of 2D materials which has found extensive applications in electrochemical energy storage[50,51,156], FETs,[157]electromagnetic shielding[158] and many others. Moreover, they can be subjected to liquid exfoliation[159] for large-scale synthesis, which makes them very interesting for industry level applications. In this chapter are studied the most commonly used MXenes: the $Ti_3C_2T_x$ and Ti_2CT_x. Their good conductive properties,[160] as well as their outstanding electrochemical performance,[50,156] render them the ideal candidates not only for stand-alone electrodes but also as additives for the formation of hybrid electrodes. This is the focal point on the study of this material, its application into the LIBs along with the SiNWs. Nevertheless, before considering the formation of SiNWs/MXene hybrid electrodes, there is an important subject to overcome in this novelty materials: their stability. Previous studies found that the $Ti_3C_2T_x$ degrade either in humid air[157] or water[161], and this degradation is even faster in the Ti_2CT_x.[48] This could be a serious obstacle in their application and makes absolutely necessary the comprehension of the degradation process, as well as the development of protocols to

prevent it. In the literature there is no such reports, therefore, this will be the aim of this chapter: a comprehensive study of the degradation mechanisms of the MXenes, the factors which influence it and the ways to suppress it.

8.2 Experimental

The obtainment of the MXene colloidal solution was achieved by two subsequent processes: the etching of the MAX phase to obtain multi-layered MXenes and its delamination to produce a mono-layered (or few-layered) MXene colloidal solution.

8.2.1 Preparation of multilayered MXenes

The multilayered (m-) $Ti_3C_2T_x$ or Ti_2CT_x powders were prepared by acidic etching of corresponding MAX phases according to the literature[50]. Firstly, 1 g of LiF (Sigma Aldrich, USA) was added to 10 ml of 9 M HCl solution (30 wt.%, USA). After 0.5 h of stirring, 1 g of Ti_3AlC_2 was slowly added to the acidic solution. Then the mixture was transferred to an oil bath where it reacted for 24 h at 35 ºC under stirring. After that, the etched material was washed with deionized (DI) water and centrifuged several times until the pH of the supernatant reached 6. Finally, the dispersion was filtrated through a Celgard membrane (Celgard 3501, PP coated, USA) and then, the as-obtained cake was dried in a desiccator for a whole night. The m-Ti_2CT_x was similarly prepared except using the Ti_2AlC MAX phase.

8.2.2 Delamination of multilayered MXenes

The delamination of m-$Ti_3C_2T_x$ and m-Ti_2CT_x was conducted in the same way. Typically, 200 mg of dried m-$Ti_3C_2T_x$ cake was added to 50 ml of water and was vigorously stirred for 1 h to ensure complete re-dispersion. The solution was degassed for 10 min in a pulsed sonication bath while bubbling with Ar. After that, the dispersion was continuously sonicated for 1 h under Ar bubbling. During sonication, the temperature was held at 20 °C while the

frequency was set to 37 kHz and the power amplitude to 60%. Afterwards, the dispersion was centrifuged at 3500 rpm for 1 h to separate the delaminated flakes from the unexfoliated particles, and labelled "standard delaminated $Ti_3C_2T_x$ (d-$Ti_3C_2T_x$)". The sediments were recycled and the above process (sonication and centrifugation) was repeated to obtain a sufficient quantity of colloidal solution. The supernatant was injected into normal glass bottles, sealed with parafilm and stored in a room temperature environment. This environment was denoted as "Air@RT". We also stored the d-$Ti_3C_2T_x$ colloidal solution in the fridge (5 °C), a low temperature environment (Air@LT). To further improve the stability of the MXene flakes, the fresh d-$Ti_3C_2T_x$ colloidal solutions were hermetically sealed within Ar-filled bottles immediately, which were then stored at room temperature (Ar@RT) and in the fridge (Ar@LT). Delaminated Ti_2CT_x (d-Ti_2CT_x) colloidal solution was similarly prepared and stored in the Air@RT and Ar@LT environments.

8.2.3 Size selection of d-$Ti_3C_2T_x$ flakes

In order to obtain colloidal MXene dispersions with different lateral flake sizes, a liquid cascade centrifugation technique[162] was performed. This process was made right after the sonication described in the delamination. The as-sonicated $Ti_3C_2T_x$ solution was first centrifuged at 1000 rpm (134 g) for 1 h. The sediments, containing unexfoliated/ restacked MXene or incompletely etched MAX, were discarded. The supernatant, which contained flakes with a wide range of sizes, was subjected to a second centrifugation at 2500 rpm (837 g) for 1 h. The sediments, obtained in the speed range "1000-2500 rpm", were collected and re-dispersed to form a colloidal solution *via* vigorous shaking for 5 min. This sample was denoted as "large". The supernatant was continuously centrifuged at increasing speeds while the sediments between the two centrifugation speeds were collected and re-dispersed, namely 2500-4000 rpm (2144 g, "medium large"), 4000-5500 rpm (3320 g, "medium") and 5500-

7000 rpm (5379 g, "medium small"). The final supernatant was gathered and named as "small". A scheme of the process in displayed in **scheme 8.1**.

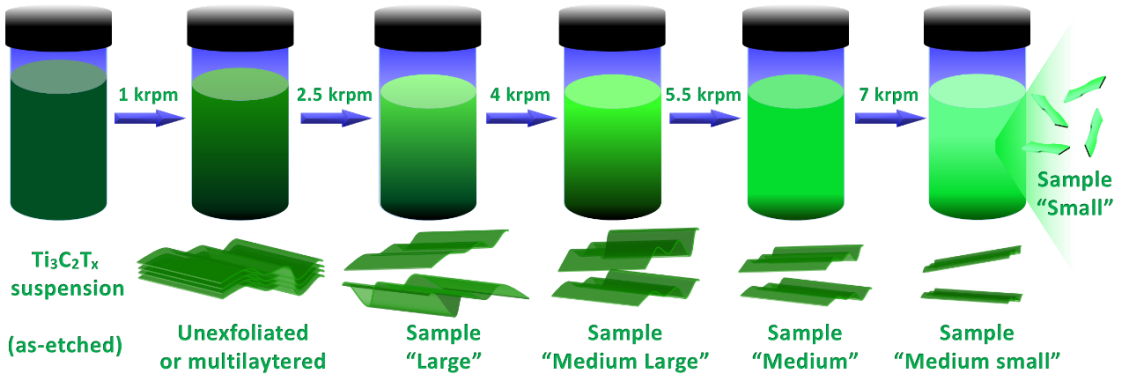

Scheme 8.1 Diagram of the size selection process.

8.3 Results and discussion

8.3.1 Stability of standard samples at Air@RT

For most applications, $Ti_3C_2T_x$ MXene aqueous dispersions are stored at room temperature (23 °C, Air@RT) [53,163] with no further protection. These parameters were the starting conditions of the MXene stability studies. By electron microscopy analysis, it was observed that the standard as-synthetized $Ti_3C_2T_x$ flakes, **figure 8.1A** and **figure 8.1G**, shows a clean surface and edges. Moreover, high-resolution TEM revealed clear lattice fringes, **figure 8.1D**, suggesting the nanosheets are single-crystalline. SAED pattern, inset of **figure 8.1D**, shows a hexagonal atomic arrangement, which is coherent with previous reports on $Ti_3C_2T_x$ MXenes.[48,55]

After aging in Air@RT for 1 week, at the edges of the sheets, some "branches", up to 100 nm in size, are formed, **figure 8.1B**. However, in the basal planes, only small nanoparticles of 2-3 nm in size are observed. Analyzing by fast-Fourier transform (FFT) the latter of the branches and nanoparticles formed, it was obtained a clear pattern which match with TiO_2

anatase (inset of **figure 8.1E**). Moreover, the SEM images in **figure 8.1H,** also showed contrast differences between edge and basal plane sites. These much brighter areas on the edge are symptomatic of change in composition of the material, which match with the formation of anatase TiO_2 observed by TEM.

Further aging in Air@RT for 30 days resulted in the complete degradation of the sheets, only being able to find anatase debris and disordered carbon, shown in **figure 8.1C**, **F** and **I**. Despite **figure 8.1F** still shows some sheets, both the edges and basal planes shows an extreme charge effect and blurry edges, being significant of a high degradation stage and anatase presence. The color of the dispersion also evolved from dark green to cloudy-white during the aging process (inset of **figures 8.1G**, **H** and **I**). The observations performed by electron microscopy analysis, suggests that the degradation process is faster on the edges, while the basal planes seems to be more resilient to the process. Therefore, during the aging, the "branches" grow from the edge sites to the basal plane, shredding the nanosheets into small particles (debris).

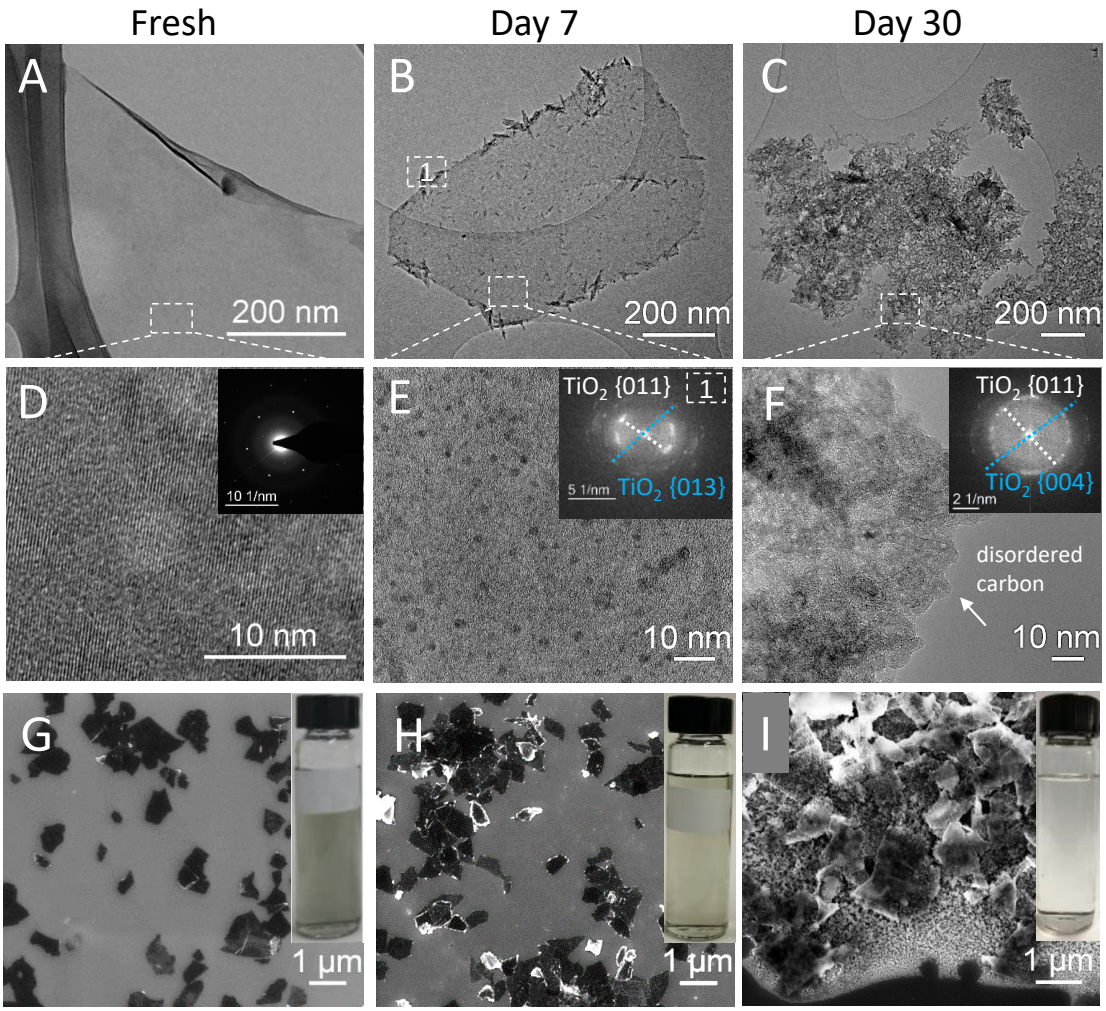

Figure 8.1 TEM images of (A) fresh d-$Ti_3C_2T_x$ solution and aged solutions in Air@RT for (B) 7 days and (C) 30 days, respectively. (D-F) are high resolution TEM images in (A-C), respectively. Inset in (D) is the corresponding SAED pattern and in (E-F) are the corresponding FFT patterns. SEM images of flakes from the fresh standard solution (G) after aging in Air@RT for (H) 7 days and (I) 30 days. Insets in (G-I) shows that the color of the standard solution changes over time.

To further confirm the composition of MXene solution after different periods of degradation, Raman analysis was performed. The fresh sample, **figure 8.2A**, showed the expected vibrational modes for $Ti_3C_2T_x$ MXene.[33] After aging the MXene solution in Air@RT for 14 days, the $Ti_3C_2T_x$ vibrational modes fully disappear, only being possible to detect anatase and disordered carbon peaks, **figure 8.2A** and **B**. When the exposure to Air@RT is increased to 60 days, the anatase signal intensify, being able to identify more of the vibrational modes of the anatase.[33]

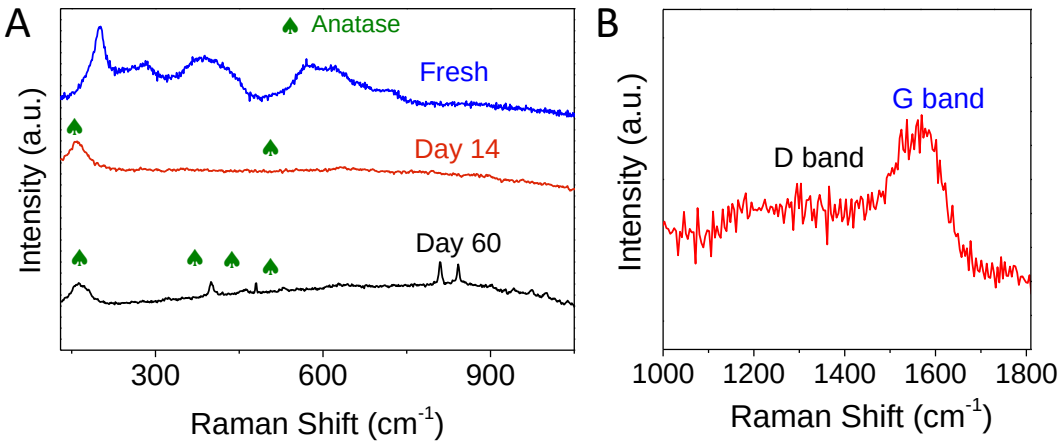

Figure 8.2 Raman spectra of fresh as well as aged MXene films for different durations A) and zoomed area of the carbon signal for the 14 days aged sample.

The evolution of the surface of the $Ti_3C_2T_x$ flakes was further monitored by XPS. **Figure 8.3A** shows the high-resolution XPS of the fresh MXene film in the Ti 2p region. In this spectrum it is observed the typical $Ti_3C_2T_x$ MXene signal, with a pair of asymmetric peaks corresponding to a Ti-C bond (formation of Ti Carbide) at a binding energy of 455 eV, two sets of symmetric peaks indexed to Ti (II) (~456 eV) and Ti (III) (~458 eV) which can be attributed to the presence of sub-oxide and/or hydroxide, and Ti (IV) oxide (TiO_2) (~ 459 eV). [164] After 10 days in Air@RT, the shape of the spectra significantly changes. Its deconvolution shows that the Ti (IV) oxide peak increases substantially while the carbide peak intensity gets reduced, **figure 8.3B**. After the MXene colloidal solution was aged in Air@RT for 25 days, no carbide signal was detected and the remaining signal was attributed to 5% Ti (III) sub-oxide and 95% TiO_2, **figure 8.3C**.

The evolution of the XPS spectra to TiO_2 clearly matches with the Raman and electron microscopy observations, which shows a similar degradation rate. In addition, the presence of Ti (II) and (III) sub-oxides and/or hydroxides in the initial 10 days, **figure 8.3C**, and their substantial concentration decrease after 25 days, suggest that the Ti (II, III) hydroxides

and/or oxides, are intermediate phases in the degradation of $Ti_3C_2T_x$ into anatase TiO_2. This oxidation phenomenon is also found in monolayered or multilayered MXene that are exposed to air[45] or water.[161]

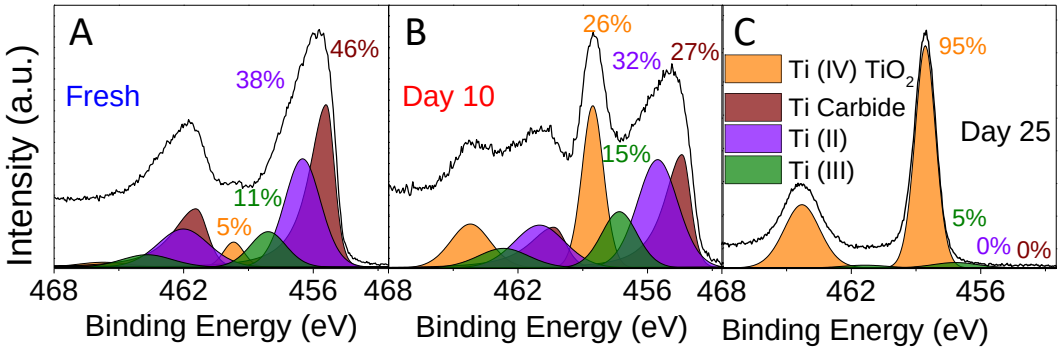

Figure 8.3 XPS results of fresh d-$Ti_3C_2T_x$ film (A) and film that was aged in Air@RT for 10 days (B) and for 25 days (C).

In order to quantify the degradation phenomenon and track it with a higher periodicity, UV-Vis measurements of the solution were performed. The extinction spectra of a selected sample, for the displayed days aging in Air@RT, is shown in **figure 8.4A**. In this figure it can be seen the clear evolution of the fresh d-$Ti_3C_2T_x$ spectrum to the typical TiO_2 spectrum[165], with a continuous decay of the $Ti_3C_2T_x$ features. The intensity at 785 nm was chosen as the metric for the concentration of the MXene nanosheets. Its normalized intensity plotted as a function of time can allows us to track the degradation of the colloidal solution similarly as it has been done for other 2D materials[166]. The 785 nm peak was selected to normalization due to its consistent decrease of intensity with the aging of the material, being a feature away enough from the TiO_2 exciton at 300 nm to not be affected by it.

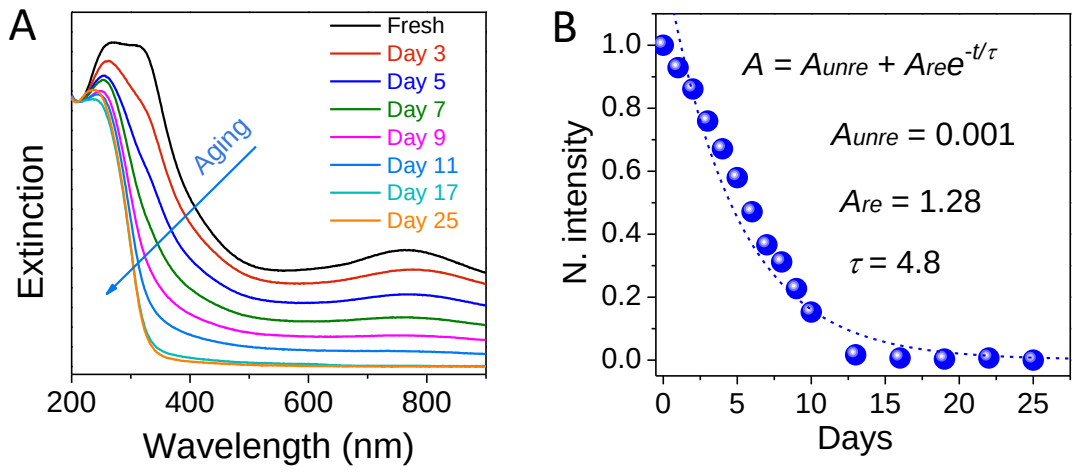

Figure 8.4 UV-Vis extinction spectra of the standard d-$Ti_3C_2T_x$ MXene solution aged in Air-RT for different durations A) and experimental data and fitting of the normalized intensity of the 785 nm peak as a function of time B).

The evolution of the normalized intensity, **figure 8.4B**, was fitted to an empirical function,[166] **equation 8.1**, where A_{unre} are the stable/unreactive nanosheets, A_{re} the reactive/unstable ones, and τ is the time constant (days).

$$A = A_{unre} + A_{re} e^{-t/\tau} \qquad \textbf{Equation 8.1}$$

It is quite remarkable that the MXene nanosheets follow very accurately an exponential decay with a time constant of only 4.8 days. Furthermore, if the proportion of reactive material, $A_{re}/(A_{unre} + A_{re})$, is calculated, a value of 99.92% is obtained, indicating that all the MXene nanosheets are vulnerable to degradation.

The observed exponential decay is similar to the degradation behavior of aqueous solutions of black phosphorous, which showed a comparable time constant of 7.9 days.[166] These results show that after 10 days the amount of $Ti_3C_2T_x$ has been reduced almost to an 80% of their initial proportion, and after 15 days the MXene signal is not appreciable, what is in a very good agreement with the Raman and XPS observations.

8.3.2 Influence of ambient conditions in stability

Based on above results, it is clear that d-$Ti_3C_2T_x$ MXene aqueous solutions are unstable in Air@RT environments. Moreover, the obtained degradation rate is too high to ensure the performance of the MXenes in various applications and makes necessary to develop ways for improving the lifetime of the aqueous solution. This subject was approached by two ways: introducing the aqueous solution into an oxygen-free environment and lowering the temperature to reduce the oxidation rate. The use of these methods could not only allow the finding of the most appropriate way to preserve the solution, but could also help the better understanding of the oxidation process. If in the oxygen-free environment the degradation rate does not improve, clearly the water is the main oxidizer agent of the d-$Ti_3C_2T_x$. In the opposite case, the oxygen is the main oxidizer one.

The oxygen-free environment was achieved by introducing the d-$Ti_3C_2T_x$ aqueous solution into Ar-filled bottles, which were pre-assembled inside the glove box at a pressure of 2.3 bar. The compressed Ar could effectively prevent the air from entering the water medium and forming dissolved oxygen. Moreover, the multilayered $Ti_3C_2T_x$ suspension was degassed prior to and during bath sonication, to remove the dissolved oxygen from the fresh d-$Ti_3C_2T_x$ aqueous solution. Consequently, the solution stored in Ar-filled bottles was well protected from the dissolved oxygen. Lowering the temperature could also improve the lifespan of the d-$Ti_3C_2T_x$ aqueous solution by reducing the oxidation rate as Arrhenius equation predicts.[167] The usefulness of these methods were tested and the stability of MXene aqueous solutions in different environments, named Air@LT, Ar@RT and Ar@LT are compared with Air@RT in **figure 8.5A**. In this figure it can be seen how the stability was remarkably improved by introducing a lower temperature and/or Ar environment. After 25 days, the concentration of the Air@LT sample was only reduced to the 57% of the initial, in sharp

contrast of 86% and 95% of the Ar@RT and Ar@LT respectively. In all cases, the lifespan was substantially increased when compared with the Air@RT.

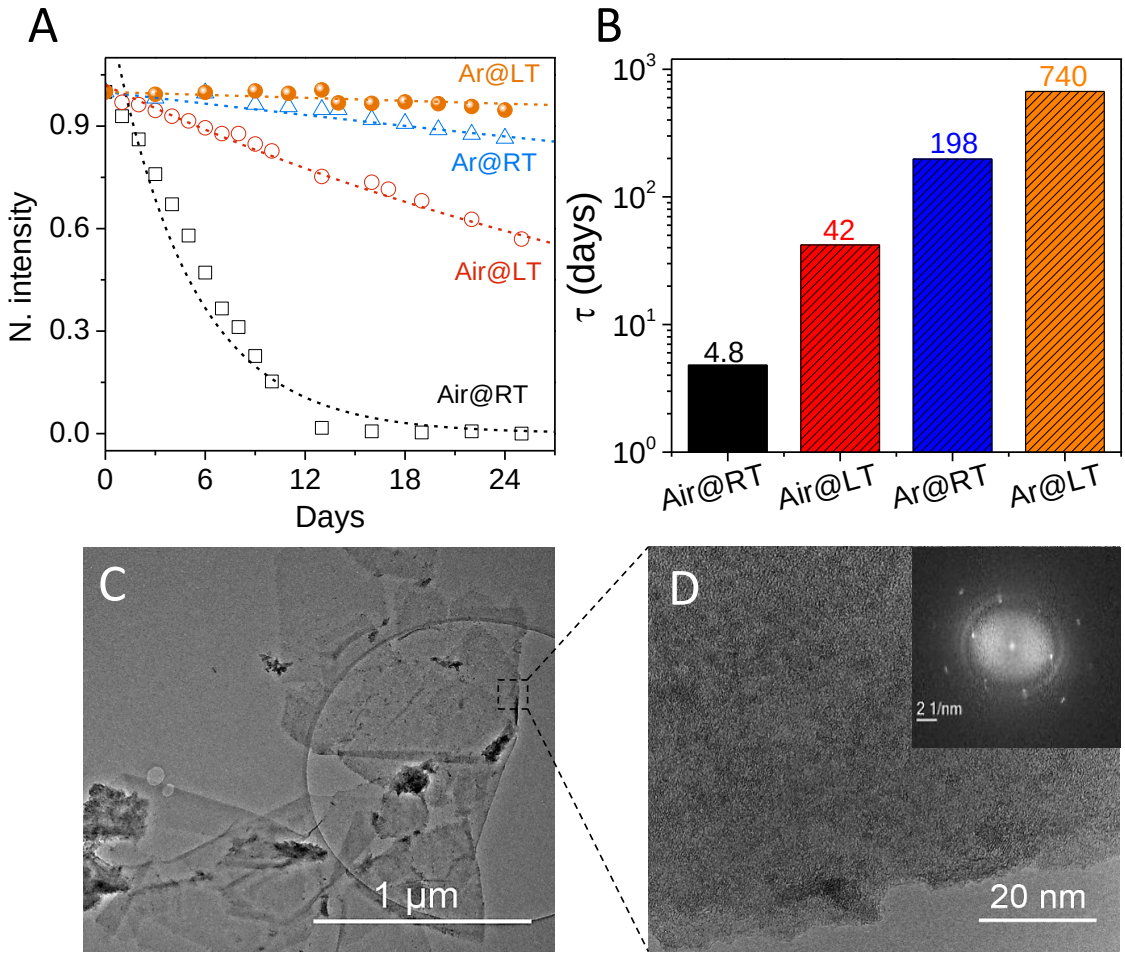

Figure 8.5 Stability of colloidal d-$Ti_3C_2T_x$ in different environments A). The dotted lines are the fitting results according to the empirical equation $A = A_{unre} + A_{re}e^{-t/\tau}$. Time constants of colloidal d-$Ti_3C_2T_x$ in different environments, B). Low, C), and high, D), magnification TEM images of aged d-$Ti_3C_2T_x$ flakes in Ar@LT for 14 days. Inset in D) is the corresponding FFT pattern.

The improved stability of Ar-stored samples, compared to the Air-stored ones, suggests that the removal of the dissolved oxygen from the colloidal solutions is considerably more effective than merely lowering the temperature of the solution. The aforementioned highlights the dissolved oxygen as major oxidant of the $Ti_3C_2T_x$, while the aqueous medium is just a mild one. This observation was further supported by fitting the degradation results with the exponential decay model. The time constants, shown in **figure 8.5A-B**, exhibited

an improvement of almost an order of magnitude when the MXene solution were stored at LT (from 4.8 to 42 days), and were further increased to 198 and 740 days (about two years) in Ar@RT and Ar@LT, respectively. The above results show that the Ar@LT is the best environment for storing MXene colloidal solutions. This point was further supported by the Raman (not shown), XPS (not shown) and electron microscopy, **figure 8.5C-D**. In these TEM images, it can be seen that the MXene flakes stored in Ar@LT for 1 month still show a relatively clean and even surface, despite of the presence of some "branches" at edges. The higher magnification TEM image in **figure 8.5D** shows no anatase nanopaticles, in sharp contrast with the observed in Air@RT samples. Moreover, the FFT in the inset of the figure, also indicates a well-kept crystallinity of the $Ti_3C_2T_x$ in the Ar@LT sample.

8.3.3 Influence of flake size on stability

From the analysis of the electron microscopy images, it was stated that the degradation at the edges was considerably faster than in basal planes. These result indicates that flake size could potentially be a critical factor in the stability of the MXene solution. Due to the fact that smaller flakes have a bigger perimeter to surface area, they could degrade much faster than bigger flakes. To check and quantify this assumption, it was investigated the influence of the size of the flakes into the kinetics of the degradation. Instead of using the standard d-$Ti_3C_2T_x$ solution, that has a broad size distribution[168], we performed a size selection of the colloidal solution *via* a cascade method.[162,169] From the five ranges of sizes obtained from the cascade centrifugation, three representatives were chosen, namely, large, medium and small flake samples, in order to have wider size differences. **Figure 8.6A-C** show the SEM images of size-selected flakes, indicating smaller flakes were obtained as the centrifugation speed was increased. Histograms of the lateral size of the flakes, which were performed through SEM image analysis, **figure 8.6D-F**, further confirm the size reduction with the increasing centrifugation speed.

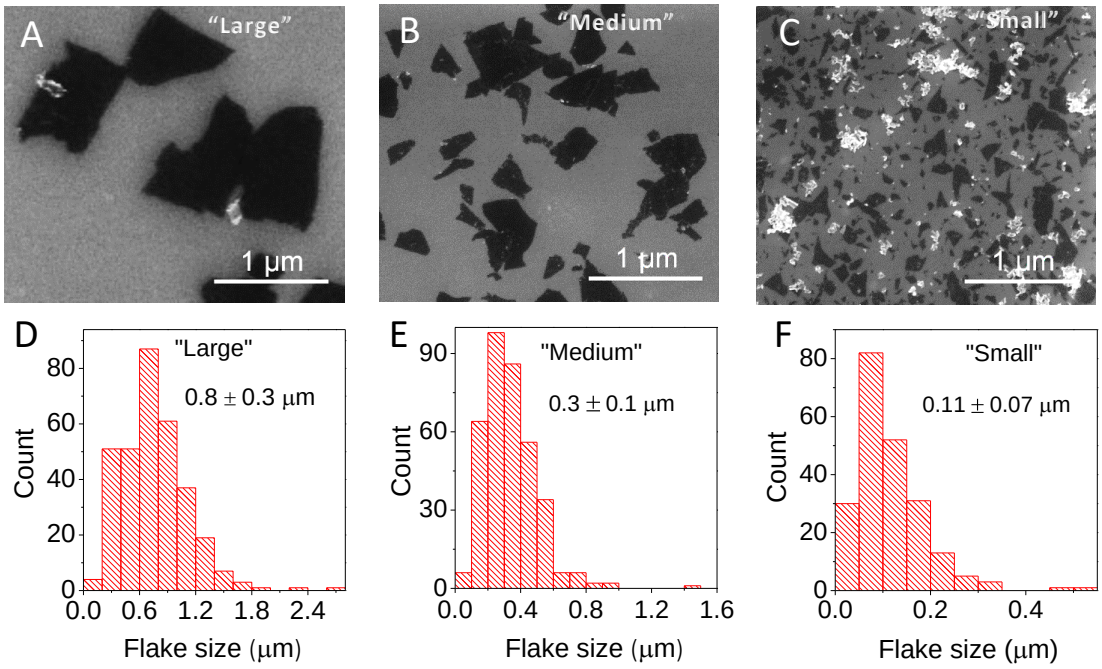

Figure 8.6 SEM images of size selected samples ranging from the largest size on the left to the smallest size on the right, A) to C). D) to F) corresponding lateral flake size histograms of A) to C).

To quantify the degradation rate of the different sized samples, the stability was obtained through the normalized extinction spectra. The stability of colloidal solutions with various sizes, shown in **figures 8.7A-D**, suggested that large MXene flakes are the most stable, followed by the medium and small ones. This fact is appreciable in all the ambient conditions, making clear that the degradation process is an edge-driven reaction. Moreover, the stability results again highlight a huge lifespan increase of the dispersions by introducing them into Ar and LT conditions. The lower stability of smaller flakes could also be confirmed by TEM, as shown in **figure 8.7E-F**, where it can be observed a much advanced degradation stage in the smaller flake.

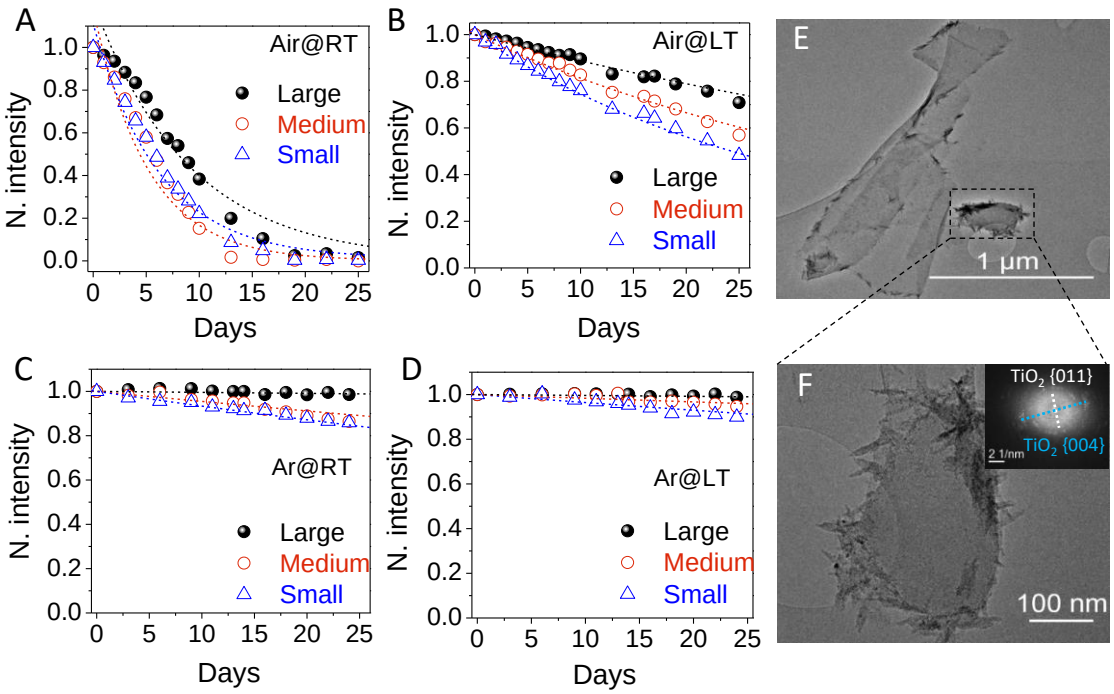

Figure 8.7 Stability results of small, medium and large d-$Ti_3C_2T_x$ flakes in Air@RT, Air@LT, Ar@RT and Ar@LT, A) to D) respectively. The dotted lines are the fitting results according to the empirical equation, $A = A_{unre} + A_{re}e^{-t/\tau}$.

From the normalized intensity of the extinction spectra, it was further estimated the time constants (τ) of colloidal solutions with varying flake sizes by fitting the data points in **figure 8.7A-D**. Once again, the exponential decay model explains the degradation behavior of the dispersions quite well, regardless of flake size. The τ of the different sized samples in the tested environments are summarized in **Table 8.1**. Here, it can be seen how the lifespan of the large flakes is considerable higher than the smaller ones in every case. This result is also observed when comparing the medium and small sizes, where only in the Air@RT a reverse behavior is observed due to the proximity of the results.

Table 8.1 Time constants of different sizes in different environments

Size	Time constant (τ) (days)			
	Air@RT	**Air@LT**	**Ar@RT**	**Ar@LT**
Large	9	75	2100	2400
Medium	5.1	43	205	555
Small	6.2	30	138	255

Very interestingly, the τ of the standard d-$Ti_3C_2T_x$ sample in Ar@LT was 740 days, a value between that of the small flake sample and the large flake one, indicating that the instability of smaller flakes is the main cause for the short lifetime of the standard MXene dispersion. The aforementioned conclusion can be also extended to the other environments, where similar results are observed.

To gain more insights into the size effect, the τ as a function of flake size, **figure 8.8**, was fitted using the **equation 8.2**[166], where "a" and "b" are coefficients, and "L" is the mean flake size (nm).

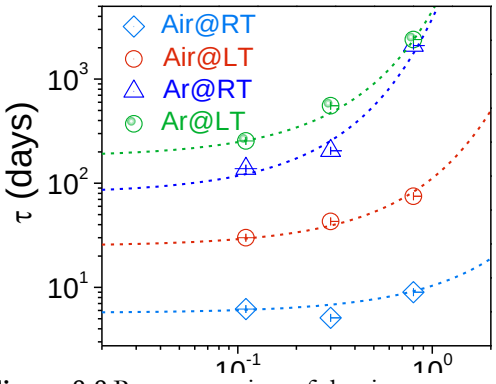

Figure 8.8 Representation of the time constant extracted from the fitting of graphs of figure 8.7 as a function of flake length. The dotted lines are the fitted results according to the empirical equation, $\tau = a*10^{bL}$.

$$\tau = a*10^{bL} \qquad \textbf{Equation 8.2}$$

In this figure, the correlation between flake size and τ for each environment can be clearly seen. In addition, the fitting parameters and correlations are listed in **table 8.2**. These correlations are extremely important and useful, because it allows a fast

knowledge of the mean size of the MXene flakes *in-situ* from the UV-Vis spectra, without requiring electron microscopy or other size measurements and *vice versa*.

Table 8.2 Fitting parameters and correlations for listed environments

Sample	Metrics
Air@RT	$\tau = 5.7*10^{0.00026L}$
Air@LT	$\tau = 25*10^{0.0006L}$
Ar@RT	$\tau = 80*10^{0.00168L}$
Ar@LT	$\tau = 180*10^{0.0014L}$

Based on the above discussion, the large flake dispersion stored it in Ar@LT environment, would be the ideal conditions to store MXene aqueous solutions. In these conditions, the solution is extremely stable, only degrading a 1.2% over 25 days. The fact that the $Ti_3C_2T_x$ MXene dispersion still degrades in absence of oxygen can be attributed to the water medium, a mild oxidant for MXenes. Therefore, if the flakes are separated from water the degradation should be fully avoided.

8.3.4 Preserve of the MXenes in absence of water

To remove the water from the MXene solutions, they were subjected to a vacuum filtration process, obtaining compact films of stacked flakes, **figure 8.9 A-C**. After the filtration, the material was introduced into a desiccator for 24 h in order to get rid of any water remains. To check if the material still oxidizes, a film produced from as-obtained material and a filtrated film aged 30 days in Air@RT (aged after filtration) were analyzed by Raman, **figure 8.9D**. The Raman spectra show no difference between the films and a total absence of anatase signal, meaning that the flakes are well preserved when they are separated from water. This result is understandable, as the compact morphology, **figure 8.9C**, prevents the inner nanosheets from interacting with humid air, preserving the majority of the material unoxidized. This conservation method would be useless if the filtrated material would not be able to be redispersed again. However, just by a simple magnetically stirring in water or manual shaking, it quickly re-disperse and form a colloidal solution, **figure 8.9E**,

demonstrating excellent reversibility. This result is very important, as it allows us to keep the quality of MXene high, even for prolonged periods of time in Air@RT.

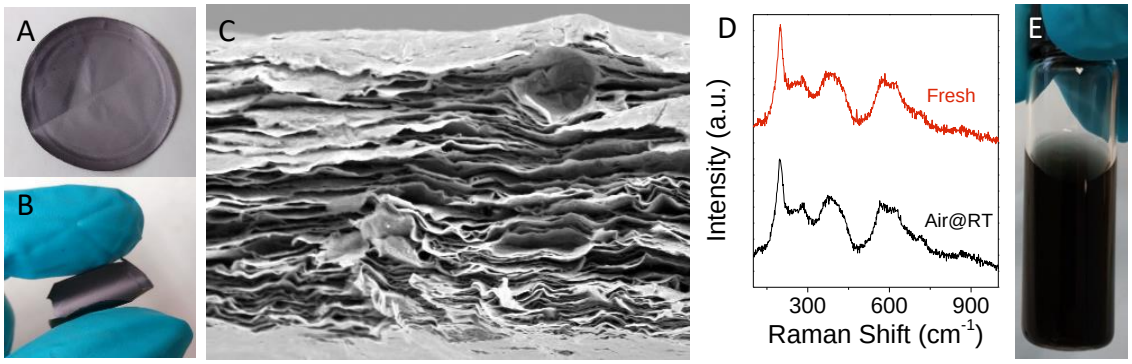

Figure 8.9 Filtrated MXene film A)-B). Cross sectional SEM image of a MXene filtrated film from colloidal solution, C). Raman spectra of fresh as-produced MXenes and filtrated film after 30 days in Air@RT conditions, D). Redispersed MXene film in water by manual shaking, E).

The degradation process of the $Ti_3C_2T_x$ MXene can be summarized as follows: (1) In Air environments, there is presence of dissolved oxygen and water, which both act as oxidizers of the flakes. The formers react more actively in the edges, leading to the formation of anatase (TiO_2) and degrading the material. Small size flakes and/or storing the dispersion at RT contributes to the acceleration of the flakes degradation. This process is schematically illustrated in **scheme 8.2A**. (2) Through elimination of dissolved oxygen from water via storing the material in compressed Ar vials, the degradation phenomenon is substantially suppressed, reaching time constants of several years. Even so, the flakes still degrade slowly over time, **scheme 8.2B**. (3) If the flakes are separated from water *via* vacuum-assisted filtration, the degradation is effectively suppressed being regardless of the environment, **scheme 8.3C**.

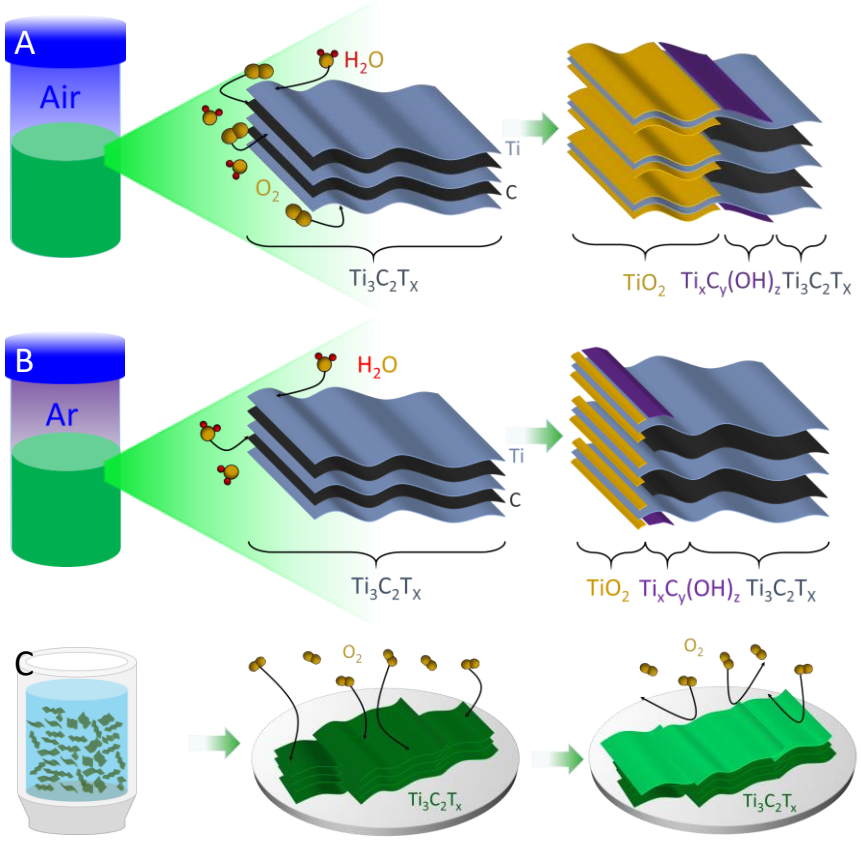

Scheme 8.2 Schematics of degradation of the colloidal d-$Ti_3C_2T_x$ MXene aqueous solution in Air@RT A), Ar@RT B), and the filtrated film under Air@RT, C). In A), the high solubility of oxygen in water provides a continuous source for MXene degradation. In B), in the absence of dissolved oxygen, water (a mild oxidant) slowly degrades the MXene flakes in the Ar-based environment. In C), the outer flakes and the compact nature of the film prevents the oxidation of the majority of the material.

8.3.5 Extension of the results to other MXenes

Another popular MXene which could get really benefited from an increase of the lifespan is the Ti_2CT_x. This material has very promising electrochemical performance as a battery and supercapacitor electrode.[156,170] However, its high degradation rate[48,171], which could be attributed to the fact that MXenes, $M_{n+1}X_n$, becomes more stable as n increases from 1 to 3[51], could potentially hinder its application. For this reason, it is a perfect candidate to test if the above described degradation process can be applied for all MXenes, and, consequently, the investigated protocols to extent their lifetime.

The as-delaminated (d-) Ti_2CT_x MXene colloidal solution, has a pink color, **figure 8.10A**, and consists of ultrathin, electron-transparent nanosheets, **figure 8.10B**. In order to check

its stability under common ambient conditions, the d-Ti_2CT_x dispersion was stored in Air@RT. Its extinction spectra were obtained similarly as in $Ti_3C_2T_x$, and the normalized intensity was extracted at wavelengths of 520 nm. The normalized intensity as a function of aging time can be seen in **figure 8.10C**. In contrast with the $Ti_3C_2T_x$, the Ti_2CT_x degraded in hours instead of days. Almost a 50% of d-Ti_2CT_x concentration decayed after aging in Air@RT for 8 h, and it was completely gone after 24 h, as shown in **figure 8.10C**. As the $Ti_3C_2T_x$, the degradation of d-Ti_2CT_x flakes also follows an exponential decay. Fitting the data, a time constant (τ) of 0.4 days (10 h) is obtained. This is quite believable, as the solution became cloudy-white after aging the solution in Air@RT for 12 h **figure 8.10D**. TEM images of the flakes after 12 h in Air@RT further confirmed an advanced stage of degradation, showing numerous "branches" and nanoparticles, which were confirmed to be anatase, **figure 8.10E**.

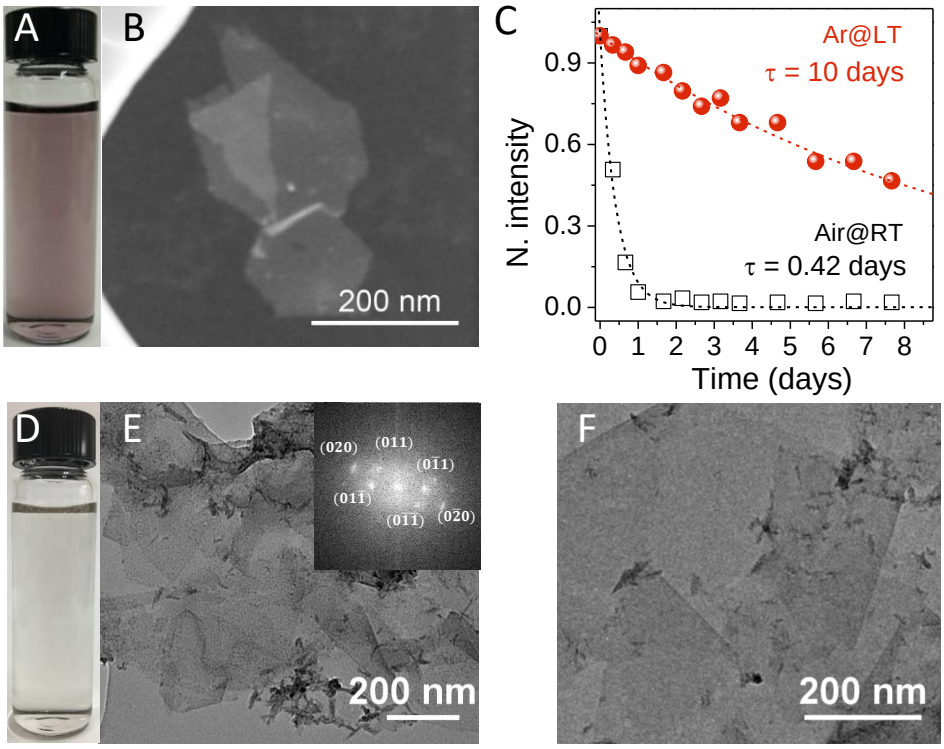

Figure 8.10 Optical image of fresh d-Ti_2CT_x MXene solution, A) and aged solution for 1 day in Air@RT, D). SEM image of fresh MXene flake, B). Stability of d-Ti_2CT_x in Air@RT and Ar@LT,

C). The dotted lines are the fitting results according to the empirical equation $A = A_{unre} + A_{re}e^{-t/\tau}$. TEM image of d-$Ti_2CT_x$ stored in Air@RT for 12 h, E) and in Ar@LT for 12 h, F).

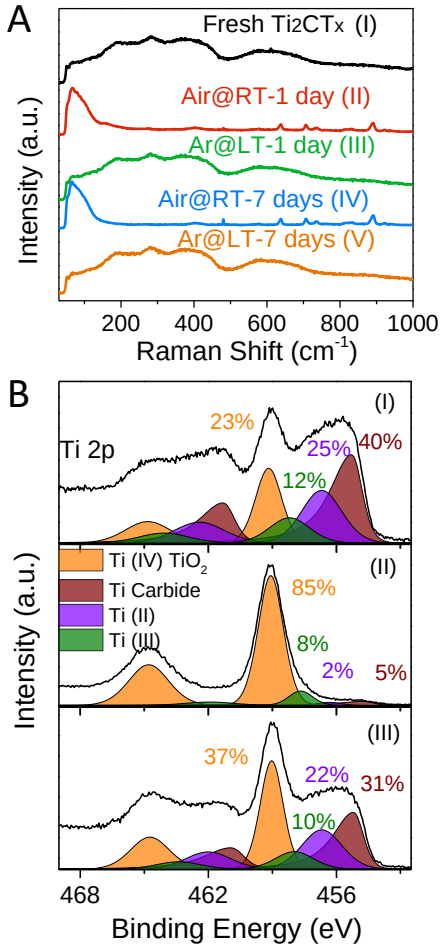

Figure 8.11 Raman spectra of fresh, Air@RT and Ar@RT samples after the displayed aging times, A). XPS spectra of fresh Ti_2CT_x (I), aged for 1 day in Air@RT (II) and aged for 1 day in Ar@RT (III).

In order to improve the stability of d-Ti_2CT_x solutions, the same protocol as in d-$Ti_3C_2T_x$ MXenes was applied, i.e. storing the solution in Ar@LT. Their normalized extinction spectra showed a significantly improved stability, **figure 8.10C**, with a τ of 10 days, 24 times higher than that of the Air@RT sample. After being stored in Ar@LT for 12 h, the d-Ti_2CT_x flakes were observed by TEM, showing relatively clean surfaces with well-defined edges and shapes, **figure 8.10F**.

Raman and XPS spectra, **figures 8.11A** and **B** respectively, further confirm the higher stability of d-Ti_2CT_x solution stored in Ar@LT, demonstrating that the proposed method for improving the stability of MXene aqueous solution is effective and universal. Moreover, the filtration of the d-Ti_2CT_x flakes could protect them from degradation over time, and by a simple re-dispersion process the dispersion could be obtained again. Despite that, the much smaller time constant in d-Ti_2CT_x compared to d-$Ti_3C_2T_x$ MXene in Ar@LT indicates the reaction speed between d-Ti_2CT_x and water is quite fast. This makes water a not suitable solvent for the storage of this colloidal solution and future work should be addressed on the identification of an ideal solvent for the Ti_2CT_x nanosheets.

8.4 Conclusions

Along the chapter, the stability of MXene aqueous solutions have been studied. Through the investigation of the degradation process in standard storing conditions, Air@RT, it has been regarded that the starting material slowly oxidize forming anatase TiO_2 and amorphous carbon. XPS analysis have revealed that other suboxides/hydroxides are involved in the degradation process, but only as intermediate stages in oxidation. Moreover, TEM and SEM observations have shown a preferential degradation on the edges of the flakes, making small flakes more sensitive to oxidation.

The degradation stage of the MXene colloidal solutions has been quantify by UV-Vis spectra analysis. In addition, the fitting of this oxidation as a function of time by a single exponential decay, have allowed us to extract a time constant of the degradation process. Through this method, the stability at low temperature and oxygen-free conditions has been explored. The storing in those environments has resulted in an impressive increase in the lifespan, revealing that the dissolved oxygen is the prime oxidizer, while water just a mild one.

To investigate the influence of the flake size in the stability, a cascade centrifugation method has been used to separate nanosheets by their size. By following the same methodology as before, the time constants of the size selected colloidal solutions have been obtained. Additionally, a clear correlation between the time constants and flake size, was obtained. This result can potentially permit the size determination of the nanosheets just from UV-Vis spectra. Moreover, this correlation has further proved a faster decay of the smaller flakes and the validity of the proposed storing conditions for increasing the lifetime of the colloidal solutions.

Due to the fact that even in Ar@LT the material still oxidizes, it has been proposed a long term preservation by filtering the solution and storing the material as a solid film. This strategy has proven to preserve extremely good the material and being fully reversible.

Finally, the study was extended to d-Ti_2CT_x, another material of the MXene family. The results obtained were in line of the observed in d-$Ti_3C_2T_x$. This undoubtedly demonstrate that the proposed protocols for extending the lifetime of MXene colloidal solutions, are applicable to all MXene family.

The ever-increasing attention that the MXenes have attracted in many applications, often involves the use of aqueous colloidal solutions. For this reason, the results of this chapter are fundamental to the future development of this promising material. Moreover, the proposed protocols facilitate the inclusion of the MXenes into the SiNWs electrodes, what compose some of the future work.

Chapter 9:

Conclusions and future work

Along the manuscript the most important results of each chapter have been summarized in the corresponding conclusion section. Similarly, in this chapter is gathered the most important conclusions of the thesis to provide a comprehensive picture of the performed work. Moreover, at the end of the chapter, it is discussed the future steps in this research area and the open perspectives of this work.

9.1 SiNWs for solar cells

The first study conducted in the work was the study of the morphological, chemical and structural characterization of the SiNWs growth by MACE. The synthesis method has been used along the different chapters of the manuscript, so this first study is extremely important to understand the growth mechanism and the properties of the material synthetized. From those analysis, it was observed that the SiNWs have a preferential growth in the [100] direction and a thin SiO_2 coverage is produced in SiNW surface, due to the MACE. The kinetics of the reactions has been also obtained, which has allowed us a good control of the growth.

SiNWs by MACE were applied in c-Si and highly absorbing surfaces were obtained. Their reflective properties were analyzed and compared with anti-reflective commercial technologies, showing a much better performance than the commercial solutions.

Despite of the great results as anti-reflective layers, the increase of surface recombination could be an important obstacle for achieving good efficiencies as solar cells. In order to delve into this problem two approaches were addressed: the increase of surface conductivity to obtain a better carrier collection and the reduction of the recombination *via* surface passivation.

The first approach was conducted by the *in situ* growth of a thin and conductive CNT layer on top of the SiNWs. This CNTs layer was achieved by a CVD growth and the characterization of the material showed a very high quality single walled CNTs. The reported growth method resulted in the formation of an interconnected net with a low resistivity (3 kΩ/□) and almost none affection to the reflective properties of the SiNWs.

The second way to improve the surface recombination of the SiNWs covered surfaces, was the study of the surface passivation. The surface passivation in silicon is usually achieved by the deposition of well-known dielectric layers. However, the regular SiNWs have such a small separation that when a layer is deposited, the material does not cover their whole surface, leading to a poor passivation. To solve this difficulty, it was developed a SiNWs growth assisted by patterns with higher SiNW separation. By this approach, it was obtained a very homogeneous deposition all over the surface. This method allowed the control of the SiNWs separation and diameter, by using AAO membranes directly grown on the Si as patterns. The AAO growth on Si substrates was previously scarcely explored. Along the corresponding chapter it has been conducted a thorough investigation to understand and control this growth method. This deep study resulted in a very precise control of the AAO and SiNW parameters which could potentially have applications in many other field.

9.2 SiNWs for lithium-ion batteries

The SiNWs were applied in the LIBs under three electrodes architectures, each of them showing substantial innovations.

The first type of electrode, consisted on the mixture of SiNWs with common batteries additives (binder and carbon black) deposited on top of Cu substrates. This method needs large quantities of SiNWs detached from a substrate that the common MACE cannot provide. In order to fulfill this requirement, the MACE process was applied until the etching consumed the whole thickness of the wafers. This extended process indeed produced enough SiNWs to allow the formation of batteries, but it was observed that obtained SiNWs had a much thicker oxide coverage than the common ones. Interestingly, it was obtained that the SiO_2 thickness was size depending, being much thicker in bigger SiNWs. This result allowed the development of an extra step in the SiNWs synthesis to remove the formed SiO_2 prior to its application on LIBs.

The assembled SiNWs electrodes showed a very good electrochemical performance being considerably better than other Si nanomaterials with comparable sizes. Additionally, the SiNWs were mixed with Si NPs of a considerably lower size and higher capacity. The mixture of these two materials revealed an extraordinary synergy, which combines the improved SiNPs capacity and SiNWs stronger structure, to form a hybrid electrode with a very good capacity and cycling performance.

The second type of electrode architecture was the free-standing electrode, formed by the mixture of SiNWs and CNTs. The first step in the optimization of this type of electrodes was the selection of the appropriate SiNWs/ CNT ratio, which have to be a compromise between the properties that each material adds to the mixture. This optimization was done

attending to the electrodes resistivity of and the maximization of the SiNWs content, obtaining an ideal ratio of 20% of CNTs.

The electrodes fabricated under this architecture showed very high capacities and cycling performance, revealing an extraordinary low degradation. However, these results were only from the 40 first cycles and longer cycling should be done to check if indeed the capacity fading is effectively suppressed.

The last method of the SiNWs integration into the LIBs, was the deposition of a-Si:H directly over the Cu substrates followed by a subsequent MACE etching. This method is the most innovative among the three tested because, to our knowledge, the use of this a-SiNWs in LIBs was never reported. In this case, the a-Si:H was deposited on the Cu substrates by two techniques, PECVD and RF-MS. Despite of the similarities in the deposited films, only the growth of a-SiNWs by MACE was achieved in the PECVD samples. A deep study was performed to delve into this subject, focusing on the film morphology and composition. It was found, that the RF-MS samples, had more hydrogen, but its incorporation was mainly in the form of polyhydrides which are much more inefficient passivating the material.

The bigger difficulty encountered in these novel electrodes was to accurately measure the mass of SiNW. The nature of the a-SiNWs synthesis process does not allow a direct measurement of the active mass of the electrodes. Therefore, the mass was obtained through the density, which was previously calculated from indirect measurements.

The a-SiNWs/Cu electrodes were assembled into batteries and were electrochemically characterized. They showed an extraordinary performance increase compared with the bare a-Si:H films, solving many of their major drawbacks. Furthermore, the surface/volume ratio increase achieved by the a-SiNWs/Cu electrodes could allow the utilization of carbon additives to improve the cycling performance of the material.

9.3 MXenes

The MXenes, a new family of 2D materials, was proposed to be used as additive for the SiNWs into LIBs. Their good electrochemical and conductive properties make them a good candidate to be paired with the SiNWs into LIBs. However, before this application, there are still fundamental aspects that need to be solved. The most important is that the MXenes are unstable in ambient conditions and no study stated the origins of this instability or a way to prevent it. Thus, in the present work the MXenes stability was studied.

This study revealed that the degradation of the Ti MXenes (Ti_2CT_x and $Ti_3C_2T_x$) colloidal solutions is an oxidation which results in the formation TiO_2 and amorphous carbon. The oxidation of the flakes is an edge-driven reaction which affects more intensely to the smaller flakes. The characteristic degradation time was obtained for standard storing conditions and different environments were proposed to extend the lifetime of the solutions. The oxidation rates in this environments showed a considerably higher lifespan, which in some cases were of several years. Additionally, this study revealed that the oxidizer agents responsible for the degradation of the material are primely the dissolved oxygen and, less intensely, the water. All these oxidizers were removed from the MXenes through vacuum filtration obtaining almost none material degradation.

9.4 Future work

Despite most of the topics treated along this work could be subjected to further work, probably are two main areas which, due to their novelty, would be the most interesting.

The first one would be the a-SiNWs implementation into batteries. The performance shown by this material without any additive outclass any other Si bare material. Therefore, it would be quite interesting observe the effect of different carbon additives into its capacity, and

specially into its cycling. A further development of this novel electrode architecture could be a high breakthrough in the Si based anodes for LIBs. Moreover, the easy scalability that the method presents could be really interesting to industry level applications.

The other field which also would be benefited with further work are the MXenes. Since its discovery, the interest on these materials has grown exponentially and its early stage of development makes them a very fruitful research area. The mixing of this material with the different kind of SiNWs studied could be an interesting next step in the development of both the SiNWs and MXenes.

Chapter 10:

Conclusiones y trabajo futuro

A lo largo del manuscrito, los resultados más importantes de cada capítulo se han ido resumido en las correspondientes secciones de conclusiones. De una forma similar, en este capítulo recogeremos las conclusiones más importantes de la tesis para proporcionar una imagen completa del trabajo realizado. Además, al final del capítulo discutiremos los pasos futuros en esta área de investigación y las perspectivas que deja abiertas este trabajo.

10.1 SiNWs para células solares

El primer estudio realizado en el trabajo fue la caracterización morfológica, química y estructural del crecimiento de SiNWs por MACE. Este método de síntesis se ha utilizado a lo largo de los diferentes capítulos del manuscrito, por lo que este primer estudio es extremadamente importante para comprender el mecanismo de crecimiento y las propiedades del material sintetizado. A partir de estos análisis, se observó que los SiNWs tienen un crecimiento preferencial en la dirección [100]. Además, se apreció que el MACE produce una fina capa de SiO_2 en la superficie de los SiNWs. Por otra parte, también se estudió la cinética de las reacciones involucradas en el proceso, permitiéndonos un gran control sobre el crecimiento.

Los SiNWs fueron crecidos por MACE en obleas de c-Si, obteniendo superficies altamente absorbentes. Sus propiedades ópticas fueron analizadas y comparadas con capas

antireflectantes comerciales, mostrando un rendimiento mucho mejor que las soluciones comerciales.

A pesar de los buenos resultados como capas antirreflectantes, el aumento que producen los SiNWs en la recombinación superficial podría ser un enorme obstáculo para lograr una buena eficiencia en células solares. Con el fin de profundizar en este problema, se abordaron dos enfoques: el aumento de la conductividad de la superficie para obtener una mejor recolección de portadores y la reducción de la recombinación a través de la pasivación de la superficie.

El primer enfoque fue llevado a cabo mediante el crecimiento, por CVD, de una capa fina y conductora de CNTs sobre los SiNWs. Esta lámina de CNTs se caracterizó mediante Raman, mostrando una composición predominante de CNTs de una sola pared de muy alta calidad. Además, mediante microscopía electrónica se observó que los CNTs crecen formando una red interconectada con una baja resistividad (3 kΩ/□) y sin tener casi ninguna influencia en las propiedades reflectoras de los SiNWs.

La segunda forma de mejorar la recombinación superficial de las superficies cubiertas con SiNWs fue el estudio de la pasivación superficial. Esta pasivación, en silicio normalmente se consigue mediante la deposición de capas dieléctricas bien conocidas. Sin embargo, los SiNWs comunes tienen una separación tan pequeña, que cuando se deposita una capa, el material no cubre toda su superficie y da lugar a una mala pasivación. Para resolver esta dificultad, se desarrolló un crecimiento de SiNWs asistido por patrones con mayor separación entre los SiNWs. La mejora del espaciado entre SiNWs nos permitió la deposición de láminas sobre los nanohilos de forma efectiva. Los patrones usados fueron membranas AAO directamente crecidas en el Si. En la bibliografía, el crecimiento directo de AAO sobre Si ha sido muy poco estudiado, por ello a lo largo del correspondiente capítulo, se a llevado a cabo una investigación exhaustiva para comprender y controlar este método de crecimiento. Este profundo estudio nos concedió un control muy preciso de los parámetros

tanto de las AAO como de los SiNW. A parte de la aplicación aquí estudiada, la gran versatilidad del método podría tener aplicaciones en muchos otros campos.

10.2 SiNWs para LIBs

Los SiNWs se aplicaron en las LIBs bajo tres configuraciones de electrodos, cada uno de ellos mostrando sustanciales innovaciones.

El primer tipo de electrodo, consistió en la mezcla de SiNWs con aditivos comunes de baterías (aglutinantes poliméricos y negro de acetileno) depositados sobre sustratos de Cu. Este método necesita grandes cantidades de SiNWs en forma de disolución, requisito que el MACE común no puede proporcionar. Para cumplir este requerimiento, se aplicó el procedimiento MACE hasta consumir todo el grosor de la oblea. Este proceso MACE prolongado fue capaz de producir bastantes SiNWs para permitir la formación de baterías, pero se observó que los SiNWs obtenidos tenían una cobertura de óxido mucho más gruesa que los comunes. El espesor del SiO_2 depende del tamaño de los SiNWs, siendo mucho más grueso en los nanohilos más grandes. Este resultado nos permitió desarrollar un paso extra en la síntesis de los SiNWs para eliminar el SiO_2 formado antes de que fueran aplicados en las LIBs.

La caracterización electroquímica de los electrodos de SiNWs, mostró un rendimiento muy bueno, siendo considerablemente mejor que otros nanomateriales de Si con tamaños comparables. Adicionalmente, los SiNWs se mezclaron con Si NPs de un tamaño menor y, por tanto, mayor capacidad electroquímica. La mezcla de estos dos materiales condujo a una extraordinaria sinergia, combinando la capacidad mejorada de las Si NPs y la sólida estructura de los SiNWs. Estos electrodos híbridos demostraron una muy buena capacidad y resistencia al ciclado.

El segundo tipo de configuración de electrodos fueron los electrodos "free-standing", formados por la mezcla de SiNWs y CNTs. El primer paso en la creación de este tipo de electrodos fue la determinación de la proporción de SiNWs/CNT apropiada. Esta debía mostrar un compromiso entre las propiedades que cada material añade a la mezcla para optimizar las capacidades electroquímicas del electrodo final. La optimización se realizó atendiendo a la resistividad de los electrodos y la maximización del contenido de SiNWs, obteniéndose una relación ideal de 20% en peso de CNTs.

Los electrodos fabricados de esta manera mostraron capacidades y rendimientos en el ciclado muy altos, revelando una extraordinariamente baja degradación de los SiNWs en presencia de los CNT. Sin embargo, estos resultados comentados fueron sólo en base de los primeros 40 ciclos. Para comprobar si efectivamente la disminución de la capacidad se suprime con la inclusión de los CNTs, habría que extender más el ciclado.

El último método de integración de los SiNWs en las LIBs, fue la deposición de a-Si:H directamente sobre los sustratos de Cu y el subsiguiente crecimiento de SiNWs con MACE. Este método es el más innovador entre los tres ensayados porque, en nuestro conocimiento, el crecimiento de este tipo de SiNWs para baterías nunca se ha reportado. El a-Si:H se depositó sobre los sustratos de Cu mediante dos técnicas, PECVD y RF-MS. Sin embargo, sólo el crecimiento de los a-SiNWs por MACE se logró en las muestras PECVD. Para profundizar en este tema se realizó un concienzudo estudio sobre la morfología y composición de las láminas depositadas. Mediante FTIR y técnicas IBA se encontró que las muestras de RF-MS tenían más hidrógeno, pero su incorporación estaba principalmente en forma de polihidruros, que son menos eficaces pasivando el material.

La mayor dificultad encontrada en la formación de estos novedosos electrodos fue medir con precisión la masa de los a-SiNWs. La naturaleza del proceso de síntesis de los a-SiNWs no permite una medida directa de la masa activa de los electrodos. Por lo tanto, este valor de

masa se obtuvo a través de la densidad, que, así mismo, se extrajo de mediciones indirectas y cálculos teóricos sobre las películas.

Los electrodos a-SiNWs/Cu se ensamblaron en baterías y se caracterizaron electroquímicamente. Estos mostraron un extraordinario aumento de rendimiento en comparación con las láminas de a-Si:H, resolviendo muchos de sus principales inconvenientes. Además, el increíble aumento de la relación superficie/volumen conseguido mediante la creación de los a-SiNWs, podría permitir la utilización de aditivos de carbono para mejorar el ciclado del material, lo cual no es posible en las películas de a-Si:H.

10.3 MXenes

Los MXenes, una nueva familia de materiales 2D, se propusieron en este trabajo para ser utilizados como aditivo junto con los SiNWs en las LIBs. Sus buenas propiedades electroquímicas, así como alta conductividad, los convierten en un extraordinario candidato para ser empleado junto con los SiNWs en las LIBs. Sin embargo, antes de esta aplicación, todavía hay aspectos fundamentales que necesitan ser resueltos. Lo más importante es que los MXenes son inestables en condiciones ambientales estándar. Como ningún estudio ha reportado los orígenes de esta inestabilidad, ni una manera de prevenirlo, en el presente trabajo se persigue este objetivo: el estudio de la estabilidad de los MXenes.

En este estudio se llegó a la conclusión de que la degradación de las soluciones coloidales de MXenes de Ti (Ti_2CT_x y $Ti_3C_2T_x$) da como resultado la formación de TiO_2 y carbono amorfo. Por distintas técnicas, se estudió el tiempo de degradación característico de los materiales, y se propusieron diferentes ambientes de almacenamiento. El estudio de la degradación reveló que los agentes oxidantes responsables de la oxidación del material son principalmente el oxígeno disuelto en el agua y, menos intensamente, el agua. Las condiciones propuestas de almacenamiento produjeron un enorme aumento de la vida útil de los materiales,

permitiendo un método de almacenamiento a largo plazo. Los tiempos de vida más largos obtenidos (más de 2 años) fueron para las condiciones Ar @ Lt, cuando el material está en forma de solución coloidal. También se observó que cuando el material es separado del agua, la degradación es prácticamente nula, siendo esta otra válida forma de almacenamiento a largo plazo. Adicionalmente, se observó que el proceso de degradación es una reacción más intensa en los bordes, dando lugar a que los nanocompuestos más pequeños sean los más sensibles a la oxidación.

10.4 Trabajo futuro

La mayoría de los temas tratados a lo largo de este trabajo podrían ser objeto de un estudio más profundo; sin embargo, probablemente hay dos áreas que, por su novedad, serían las más interesantes de ampliar.

La primera sería la implementación de los a-SiNWs en baterías. El rendimiento mostrado por este material sin ningún aditivo supera a cualquier otro material de Si. Por lo tanto, sería muy interesante analizar el efecto de los diferentes aditivos de carbono en su capacidad, y especialmente en su ciclado. Un desarrollo en mayor profundidad de esta nueva arquitectura de electrodo podría suponer un gran avance en los ánodos basados en Si para LIBs. Por otra parte, este método presenta una fácil escalabilidad, siendo muy interesante para aplicaciones a nivel industrial.

El otro campo que también podría ser muy fructífero es el de los MXenes. Desde su descubrimiento, el interés por estos materiales ha crecido exponencialmente y su temprana etapa de desarrollo los convierte en un área de investigación muy atractiva. El desarrollo de electrodos híbridos de SiNWs/MXenes podría ser un interesante paso en la aplicación estos materiales en las LIBs.

BIBLIOGRAPHY:

1. Sze, S. M. & Ng, K. K. *Physics of semiconductor devices*. (Wiley-Interscience, 2007).

2. Banerjee, B. & Sanjay, S. *Solid State Electronic Devices*. (2005).

3. Muller, a, Ghosh, M., Sonnenschein, R. & Woditsch, P. Silicon for photovoltaic applications. *Mater. Sci. Eng. B-Solid State Mater. Adv. Technol.* **134,** 257–262 (2006).

4. *Silicon*. (Springer Berlin Heidelberg, 2004).

5. Han, H., Huang, Z. P. & Lee, W. Metal-assisted chemical etching of silicon and nanotechnology applications. *Nano Today* **9,** 271–304 (2014).

6. Lee, J. K., Smith, K. B., Hayner, C. M. & Kung, H. H. Silicon nanoparticles-graphene paper composites for Li ion battery anodes. *Chem. Commun.* **46,** 2025–2027 (2010).

7. Xu, Z. *et al.* Water-soluble PEGylated silicon nanoparticles and their assembly into swellable nanoparticle aggregates. *J. Nanoparticle Res.* **17,** 56 (2015).

8. Yao, Y. *et al.* Interconnected silicon hollow nanospheres for lithium-ion battery anodes with long cycle life. *Nano Lett.* **11,** 2949–2954 (2011).

9. Song, T. *et al.* Arrays of sealed silicon nanotubes as anodes for lithium ion batteries. *Nano Lett.* **10,** 1710–1716 (2010).

10. Peng, K. Q., Wang, X., Li, L., Hu, Y. & Lee, S. T. Silicon nanowires for advanced energy conversion and storage. *Nano Today* **8,** 75–97 (2013).

11. Hsu, C. M., Connor, S. T., Tang, M. X. & Cui, Y. Wafer-scale silicon nanopillars and nanocones by Langmuir-Blodgett assembly and etching. *Appl. Phys. Lett.* **93,** 133109

(2008).

12. Law, M., Goldberger, J. & Yang, P. D. Semiconductor nanowires and nanotubes. *Annu. Rev. Mater. Res.* **34,** 83–122 (2004).

13. Huang, Z. P. *et al.* Metal-Assisted Chemical Etching of Silicon: A Review. *Adv. Mater.* **23,** 285–308 (2011).

14. Choi, W. K. *et al.* Synthesis of silicon nanowires and nanofin arrays using interference lithography and catalytic etching. *Nano Lett.* **8,** 3799–3802 (2008).

15. Huang, Z., Fang, H. & Zhu, J. Fabrication of silicon nanowire arrays with controlled diameter, length, and density. *Adv. Mater.* **19,** 744–748 (2007).

16. Huang, Z. *et al.* Extended arrays of vertically aligned Sub-10 nm diameter [100] Si nanowires by metal-assisted chemical etching. *Nano Lett.* **8,** 3046–3051 (2008).

17. Peng, K. Q. *et al.* Uniform, axial-orientation alignment of one-dimensional single-crystal silicon nanostructure arrays. *Angew. Chemie-International Ed.* **44,** 2737–2742 (2005).

18. OGATA, Y., KOBAYASHI, K. & MOTOYAMA, M. Electrochemical metal deposition on silicon. *Curr. Opin. Solid State Mater. Sci.* **10,** 163–172 (2006).

19. Flätgen, G. *et al.* Autocatalytic mechanism of H2O2 reduction on Ag electrodes in acidic electrolyte: experiments and simulations. *Electrochim. Acta* **44,** 4499–4506 (1999).

20. Srivastava, S. K. *et al.* Large area fabrication of vertical silicon nanowire arrays by silver-assisted single-step chemical etching and their formation kinetics. *Nanotechnology* **25,** 17 (2014).

21. Garnett, E. & Yang, P. Silicon nanowire radial p-n junction solar cells. *J. Am. Chem. Soc.* **130,** 9224–5 (2008).

22. Qu, Y. *et al.* Electrically Conductive and Optically Active Porous Silicon Nanowires. *Nano Lett.* **9,** 4539–4543 (2009).

23. Guo, C. S. *et al.* Surface passivation and transfer doping of silicon nanowires. *Angew. Chemie - Int. Ed.* **48,** 9896–9900 (2009).

24. Luo, L. *et al.* Silicon nanowire sensors for Hg2+ and Cd2+ ions. *Appl. Phys. Lett.* **94,** (2009).

25. Wang, Q. *et al.* Field emission properties of carbon coated Si nanocone arrays on porous silicon. *Nanotechnology* **16,** 2919–2922 (2005).

26. Peng, K.-Q. & Lee, S.-T. Silicon nanowires for photovoltaic solar energy conversion. *Adv. Mater.* **23,** 198–215 (2011).

27. Kelzenberg, M. D. *et al.* Enhanced absorption and carrier collection in Si wire arrays for photovoltaic applications. *Nat. Mater.* **9,** 239–244 (2010).

28. Peplow, M. Graphene: The quest for supercarbon. *Nature* **503,** 327–329 (2013).

29. Khan, U. *et al.* Polymer reinforcement using liquid-exfoliated boron nitride nanosheets. *Nanoscale* **5,** 581–7 (2013).

30. Chhowalla, M., Liu, Z. & Zhang, H. Two-dimensional transition metal dichalcogenide (TMD) nanosheets. *Chem. Soc. Rev.* **44,** 2584–2586 (2015).

31. Zhang, C. J. *et al.* Layered Orthorhombic Nb2O5@Nb4C3Tx and TiO2@Ti3C2Tx Hierarchical Composites for High Performance Li-ion Batteries. *Adv. Funct. Mater.* **26,** 4143–4151 (2016).

32. Beidaghi, M. *et al.* One-Step Synthesis of Carbon Supported Nb2O5 Particles for Electrochemical Capacitor Applications by Oxidation of Layered Nb2C. *Meet. Abstr.* **MA2014-02,** 185 (2014).

33. Naguib, M. *et al.* One-step synthesis of nanocrystalline transition metal oxides on thin sheets of disordered graphitic carbon by oxidation of MXenes. *Chem. Commun.* **50,** 7420–7423 (2014).

34. Wang, Q. & O'Hare, D. Recent Advances in the Synthesis and Application of Layered Double Hydroxide (LDH) Nanosheets. *Chem. Rev.* **112,** 4124–4155 (2012).

35. Raccichini, R., Varzi, A., Passerini, S. & Scrosati, B. The role of graphene for electrochemical energy storage. *Nat. Mater.* **14,** 271–279 (2015).

36. Kong, L. *et al.* Free-Standing T-Nb2O5/Graphene Composite Papers with Ultrahigh Gravimetric/Volumetric Capacitance for Li-Ion Intercalation Pseudocapacitor. *ACS Nano* **9,** 11200–11208 (2015).

37. Zhang, C. *et al.* Synthesis and Charge Storage Properties of Hierarchical Niobium Pentoxide/Carbon/Niobium Carbide (MXene) Hybrid Materials. *Chem. Mater.* **28,** 3937–3943 (2016).

38. Wei, Y. *et al.* Layered carbide-derived carbon with hierarchically porous structure for high rate lithium-sulfur batteries. *Electrochim. Acta* **188,** 385–392 (2016).

39. Kong, L. *et al.* Ultrahigh intercalation pseudocapacitance of mesoporous orthorhombic niobium pentoxide from a novel cellulose nanocrystal template. *Mater. Chem. Phys.* **149–150,** 495–504 (2015).

40. Kong, L. *et al.* Nanoarchitectured Nb2O5 hollow, Nb2O5@carbon and NbO2@carbon Core-Shell Microspheres for Ultrahigh-Rate Intercalation Pseudocapacitors. *Sci. Rep.* **6,** 21177 (2016).

41. Hu, Z. *et al.* Al-doped α-MnO2 for high mass-loading pseudocapacitor with excellent cycling stability. *Nano Energy* **11,** 226–234 (2015).

42. Xiao, X. *et al.* Freestanding MoO3−x nanobelt/carbon nanotube films for Li-ion intercalation pseudocapacitors. *Nano Energy* **9,** 355–363 (2014).

43. Xiao, X. *et al.* Intercalation of cations into partially reduced molybdenum oxide for high-rate pseudocapacitors. *Energy Storage Mater.* **1,** 1–8 (2015).

44. Zhang, C. (John) *et al.* Synthesis and electrochemical properties of niobium pentoxide deposited on layered carbide-derived carbon. *J. Power Sources* **274,** 121–129 (2015).

45. Kong, L. *et al.* High-power and high-energy asymmetric supercapacitors based on Li + -intercalation into a T-Nb2O5/graphene pseudocapacitive electrode. *J. Mater. Chem. A* **2,** 17962–17970 (2014).

46. Kim, Y. H. *et al.* Self-Activated Transparent All-Graphene Gas Sensor with Endurance to Humidity and Mechanical Bending. *ACS Nano* **9,** 10453–10460 (2015).

47. Liu, Z., Lau, S. P. & Yan, F. Functionalized graphene and other two-dimensional materials for photovoltaic devices: device design and processing. *Chem. Soc. Rev.* **44,** 5638–5679 (2015).

48. Naguib, M. *et al.* Two-dimensional transition metal carbides. *ACS Nano* **6,** 1322–31 (2012).

49. Urbankowski, P. *et al.* Synthesis of two-dimensional titanium nitride Ti4N3 (MXene). *Nanoscale* **8,** 11385–11391 (2016).

50. Ghidiu, M., Lukatskaya, M. R., Zhao, M.-Q., Gogotsi, Y. & Barsoum, M. W. Conductive two-dimensional titanium carbide 'clay' with high volumetric capacitance. *Nature* **516,** 78–81 (2014).

51. Anasori, B., Lukatskaya, M. R. & Gogotsi, Y. 2D metal carbides and nitrides (MXenes) for energy storage. *Nat. Rev. Mater.* **2,** 16098 (2017).

52. Kim, S. J. *et al.* High mass loading, binder-free MXene anodes for high areal capacity Li-ion batteries. *Electrochim. Acta* **163,** 246–251 (2015).

53. Lukatskaya, M. R. *et al.* Cation intercalation and high volumetric capacitance of two-dimensional titanium carbide. *Science.* **341,** 1502–5 (2013).

54. Dall'Agnese, Y., Taberna, P.-L., Gogotsi, Y. & Simon, P. Two-Dimensional Vanadium Carbide (MXene) as Positive Electrode for Sodium-Ion Capacitors. *J. Phys. Chem. Lett.* **6,** 2305–2309 (2015).

55. Mashtalir, O. *et al.* Intercalation and delamination of layered carbides and carbonitrides. *Nat. Commun.* **4,** 1716 (2013).

56. Anasori, B. *et al.* Two-Dimensional, Ordered, Double Transition Metals Carbides (MXenes). *ACS Nano* **9,** 9507–9516 (2015).

57. Mashtalir, O., Lukatskaya, M. R., Zhao, M.-Q., Barsoum, M. W. & Gogotsi, Y. Amine-Assisted Delamination of Nb2 C MXene for Li-Ion Energy Storage Devices. *Adv. Mater.* **27,** 3501–3506 (2015).

58. Halim, J. *et al.* Synthesis and Characterization of 2D Molybdenum Carbide (MXene). *Adv. Funct. Mater.* **26,** 3118–3127 (2016).

59. Pierson, H. O. *Handbook of chemical vapor deposition*. (Noyes Publications, 1999).

60. Ohring, M. in *Materials Science of Thin Films* 203–275 (2002).

61. Ehrlich, G. M. *Lithium-Ion Batteries*. *Handbook of Batteries* (2002).

62. Zhang, W. Lithium insertion / extraction mechanism in alloy anodes for lithium-ion batteries. *J. Power Sources* **196,** 877–885 (2011).

63. Wu, S. L., Zhang, T., Zheng, R. T. & Cheng, G. A. Facile morphological control of single-crystalline silicon nanowires. *Appl. Surf. Sci.* **258,** 9792–9799 (2012).

64. Peng, K. *et al.* Ordered silicon nanowire arrays via nanosphere lithography and metal-induced etching. *Appl. Phys. Lett.* **90,** 1–4 (2007).

65. Peng, K., Lu, A., Zhang, R. & Lee, S.-T. Motility of Metal Nanoparticles in Silicon and Induced Anisotropic Silicon Etching. *Adv. Funct. Mater.* **18,** 3026–3035 (2008).

66. Huang, Z. P. *et al.* Ordered Arrays of Vertically Aligned 110 Silicon Nanowires by Suppressing the Crystallographically Preferred Etching Directions. *Nano Lett.* **9,** 2519–2525 (2009).

67. Tsujino, K. & Matsumura, M. Boring deep cylindrical nanoholes in silicon using silver nanoparticles as a catalyst. *Adv. Mater.* **17,** 1045–1047 (2005).

68. Perez, J. M. *et al.* Direct evidence for the amorphous silicon phase in visible photoluminescent porous silicon. *Appl. Phys. Lett.* **61,** 563–565 (1992).

69. Nemanick, E. J. *et al.* Chemical and Electrical Passivation of Single-Crystal Silicon(100) Surfaces through a Two-Step Chlorination/Alkylation Process. (2006).

70. Cheng, S. L., Chung, C. H. & Lee, H. C. A Study of the Synthesis, Characterization, and Kinetics of Vertical Silicon Nanowire Arrays on (001)Si Substrates. *J. Electrochem. Soc.* **155,** D711 (2008).

71. Srivastava, S. K. *et al.* Excellent antireflection properties of vertical silicon nanowire arrays. *Sol. Energy Mater. Sol. Cells* **94,** 1506–1511 (2010).

72. Hung, Y.-J., Lee, S.-L., Wu, K.-C., Tai, Y. & Pan, Y.-T. Antireflective silicon surface with vertical-aligned silicon nanowires realized by simple wet chemical etching processes. *Opt. Express* **19,** 15792 (2011).

73. Kumar, D., Srivastava, S. K., Singh, P. K., Husain, M. & Kumar, V. Fabrication of silicon nanowire arrays based solar cell with improved performance. *Sol. Energy Mater.*

Sol. Cells **95,** 215–218 (2011).

74. Shockley, W. & Read, W. T. Statistics of the Recombination of Holes and Electrons. *Phys. Rev.* **87,** 835–842 (1952).

75. Srivastava, S. K., Kumar, D., Singh, P. K., Kumar, V. & Ieee. SILICON NANOWIRE ARRAYS BASED 'BLACK SILICON' SOLAR CELLS. *34th IEEE Photovoltaic Specialists Conference* 1008–1013 (2009).

76. Murakami, Y. *et al.* Growth of vertically aligned single-walled carbon nanotube films on quartz substrates and their optical anisotropy. *Chem. Phys. Lett.* **2004,** 298 (2004).

77. Morant, C. *et al.* Mo–Co catalyst nanoparticles: Comparative study between TiN and Si surfaces for single-walled carbon nanotube growth. *Thin Solid Films* **520,** 5232–5238 (2012).

78. Dresselhaus, M. S., Dresselhaus, G., Saito, R. & Jorio, A. Raman spectroscopy of carbon nanotubes. *Phys. Reports-Review Sect. Phys. Lett.* **409,** 47–99 (2005).

79. Jorio, A. *et al.* Structural (n, m) determination of isolated single-wall carbon nanotubes by resonant Raman scattering. *Phys. Rev. Lett.* **86,** 1118–1121 (2001).

80. Milnera, M., Kürti, J., Hulman, M. & Kuzmany, H. Periodic Resonance Excitation and Intertube Interaction from Quasicontinuous Distributed Helicities in Single-Wall Carbon Nanotubes. *Phys. Rev. Lett.* **84,** 1324–1327 (2000).

81. Ebbesen, T. W. & Ajayan, P. M. Large-scale synthesis of carbon nanotubes. *Nature* **358,** 220–222 (1992).

82. Tune, D. D., Flavel, B. S., Krupke, R. & Shapter, J. G. Carbon Nanotube-Silicon Solar Cells. *Adv. Energy Mater.* **2,** 1043–1055 (2012).

83. Scardaci, V., Coull, R. & Coleman, J. N. Very thin transparent, conductive carbon

nanotube films on flexible substrates. *Appl. Phys. Lett.* **97,** 5–8 (2010).

84. Tune, D. D., Blanch, A. J., Krupke, R., Flavel, B. S. & Shapter, J. G. Nanotube film metallicity and its effect on the performance of carbon nanotube-silicon solar cells. *Phys. Status Solidi* **211,** 1479–1487 (2014).

85. Li, Z. R. *et al.* Light-harvesting using high density p-type single wall carbon nanotube/n-type silicon heterojunctions. *ACS Nano* **3,** 1407–1414 (2009).

86. Ma, W. J. *et al.* Directly synthesized strong, highly conducting, transparent single-walled carbon nanotube films. *Nano Lett.* **7,** 2307–2311 (2007).

87. Li, Z. *et al.* Large area, highly transparent carbon nanotube spiderwebs for energy harvesting. *J. Mater. Chem.* **20,** 7236 (2010).

88. Soppe, W., Rieffe, H. & Weeber, A. Bulk and surface passivation of silicon solar cells accomplished by silicon nitride deposited on industrial scale by microwave PECVD. *Prog. Photovoltaics Res. Appl.* **13,** 551–569 (2005).

89. Van Sark, W. G. J. H. M. in *Thin Films and Nanostructures* **30,** 1–215 (2002).

90. Hoex, B., Heil, S. B. S., Langereis, E., Van De Banden, M. C. M. & Kessels, W. M. M. Ultralow surface recombination of c-Si substrates passivated by plasma-assisted atomic layer deposited Al2O3. *Appl. Phys. Lett.* **89,** 42112 (2006).

91. Liu, Y. *et al.* Nanostructure formation and passivation of large-area black silicon for solar cell applications. *Small* **8,** 1392–1397 (2012).

92. Ben Jaballah, A., Moumni, B. & Bessais, B. Formation, rapid thermal oxidation and passivation of solar grade silicon nanowires for advanced photovoltaic applications. *Sol. Energy* **86,** 1955–1961 (2012).

93. Goldberger, J., Hochbaum, A. I., Fan, R. & Yang, P. D. Silicon Vertically Integrated

Nanowire Field Effect Transistors. *Nano Lett.* **6,** 973–977 (2006).

94. Cui, Y., Zhong, Z., Wang, D., Wang, W. U. & Lieber, C. M. High performance silicon nanowire field effect transistors. *Nano Lett.* **3,** 149–152 (2003).

95. Guichard, A. R., Barsic, D. N., Sharma, S., Kamins, T. I. & Brongersma, M. L. Tunable Light Emission from Quantum-Confined Excitons in TiSi2-Catalyzed Silicon Nanowires. *Nano Lett.* **6,** 2140–2144 (2006).

96. Wu, Y., Fan, R. & Yang, P. Block-by-Block Growth of Single-Crystalline Si/SiGe Superlattice Nanowires. *Nano Lett.* **2,** 83–86 (2002).

97. Su, X. *et al.* Silicon-Based Nanomaterials for Lithium-Ion Batteries: A Review. *Adv. Energy Mater.* **4,** 1300882 (2014).

98. Md Jani, A. M., Losic, D. & Voelcker, N. H. Nanoporous anodic aluminium oxide: Advances in surface engineering and emerging applications. *Prog. Mater. Sci.* **58,** 636–704 (2013).

99. Li, A. P., Müller, F., Birner, A., Nielsch, K. & Gösele, U. Hexagonal pore arrays with a 50–420 nm interpore distance formed by self-organization in anodic alumina. *J. Appl. Phys.* **84,** 6023–6026 (1998).

100. Zhang, F., Liu, X., Pan, C. & Zhu, J. Nano-porous anodic aluminium oxide membranes with 6–19 nm pore diameters formed by a low-potential anodizing process. *Nanotechnology* **18,** 345302 (2007).

101. Li, a. P. Polycrystalline and Monocrystalline Pore Arrays with Large Interpore Distance in Anodic Alumina. *Electrochem. Solid-State Lett.* **3,** 131 (1999).

102. Kim, J. *et al.* Au/Ag bilayered metal mesh as a si etching catalyst for controlled fabrication of si nanowires. *ACS Nano* **5,** 3222–9 (2011).

103. Chahrour, K. M., Ahmed, N. M., Hashim, M. R., Elfadill, N. G. & Qaeed, M. a. Controllable fabrication of highly ordered thin AAO template on Si substrate for electrodeposition of nanostructures. *Appl. Phys. A* **116,** 1389–1393 (2014).

104. Yan, B., Pham, H. T. M., Ma, Y., Zhuang, Y. & Sarro, P. M. Fabrication of in situ ultrathin anodic aluminum oxide layers for nanostructuring on silicon substrate. *Appl. Phys. Lett.* **91,** 130–132 (2007).

105. Lee, W. & Kim, J.-C. Highly ordered porous alumina with tailor-made pore structures fabricated by pulse anodization. *Nanotechnology* **21,** 485304 (2010).

106. Ono, S., Saito, M. & Asoh, H. Self-ordering of anodic porous alumina formed in organic acid electrolytes. *Electrochim. Acta* **51,** 827–833 (2005).

107. Nielsch, K., Choi, J., Schwirn, K., Wehrspohn, R. B. & Gösele, U. Self-ordering Regimes of Porous Alumina: The 10 Porosity Rule. *Nano Lett.* **2,** 677–680 (2002).

108. Parkhutik, V. P. & Shershulsky, V. I. Theoretical modelling of porous oxide growth on aluminium. *J. Phys. D. Appl. Phys.* **25,** 1258–1263 (1992).

109. Masuda, H., Nagae, M., Morikawa, T. & Nishio, K. Long-Range-Ordered Anodic Porous Alumina with Reduced Hole Interval Formed in Highly Concentrated Sulfuric Acid Solution. *Jpn. J. Appl. Phys.* **45,** L406–L408 (2006).

110. Lee, C. L., Tsujino, K., Kanda, Y., Ikeda, S. & Matsumura, M. Pore formation in silicon by wet etching using micrometre-sized metal particles as catalysts. *J. Mater. Chem.* **18,** 1015–1020 (2008).

111. Landi, B. J., Ganter, M. J., Cress, C. D., DiLeo, R. a. & Raffaelle, R. P. Carbon nanotubes for lithium ion batteries. *Energy Environ. Sci.* **2,** 638 (2009).

112. Zhang, W.-J. A review of the electrochemical performance of alloy anodes for lithium-

ion batteries. *J. Power Sources* **196,** 13–24 (2011).

113. Wang, W. & Kumta, P. N. Nanostructured Hybrid Silicon/Carbon Nanotube Heterostructures: Reversible High-Capacity Lithium-Ion Anodes. *ACS Nano* **4,** 2233–2241 (2010).

114. Thompson, a. H. Electrochemical Potential Spectroscopy: A New Electrochemical Measurement. *J. Electrochem. Soc.* **126,** 608 (1979).

115. Chevrier, V. L. *et al.* Evaluating Si-Based Materials for Li-Ion Batteries in Commercially Relevant Negative Electrodes. *J. Electrochem. Soc.* **161,** A783–A791 (2014).

116. Vu, A., Qian, Y. & Stein, A. Porous electrode materials for lithium-ion batteries-how to prepare them and what makes them special. *Adv. Energy Mater.* **2,** 1056–1085 (2012).

117. Chen, D. *et al.* Reversible Lithium-Ion Storage in Silver-Treated Nanoscale Hollow Porous Silicon Particles. *Angew. Chemie Int. Ed.* **51,** 2409–2413 (2012).

118. Martin, C. *et al.* Chemical Coupling of Carbon Nanotubes and Silicon Nanoparticles for Improved Negative Electrode Performance in Lithium-Ion Batteries. *Adv. Funct. Mater.* **21,** 3524–3530 (2011).

119. Li, X. & Bohn, P. W. Metal-assisted chemical etching in HF/H(2)O(2) produces porous silicon. *Appl. Phys. Lett.* **77,** 2572–2574 (2000).

120. Chartier, C., Bastide, S. & Levy-Clement, C. Metal-assisted chemical etching of silicon in HF-H2O2. *Electrochim. Acta* **53,** 5509–5516 (2008).

121. McDowell, M. T. *et al.* Novel size and surface oxide effects in silicon nanowires as lithium battery anodes. *Nano Lett.* **11,** 4018–4025 (2011).

122. Chan, C. K., Ruffo, R., Hong, S. S., Huggins, R. A. & Cui, Y. Structural and

electrochemical study of the reaction of lithium with silicon nanowires. *J. Power Sources* **189,** 34–39 (2009).

123. Chan, C. K., Ruffo, R., Sae Hong, S. & Cui, Y. Surface chemistry and morphology of the solid electrolyte interphase on silicon nanowire lithium-ion battery anodes. *J. Power Sources* **189,** 1132–1140 (2009).

124. Obrovac, M. N. & Krause, L. J. Reversible Cycling of Crystalline Silicon Powder. *J. Electrochem. Soc.* **154,** A103 (2007).

125. Hatchard, T. D. & Dahn, J. R. In Situ XRD and Electrochemical Study of the Reaction of Lithium with Amorphous Silicon. *J. Electrochem. Soc.* **151,** A838–A842 (2004).

126. Li, J. & Dahn, J. R. An in situ X-ray diffraction study of the reaction of Li with crystalline Si. *J. Electrochem. Soc.* **154,** A156–A161 (2007).

127. Obrovac, M. N. & Christensen, L. Structural Changes in Silicon Anodes during Lithium Insertion/Extraction. *Electrochem. Solid-State Lett.* **7,** A93–A96 (2004).

128. Liu, N. *et al.* A pomegranate-inspired nanoscale design for large-volume-change lithium battery anodes. *Nat. Nanotechnol.* **9,** 187–92 (2014).

129. Wu, H. *et al.* Stable cycling of double-walled silicon nanotube battery anodes through solid–electrolyte interphase control. *Nat. Nanotechnol.* **7,** 310–315 (2012).

130. Magasinski, a *et al.* High-performance lithium-ion anodes using a hierarchical bottom-up approach. *Nat. Mater.* **9,** 353–358 (2010).

131. Kim, H., Han, B., Choo, J. & Cho, J. Three-dimensional porous silicon particles for use in high-performance lithium secondary batteries. *Angew. Chemie - Int. Ed.* **47,** 10151–10154 (2008).

132. Eom, J. Y., Park, J. W., Kwon, H. S. & Rajendran, S. Electrochemical Insertion of

Lithium into Multiwalled Carbon Nanotube/Silicon Composites Produced by Ballmilling. *J. Electrochem. Soc.* **153,** A1678 (2006).

133. Higgins, T. M. *et al.* Effect of Percolation on the Capacitance of Supercapacitor Electrodes Prepared from Composites of Manganese Dioxide Nanoplatelets and Carbon Nanotubes. *ACS Nano* **8,** 9567–9579 (2014).

134. Huang, Z.-D. *et al.* Binder-free graphene/carbon nanotube/silicon hybrid grid as freestanding anode for high capacity lithium ion batteries. *Compos. Part A Appl. Sci. Manuf.* **84,** 386–392 (2016).

135. Kim, T., Mo, Y. H., Nahm, K. S. & Oh, S. M. Carbon nanotubes (CNTs) as a buffer layer in silicon/CNTs composite electrodes for lithium secondary batteries. *J. Power Sources* **162,** 1275–1281 (2006).

136. Yue, X., Sun, W., Zhang, J., Wang, F. & Sun, K. Facile synthesis of 3D silicon/carbon nanotube capsule composites as anodes for high-performance lithium-ion batteries. *J. Power Sources* **329,** 422–427 (2016).

137. Zhang, Y. *et al.* Silicon-multi-walled carbon nanotubes-carbon microspherical composite as high-performance anode for lithium-ion batteries. *J. Mater. Sci.* **52,** 3630–3641 (2017).

138. Chou, S.-L. *et al.* Silicon/Single-Walled Carbon Nanotube Composite Paper as a Flexible Anode Material for Lithium Ion Batteries. *J. Phys. Chem. C* **114,** 15862–15867 (2010).

139. Cui, L.-F., Ruffo, R., Chan, C. K., Peng, H. & Cui, Y. Crystalline-Amorphous Core−Shell Silicon Nanowires for High Capacity and High Current Battery Electrodes. *Nano Lett.* **9,** 491–495 (2009).

140. Miyazaki, R., Ohta, N., Ohnishi, T., Sakaguchi, I. & Takada, K. An amorphous Si film

anode for all-solid-state lithium batteries. *J. Power Sources* **272,** 541–545 (2014).

141. Szczech, J. R. & Jin, S. Nanostructured silicon for high capacity lithium battery anodes. *Energy Environ. Sci.* **4,** 56 (2011).

142. Bourderau, S., Brousse, T. & Schleich, D. . Amorphous silicon as a possible anode material for Li-ion batteries. *J. Power Sources* **81–82,** 233–236 (1999).

143. Moon, T., Kim, C. & Park, B. Electrochemical performance of amorphous-silicon thin films for lithium rechargeable batteries. *J. Power Sources* **155,** 391–394 (2006).

144. Lee, K. L., Jung, J. Y., Lee, S. W., Moon, H. S. & Park, J. W. Electrochemical characteristics of a-Si thin film anode for Li-ion rechargeable batteries. *J. Power Sources* **129,** 270–274 (2004).

145. Baranchugov, V., Markevich, E., Pollak, E., Salitra, G. & Aurbach, D. Amorphous silicon thin films as a high capacity anodes for Li-ion batteries in ionic liquid electrolytes. *Electrochem. commun.* **9,** 796–800 (2007).

146. Berla, L. A., Lee, S. W., Ryu, I., Cui, Y. & Nix, W. D. Robustness of amorphous silicon during the initial lithiation/delithiation cycle. *J. Power Sources* **258,** 253–259 (2014).

147. Douani, R., Piret, G., Hadjersi, T., Chazalviel, J.-N. & Solomon, I. Formation of a-Si:H and a-Si1-xCx :H nanowires by Ag-assisted electroless etching in aqueous HF/AgNO3 solution. *Thin Solid Films* **519,** 5383–5387 (2011).

148. Brodsky, M. H., Cardona, M. & Cuomo, J. J. Infrared and Raman spectra of the silicon-hydrogen bonds in amorphous silicon prepared by glow discharge and sputtering. *Phys. Rev. B* **16,** 3556–3571 (1977).

149. Langford, a. a., Fleet, M. L., Nelson, B. P., Lanford, W. a. & Maley, N. Infrared absorption strength and hydrogen content of hydrogenated amorphous silicon. *Phys.*

Rev. B **45,** 13367–13377 (1992).

150. Smets, A. H. M., Kessels, W. M. M. & van de Sanden, M. C. M. Vacancies and voids in hydrogenated amorphous silicon. *Appl. Phys. Lett.* **82,** 1547–1549 (2003).

151. Remeš, Z., Vaněček, M., Mahan, a. & Crandall, R. Silicon network relaxation in amorphous hydrogenated silicon. *Phys. Rev. B* **56,** R12710–R12713 (1997).

152. Remeš, Z. *et al.* Optical determination of the mass density of amorphous and microcrystalline silicon layers with different hydrogen contents. *J. Non. Cryst. Solids* **227–230,** 876–879 (1998).

153. Yoshio, M. *et al.* Carbon-Coated Si as a Lithium-Ion Battery Anode Material. *J. Electrochem. Soc.* **149,** A1598 (2002).

154. Boukamp, B. A. All-Solid Lithium Electrodes with Mixed-Conductor Matrix. *J. Electrochem. Soc.* **128,** 725 (1981).

155. Maranchi, J. P., Hepp, A. F. & Kumta, P. N. High Capacity, Reversible Silicon Thin-Film Anodes for Lithium-Ion Batteries. *Electrochem. Solid-State Lett.* **6,** A198 (2003).

156. Naguib, M. *et al.* MXene: A promising transition metal carbide anode for lithium-ion batteries. *Electrochem. commun.* **16,** 61–64 (2012).

157. Lipatov, A. *et al.* Effect of Synthesis on Quality, Electronic Properties and Environmental Stability of Individual Monolayer Ti 3 C 2 MXene Flakes. *Adv. Electron. Mater.* **2,** 1600255 (2016).

158. Shahzad, F. *et al.* Electromagnetic interference shielding with 2D transition metal carbides (MXenes). *Science.* **353,** 1137–1140 (2016).

159. Nicolosi, V., Chhowalla, M., Kanatzidis, M. G., Strano, M. S. & Coleman, J. N. Liquid Exfoliation of Layered Materials. *Science.* **340,** 1226419–1226419 (2013).

160. Dillon, A. D. *et al.* Highly Conductive Optical Quality Solution-Processed Films of 2D Titanium Carbide. *Adv. Funct. Mater.* **26,** 4162–4168 (2016).

161. Mashtalir, O. *et al.* Dye adsorption and decomposition on two-dimensional titanium carbide in aqueous media. *J. Mater. Chem. A* **2,** 14334–14338 (2014).

162. Backes, C. *et al.* Production of Highly Monolayer Enriched Dispersions of Liquid-Exfoliated Nanosheets by Liquid Cascade Centrifugation. *ACS Nano* **10,** 1589–1601 (2016).

163. Er, D., Li, J., Naguib, M., Gogotsi, Y. & Shenoy, V. B. Ti3C2 MXene as a High Capacity Electrode Material for Metal (Li, Na, K, Ca) Ion Batteries. *ACS Appl. Mater. Interfaces* **6,** 11173–11179 (2014).

164. Halim, J. *et al.* X-ray photoelectron spectroscopy of select multi-layered transition metal carbides (MXenes). *Appl. Surf. Sci.* **362,** 406–417 (2016).

165. Irie, H., Watanabe, Y. & Hashimoto, K. Nitrogen-Concentration Dependence on Photocatalytic Activity of TiO 2 - x N x Powders. *J. Phys. Chem. B* **107,** 5483–5486 (2003).

166. Hanlon, D. *et al.* Liquid exfoliation of solvent-stabilized few-layer black phosphorus for applications beyond electronics. *Nat. Commun.* **6,** 8563 (2015).

167. Liaw, B. Y. *et al.* Correlation of Arrhenius behaviors in power and capacity fades with cell impedance and heat generation in cylindrical lithium-ion cells. *J. Power Sources* **119,** 874–886 (2003).

168. Peng, Y.-Y. *et al.* All-MXene (2D titanium carbide) solid-state microsupercapacitors for on-chip energy storage. *Energy Environ. Sci.* **9,** 2847–2854 (2016).

169. Zhang, C. J., Liu, X. & Nicolosi, V. Synthesis and Physicochemical Properties of Two-

Dimensional Gallium Sulfide Crystals. *Bioenerg. Open Access* **5,** 1–3 (2016).

170. Liang, X., Garsuch, A. & Nazar, L. F. Sulfur Cathodes Based on Conductive MXene Nanosheets for High-Performance Lithium-Sulfur Batteries. *Angew. Chemie Int. Ed.* **54,** 3907–3911 (2015).

171. Rakhi, R. B., Ahmed, B., Hedhili, M. N., Anjum, D. H. & Alshareef, H. N. Effect of Postetch Annealing Gas Composition on the Structural and Electrochemical Properties of Ti_2CT_x MXene Electrodes for Supercapacitor Applications. *Chem. Mater.* **27,** 5314–5323 (2015).